December 2008
SLAC-R-915

ABSTRACT

Title of dissertation: MEASUREMENT OF *CP* CONTENT AND TIME-DEPENDENT *CP* VIOLATION IN $B^0 \to D^{*+}D^{*-}$ DECAYS

Jacob M. Anderson,
Doctor of Philosophy, 2008

Dissertation directed by: Professor Douglas Roberts
Department of Physics

This dissertation presents the measurement of the the *CP*-odd fraction and time-dependent *CP* violation parameters for the $B^0 \to D^{*+}D^{*-}$ decay. These results are based on the full *BABAR* dataset of $(467 \pm 5) \times 10^6$ $B\overline{B}$ pairs collected at the PEP-II B Factory at the Stanford Linear Accelerator Center. An angular analysis finds that the *CP*-odd fraction of the $B^0 \to D^{*+}D^{*-}$ decay is $R_\perp = 0.158 \pm 0.028 \pm 0.006$, where the first uncertainty is statistical, and the second is systematic. A fit to the flavor-tagged, time-dependent, angular decay rate yields

$$C_+ = \quad 0.02 \pm 0.12 \pm 0.02$$

$$C_\perp = \quad 0.41 \pm 0.50 \pm 0.08$$

$$S_+ = -0.76 \pm 0.16 \pm 0.04$$

$$S_\perp = -1.81 \pm 0.71 \pm 0.16\,,$$

for the *CP*-odd ($\perp$) and *CP*-even ($+$) contributions. Constraining these two contri-

SLAC National Accelerator Center, 2575 Sand Hill Road, Menlo Park, CA 94309

Work supported in part by US Department of Energy contract DE−AC02−76SF00515

butions to be the same results in

$$C = \quad 0.047 \pm 0.091 \pm 0.019$$

$$S = -0.71 \pm 0.16 \pm 0.03\,.$$

These measurements are consistent with the Standard Model and with measurements of sin2β from $B^0 \to (c\bar{c})K^0$ decays.

SLAC-R-915

MEASUREMENT OF *CP* CONTENT AND TIME-DEPENDENT *CP* VIOLATION IN $B^0 \to D^{*+}D^{*-}$ DECAYS

by

Jacob M. Anderson

Dissertation submitted to the Faculty of the Graduate School of the
University of Maryland, College Park in partial fulfillment
of the requirements for the degree of
Doctor of Philosophy
2008

Advisory Committee:

Associate Professor Douglas Roberts, Chair/Advisor
Professor Abolhassan Jawahery
Professor Rabindra Mohapatra
Professor Nick Hadley
Professor William McDonough, Dean's Representative

Dedication

For her unwaivering support throughout graduate school and for her gentle prodding to get this dissertation done, I dedicate this to my wife Candice. For helping me to have fun thought it all, I include my sons Seth and Grant in my dedication.

Acknowledgments

I have been fortunate to work with many excellent physicists as a student on *BABAR*. I am grateful to Doug Roberts for taking me on as a student and giving me this opportunity to learn and grow. I have been especially helped by Chunhui Chen whose insights and level-headedness have helped me in most of my research. I would like to thank Hassan Jawahery for his gentle mentoring while I was resident at SLAC. The *BABAR* graduate student community has also been a great blessing, providing insight, help and levity whenever needed.

I have had enjoyable and educational interactions during my research with the PEP operators and physicists and *BABAR* management which have served to give me a broader view. I would also like to acknowledge the late SLAC tour program, which made me think about broader science issues and gave me a forum to share my love of science with the public at large.

Table of Contents

List of Tables vii

List of Figures ix

1 Introduction 1
1.1 Matter and anti-matter . . . 1
1.2 Outline of contents . . . 2

2 Theoretical Overview 3
2.1 The Standard Model . . . 3
2.1.1 Discrete symmetries . . . 5
2.1.2 Weak flavor mixing . . . 6
2.2 *CP* violation . . . 8
2.2.1 The CKM matrix . . . 8
2.2.2 Time-dependent *CP* violation . . . 9
2.3 $B^0 \to D^{*+}D^{*-}$ theory . . . 14
2.4 Full angular analysis measurement . . . 20
2.5 Summary . . . 22

3 PEP-II *B* Factory and the *BABAR* Detector 23
3.1 PEP-II . . . 23
3.2 Silicon Vertex Tracker (SVT) . . . 27
3.2.1 SVT electronics . . . 28
3.2.2 SVT radiation monitoring (SVTRAD) . . . 29
3.2.3 SVT performance . . . 29
3.3 Drift Chamber (DCH) . . . 31
3.4 Detector of Internally Reflected Cherenkov Light (DIRC) . . . 34
3.4.1 DIRC construction . . . 35
3.4.2 DIRC electronics and reconstruction . . . 36
3.5 Electromagnetic Calorimeter (EMC) . . . 37
3.6 Instrumented Flux Return (IFR) . . . 40
3.7 The *BABAR* trigger, DAQ and computing systems . . . 44
3.7.1 Level 1 (L1) trigger . . . 44
3.7.2 Level 3 (L3) trigger . . . 47
3.7.3 Detector control and monitoring . . . 47
3.8 Central event reconstruction . . . 49

4 *B* meson reconstruction and signal yields 51
4.1 Data sample . . . 51
4.2 Event pre-selection . . . 52
4.3 Track selection . . . 53
4.4 Composite particle reconstructions . . . 53
4.4.1 π^0 reconstruction . . . 53

4.4.2 K^0_S reconstruction . . . 54
4.4.3 D meson reconstruction . . . 54
4.4.4 D^* reconstruction . . . 54
4.5 B meson reconstruction and selection . . . 55
4.6 B flavor tagging . . . 59
4.7 Signal yields . . . 63
4.7.1 Yield extraction . . . 63
4.7.2 Peaking background . . . 64

5 Transversity angle analysis for the CP-odd fraction 66
5.1 Angular Distribution . . . 66
5.2 Angular acceptance moments . . . 67
5.2.1 Monte Carlo integration . . . 68
5.2.2 Parameterization of acceptance moments . . . 70
5.2.3 Acceptance moment validation . . . 73
5.3 Angular resolution model . . . 74
5.3.1 Uncorrelated soft pions . . . 75
5.3.2 Parameterization of the angular resolution . . . 75
5.3.3 Angular resolution validation . . . 76
5.4 Angular fit description and validation . . . 80
5.4.1 Toy MC validation . . . 81
5.4.2 Full MC validation . . . 82
5.5 Angular fit systematic errors . . . 86
5.5.1 Angular resolution model . . . 86
5.5.2 Angular acceptance parameters . . . 88
5.5.3 Parameter α . . . 91
5.5.4 Peaking background . . . 91
5.5.5 Background Model . . . 92
5.5.6 Potential fit bias . . . 93
5.6 Results . . . 93

6 Time-dependent CP analysis 95
6.1 B tagging performance . . . 96
6.2 Δt resolution function . . . 96
6.3 CP fit description and validation . . . 98
6.3.1 Toy MC validation . . . 100
6.3.2 Embedded toy MC validation . . . 104
6.3.3 Full MC validation . . . 104
6.4 Systematic uncertainties . . . 111
6.4.1 Tagging parameters . . . 111
6.4.2 Peaking background . . . 113
6.4.3 Prompt background fraction . . . 113
6.4.4 Fixed Δm_d and τ_{B^0} parameters . . . 114
6.4.5 Angular resolution . . . 114
6.4.6 Angular background . . . 114

6.4.7 Potential fit bias . . . 119
6.4.8 Boost uncertainty . . . 119
6.4.9 SVT alignment . . . 119
6.4.10 Tag interference from DCSD amplitudes . . . 120
6.5 Results . . . 122

7 Conclusions 128
7.1 Summary of results . . . 128
7.2 Final words . . . 128

Bibliography 132

List of Tables

2.1 The fundamental particles and their principle quantum numbers. . . . 4

2.2 The gauge bosons of the standard model and the forces they mediate. 4

2.3 Minimal SM matter fields, their U(1) hypercharge, SU(2) representation dimension, and SU(3) representation dimension. The L and R are the handedness of the fields. The $i = 1, 2, 3$ enumerates the generations. The $\alpha = r, g, b$ denotes the SU(3) transformations of the quarks. 6

3.1 PEP-II design and current parameters. 25

3.2 Cross-sections at $\sqrt{s} = E_{\Upsilon(4S)}$ 26

3.3 Parameters of the SVT sensors by layer and side. 28

4.1 D meson decay modes and branching fractions used in this analysis. . 52

4.2 Cuts on $-\ln(\mathcal{L}_{\text{mass}})$ by D decay mode. 56

4.3 Cuts on $|\Delta E|$ in MeV by D decay mode. 58

4.4 Tagging category definitions based on the output of the B Tagger neural net, NN. 63

5.1 Parameters of the acceptance moments for each of the three slow pion modes. 71

5.2 Parameters of the resolution model extracted from signal MC. 76

5.3 Systematic uncertainties of $R_\perp$. 86

5.4 Values of floating parameters in the fit to data to extract $R_\perp$. 93

6.1 Tagging efficiency parameters found from fitting the B_{flav} data sample. Tagging efficiency ε, efficiency difference between B^0 and $\overline{B}^0$ tagged events $\Delta\varepsilon$, mis-tag fraction w, mis-tag difference between B^0 and $\overline{B}^0$ tagged events Δw, and effective tagging power Q. All quantities are given in percent. 97

6.2 Resolution and tagging parameters extracted in fits to the $B^0 \to D^{*+}D^{*-}$ signal MC, B_{flav} MC, and B_{flav} data samples. 99

6.3 Parameters which float in the time-dependent *CP* fit. 101

6.4 Fitted *CP* parameters for MC simulation including full detector simulation. 111

6.5 Systematic error contributions to $B^0 \to D^{*+}D^{*-}$ *CP* parameters. . . . 113

6.6 Correlations of *CP* parameters for the case where they are split based on *CP*-even or -odd. 123

6.7 Correlations of *CP* parameters for the case where they are not split. . 123

6.8 Fit results from the fit to data. The errors are purely statistical. . . . 124

7.1 *CP* parameters extracted from the full dataset. The first uncertainty is statistical; the second is systematic. 128

List of Figures

2.1 The Unitarity Triangle in the (ρ, η) plane. 9

2.2 Leading diagrams for the $B^0 \to D^{*+}D^{*-}$ decay. 15

2.3 The $B^0 \to D^{*+}D^{*-}$ decay in the helicity basis. 17

2.4 The $B^0 \to D^{*+}D^{*-}$ decay in the transversity basis. 18

3.1 A drawing of the *BABAR* detector in the $y - z$ plane. 24

3.2 A drawing of the *BABAR* detector in the $x - y$ plane. 24

3.3 Drawing of the SVT: longitudinal section. 27

3.4 Drawing of the SVT: transverse section. 30

3.5 Schematic diagram for the ATOM chip circuitry for a single channel. 30

3.6 Block diagram of the SVT including power and DAQ. 32

3.7 SVT hit resolution. 32

3.8 Schematic layout of the first four superlayers of the DCH. Lines have been added between the field wires to demarcate the cells. 33

3.9 Schematic of principles of the DIRC detector. 35

3.10 Drawing of the a single EMC crystal. 38

3.11 Top half of the longitudinal cross-section of the EMC showing the arrangement of the crystals. Dimensions are given in mm. 41

3.12 Cross-section of an RPC with the schematics of the high voltage connection. 41

3.13 Cross-section of an LST. 42

3.14 Muon efficiency of the barrel system. The dashed red curve is the original RPC installation; the solid back were the RPCs in 2004; the solid green is the RPCs in 2005; and the dotted blue is the LSTs in 2005. 43

3.15 A schematic representation of the L1 trigger. 45

3.16 A schematic representation of the *BABAR* online computer systems. . . 48

4.1 The $-\ln(\mathcal{L}_{\rm mass})$ distributions for signal and background. The top plot shows the distribution in pure signal MC. The bottom is background from generic MC scaled to relative luminosity. Red is B^+B^- background; green is $B^0\overline{B}^0$ background; blue is $c\bar{c}$ background; and magenta is $u\bar{u}+d\bar{d}+s\bar{s}$ background. 57

4.2 Distribution of ΔE in data. This sample is before final event selection and uses cuts $-\ln(\mathcal{L}_{\rm mass}) < 10$ and $m_{\rm ES} > 5.27\,{\rm GeV}/c^2$ to enrich the signal. The curve is a Gaussian plus a line and is only an illustration. 58

4.3 Representation of the two time measurement technique for time-dependent *CP* violation. 60

4.4 Sub-taggers of the *BABAR* flavor tagging routine. 62

4.5 Output of the B Tagger neural net, -1 indicates $\overline{B}^0$ and 1 B^0. The blue histogram is true $\overline{B}^0$. The red is true B^0. 62

4.6 Fit to the $m_{\rm ES}$ distribution in data. The blue cure is the signal plus the background, and the red is the background contribution. 64

4.7 Distributions of $m_{\rm ES}$ taken from generic MC samples weighted to integrated luminosity. 65

5.1 Generated $\cos\theta_{\rm tr}$ distributions showing the effects of detector acceptance. 69

5.2 Slow pion efficiency as a function of momentum for data (points) and MC (histogram). 70

5.3 Acceptance moment distributions for the three moments (I_0, $I_\parallel$, $I_\perp$). The first line is for $\pi^+\pi^-$, the second $\pi^+\pi^0$, and the third $\pi^0\pi^-$. . . . 72

5.4 Deviation from generated $R_\perp$ for high statistics toy MC fits. Each point represents a single 200k event fit. The black line and square points are from fits where acceptance was neglected. The circular points are from fits which include acceptance. The blue line is zero. . 73

5.5 Projections of the $\pi^+\pi^0$ resolution function in bins of $\theta'_{\rm tr}$. The magenta histogram are events where the slow pion actually came from the other B. The cyan histogram is where the slow pion came from the signal B but was not the true slow pion. The dashed line is the contribution from $P_{\rm misReco}$ 77

5.6 Projections of the $\pi^+\pi^-$ resolution function in bins of $\theta'_{\rm tr}$. The magenta histogram are events where the slow pion actually came from the other B. The cyan histogram is where the slow pion came from the signal B but was not the true slow pion. The dashed line is the contribution from $P_{\rm misReco}$ 78

5.7 Projections of the $\pi^0\pi^-$ resolution function in bins of $\theta'_{\rm tr}$. The magenta histogram are events where the slow pion actually came from the other B. The cyan histogram is where the slow pion came from the signal B but was not the true slow pion. The dashed line is the contribution from $P_{\rm misReco}$ 79

5.8 Toy MC study where each point is a 300k event experiment generated using the full detector resolution model. The square points and black line are from fits using a model that neglects detector resolution. The circular points and blue line are from a model that includes detector resolution. 80

5.9 Plots showing the distributions from 200 toy MC experiments. The left is $R_\perp$; the center is its error; and the right is the pull overlaid with a Gaussian fit. 82

5.10 Deviations from the generated value of $R_\perp$ for toy MC experiments with 100k events over the expected range of $R_\perp$. 83

5.11 Projection of the signal MC fit result unto $\cos\theta_{\rm tr}$ (top) and $m_{\rm ES}$ (bottom). 84

5.12 Projection of the generic MC fit result onto $\cos\theta_{\rm tr}$ (top) and $m_{\rm ES}$ (bottom). The dashed red line represents the contribution from the background. 85

5.13 Distribution of $\delta R_\perp$ from fits using randomized resolution parameters. 87

5.14 Distribution of $\delta R_\perp$ from fits using randomized acceptance moment parameters for the $\pi^+\pi^-$ acceptance moments 88

5.15 Distribution of $\delta R_\perp$ from fits using randomized acceptance moment parameters for the $\pi^+\pi^0$ acceptance moments. 89

5.16 Distribution of $\delta R_\perp$ from fits using randomized acceptance moment parameters for the $\pi^0\pi^-$ acceptance moments. 90

5.17 Blind values of $R_\perp$ as a function of α. The statistical error bars have been suppressed for clarity. 91

5.18 Distribution of $\cos\theta_{\rm tr}$ data for the sideband $m_{\rm ES} < 5.27\,{\rm GeV}/c^2$. The red dashed line is the background contribution from the fit. 92

5.19 The fit result projected onto $\cos\theta_{\rm tr}$ for data where $m_{\rm ES} > 5.27\,{\rm GeV}/c^2$. The solid blue line is the total PDF, and the dashed red line is the background contribution. 94

6.1 Difference between fitted and generated S and C as a function of the value of S. Here $R_\perp = 0.125$, $C = 0$, and $\alpha = 0$. 102

6.2 Difference between fitted and generated S and C as a function of the value of C. Here $R_\perp = 0.125$, $S = -0.7$, and $\alpha = 0$. 102

6.3 Difference between fitted and generated S and C as a function of the value of $R_\perp$. Here $C = 0.0$, $S = -0.7$, and $\alpha = 0$. 103

6.4 Difference between fitted and generated S and C as a function of the value of α. Here $R_\perp = 0.125$, $C = 0.0$, and $S = -0.7$. 103

6.5 Toy MC distributions of the *CP* parameters S_+, $S_\perp$, C_+, and $C_\perp$ for 500 toy experiments. The left plot is the distribution of the parameter; the center is the distribution of the errors; and the right is the pull. 105

6.6 Embedded toy MC distributions of the *CP* parameters S_+, $S_\perp$, C_+, and $C_\perp$ for 112 experiments. The left plot is the distribution of the parameter; the center is the distribution of the errors; and the right is the pull. 106

6.7 Projection of the fit to signal MC onto $m_{\rm ES}$ for each of the tagging categories and combined in the final plot. 107

6.8 Projection of the fit to signal MC onto Δt and the raw flavor asymmetry for each of the tagging categories. 108

6.9 Projection of the fit to generic MC onto $m_{\rm ES}$ for each of the tagging categories and combined in the final plot. 109

6.10 Projection of the fit to generic MC onto Δt and the raw flavor asymmetry for each of the tagging categories. 110

6.11 Distribution of CP parameters fit using randomized sets of tagging and Δt resolution parameters. 112

6.12 Distribution of *CP* parameters split by *CP*-even and odd using randomized angular resolution parameters for the $\pi^+\pi^0$ slow pion mode. 115

6.13 Distribution of *CP* parameters split by *CP*-even and odd using randomized angular resolution parameters for the $\pi^+\pi^-$ slow pion mode. 116

6.14 Distribution of *CP* parameters split by *CP*-even and odd using randomized angular resolution parameters for the $\pi^0\pi^-$ slow pion mode. 117

6.15 Distribution of combined *CP* parameters using randomized angular resolution parameters for the $\pi^+\pi^0$ slow pion mode. 117

6.16 Distribution of combined *CP* parameters using randomized angular resolution parameters for the $\pi^+\pi^-$ slow pion mode. 118

6.17 Distribution of combined *CP* parameters using randomized angular resolution parameters for the $\pi^0\pi^-$ slow pion mode. 118

6.18 Distributions of the deviation of C and S due to doubly-CKM-suppressed decays. 121

6.19 Projections of the fit result onto data. The left plot is the $m_{\rm ES}$ spectrum for all tagging categories. The right plot is the projection onto Δt and its raw flavor asymmetry for the `Lepton`, `Kaon I`, and `Kaon II` events. 125

6.20 Projections of the $m_{\rm ES}$ component of the fit result onto data for each tagging category. The dashed red line represents the background contribution. 126

6.21 Projections of the Δt component of the fit result onto data for each tagging category. The triangular points and blue dashed line are for B^0 tagged events. The circular points and red line are for the $\overline{B}^0$ tagged events. The lower of each plot is the raw flavor asymmetry. . . 127

7.1 Averages showing sin2β from measurements of $b \to c\bar{c}d$ transitions in comparison with that from the "golden" $b \to c\bar{c}s$ transitions. 129

7.2 Constraints on the Unitarity Triangle in the $(\bar{\rho}, \bar{\eta})$ plane. 131

Chapter 1

Introduction

1.1 Matter and anti-matter

Since the earliest history, man has wondered how the universe came into being and how the different parts work together. Recently, fundamental physics has had tremendous success using small, local phenomena to explain both small and large-scale dynamics.

Observationally, our universe has an abundance of matter with respect to anti-matter. Early on, it was believed that matter and anti-matter behaved very symmetrically. This was at odds with the observed universe and a "Big Bang" derived cosmology. In 1967, Sakharov listed three general conditions [1] that were necessary to produce the conditions currently observed in the universe:

- C and CP violation
- baryon number violation
- departure from thermal equilibrium.

CP asymmetry could produce the matter/anti-matter asymmetry observed in the universe, so quantifying CP violation is a central measurement in particle physics. In the Standard Model, based on local gauge symmetries, CP violation arises naturally from spontaneous symmetry breaking at the electro-weak scale. The B factories

were designed to probe *CP* asymmetry and represent the height of sensitivity to this phenomena.

1.2 Outline of contents

This dissertation details the measurement of the *CP* content and *CP* asymmetry of the $B^0 \to D^{*+}D^{*-}$ decay. Chapter 2 contains a description of the pertinent theory from the Standard Model and an overview of *CP* violation with a particular emphasis on the $B^0 \to D^{*+}D^{*-}$ system. Chapter 3 describes the *BABAR* detector systems. Chapter 4 details the selection and composition of the data set as well as signal yields and background composition. Chapter 5 looks at a 1D angular analysis to determine the *CP*-odd fraction of the $B^0 \to D^{*+}D^{*-}$ decay. Chapter 6 presents an analysis resulting in the measurement of the *CP* asymmetries, and Chapter 7 reviews the results and discusses how they can be incorporated into understanding the Standard Model.

Chapter 2

Theoretical Overview

The $B^0 \rightarrow D^{*+}D^{*-}$ decay provides a means to measure the *CP* violation parameter sin2β as a cross-check to the $B^0 \rightarrow J/\psi K^0_s$ and related modes [2]. To better understand the importance of this decay mode, I present an overview of the Standard Model of particle physics as it relates to *CP* violation and B meson physics. Much of the phenomenology dealing with *CP* violation in this chapter is taken from the *BABAR Physics Book* [3]

2.1 The Standard Model

The Standard Model (SM) of particle physics describes the fundamental particles and their interactions as a result of three local gauge symmetries, $\mathrm{SU}(3)_C \times \mathrm{SU}(2)_L \times \mathrm{U}(1)_Y$. The $\mathrm{SU}(3)_C$ group is for the strong interaction, quantum chromodynamics (QCD). The $\mathrm{SU}(2)_L$ group is for the "weak isospin" that couples to the left-handed fermions. This group combined with the $\mathrm{U}(1)_Y$ group for "weak hypercharge" are the fundamental symmetries of the electro-weak interactions. The known six leptons and six quarks, enumerated in Table 2.1, their corresponding anti-particles, and their interactions fit into representations of these of these groups.

Through imposing local gauge invariance, we obtain an appropriate description of the interactions between the fermions. Local gauge invariance requires the

	Family			Electric		Weak Charge		
Fermion	1	2	3	charge	Color	left-hd.	right-hd.	Spin
Leptons	ν_e	ν_μ	ν_τ	0	0	$\frac{1}{2}$	n/a	$\frac{1}{2}$
	e	μ	τ	-1	0	$-\frac{1}{2}$	0	$\frac{1}{2}$
Quarks	u	c	t	$\frac{2}{3}$	r,g,b	$\frac{1}{2}$	0	$\frac{1}{2}$
	d	s	b	$-\frac{1}{3}$	r,g,b	$-\frac{1}{2}$	0	$\frac{1}{2}$

Table 2.1: The fundamental particles and their principle quantum numbers.

Force	Coupling Charge	Particles Exchanged	Symmetry
Electro-weak	Electric/weak	Photon (γ),$W^\pm$,Z^0	SU(2) $\times$ U(1)
Strong	Color	8 gluons (g)	SU(3)

Table 2.2: The gauge bosons of the standard model and the forces they mediate.

introduction of gauge fields which give rise to the gauge bosons, listed in Table 2.2, which mediate the interactions between particles.

The gauge fields are always massless; however from experiment, it is known that the W^+, W^-, and Z^0 bosons are not massless. These fields are allowed to "acquire" mass through spontaneous symmetry breaking via the Higgs mechanism. This mechanism, introduced by Weinberg and Salam in 1967 [4, 5], is critical to the model of the electro-weak interactions. The details of gauge theories and spontaneous symmetry breaking are beyond the scope of this thesis and are contained in physics texts on field theory and particle physics [6, 7]. To appreciate the context of *CP* violation in B meson decays, I present the important aspects from the SM in weak mixing and properties of discrete symmetries.

2.1.1 Discrete symmetries

Discrete symmetries appear in both classical and quantum theories of physics. Left-right, or parity, symmetry (P), expressed as $\mathbf{x} \rightarrow -\mathbf{x}$ and time-reversal symmetry (T), $t \rightarrow -t$, are well-known in classical physics. Within quantum field theory, a third discrete symmetry applies, one of charge conjugation (C) that changes a particle to its anti-particle.

Early in the 20th century, scientists assumed that each of these three transformations was a fundamental symmetry of nature. However, experiment soon showed that weak interactions do not preserve these symmetries as the strong and electromagnetic interactions do. P was violated in nuclear decays [8], while neutrinos seemed to all have a left-handed helicity indicating C violation. At the same time, the product, CP, seemed to be preserved in these interactions.

In 1964, Christensen *et al.* [9] observed CP violation in the neutral K decays $K_L^0 \rightarrow \pi\pi$. More recently in 2001, both the *BABAR* and BELLE experiments observed CP violation in B meson decays [10, 11]. CP violation arises in the SM through the Cabibbo, Kobayashi and Maskawa quark mixing matrix. The origin of this mixing matrix arises from the breaking of the $\mathrm{SU}(2)_L \times \mathrm{U}(1)_Y$ weak symmetry group. The origin of this matrix will be explored in Sec. 2.1.2.

To complete the discussion of discrete symmetries, we must note that the combined CPT transformation appears to be a preserved. While C, P, or T are violated in nature, the "CPT theorem" states that any quantum field theory which is both Lorentz invariant and obeys spin statistics must also be CPT invariant. As

Field	U(1)	SU(2)	SU(3)
$u_R^{i,\alpha}$	$\frac{2}{3}$	**1**	**3**
$d_R^{i,\alpha}$	$-\frac{1}{3}$	**1**	**3**
e_R^i	-1	**1**	**1**
$Q_L^i = \begin{pmatrix} u_L^{i,\alpha} \\ d_L^{i,\alpha} \end{pmatrix}$	$\frac{1}{6}$	**2**	**3**
$L_L^i = \begin{pmatrix} \nu_L^i \\ e_L^{-,i} \end{pmatrix}$	$-\frac{1}{2}$	**2**	**1**
$\phi = \begin{pmatrix} \phi^+ \\ \phi^0 \end{pmatrix}$	$\frac{1}{2}$	**2**	**1**

Table 2.3: Minimal SM matter fields, their U(1) hypercharge, SU(2) representation dimension, and SU(3) representation dimension. The L and R are the handedness of the fields. The $i = 1, 2, 3$ enumerates the generations. The $\alpha = r, g, b$ denotes the SU(3) transformations of the quarks.

a consequence of this theorem the mass and decay width of a particle and its anti-particle are exactly equal. To date no experiments have found deviation from *CPT* invariance [12, 13].

2.1.2 Weak flavor mixing

Within the SM, the Higgs mechanism plays a central role by "bestowing" mass on all of the fundamental fields and breaking the electro-weak gauge symmetry. By introducing a scalar field that acquires a vacuum expectation value v, one produces the appropriate mass terms in the SM Lagrangian [7]. The simplest model involves a doublet scalar field which belongs to the electro-weak gauge group SU(2) $\times$ U(1):

$$\phi = \begin{pmatrix} \phi^+ \\ \\ \phi^0 \end{pmatrix} , \tag{2.1}$$

where ϕ^+ and ϕ^0 are complex fields. If we consider couplings between the Higgs field and the quarks and leptons then these fields acquire the typical mass terms in

the Lagrangian. Consider the Yukawa couplings

$$\mathcal{L}_Y = -\left(g_d^{ij}\overline{Q}_L^i \phi d_R^j + g_u^{ij}\overline{Q}_L^i \tilde{\phi} u_R^j + g_e^{ij}\overline{L}_L^i \phi e_R^i\right) + \text{h.c.}\,, \tag{2.2}$$

where i and j label the generation of the fermions and $\tilde{\phi}$ denotes the SU(2) doublet $\tilde{\phi} = i\tau_2\phi^{\dagger T}$. The g_u, g_d, g_e couplings are in general 3×3 complex matrices. By substituting the v for the Higgs field, we obtain the mass terms.

$$\mathcal{L}_Y = -\overline{d}_L \mathcal{M}_d d_R - \overline{u}_L \mathcal{M}_u u_R - \overline{e}_L \mathcal{M}_e e_R\,, \tag{2.3}$$

where $\mathcal{M}_k^{ij} = v g_k^{ij}$, $k = u, d, e$, are the mass matrices. These matrices are not necessarily diagonal, introducing mixing between the different generations.

Using a unitary transformation,

$$\begin{aligned} u_L &= U_L^u u'_L \quad , \quad u_R = U_R^u u'_R\,, \\ d_L &= U_L^d d'_L \quad , \quad d_R = U_R^d d'_R\,, \end{aligned} \tag{2.4}$$

we can define a diagonal mass matrix $\mathcal{M}' = U_L^{\dagger k}\mathcal{M}_k U_R^k$. This definition of the fields does not affect the kinematic terms in the Lagrangian nor the Z and photon couplings. Because neutrinos are massless within the SM, the lepton fields may be chosen to be simultaneous mass and weak eigenstates, leaving the lepton terms unchanged. The quark couplings to the W can be written as

$$g\overline{u}_L \gamma^\mu d_L W_\mu^+ + \text{h.c.} \rightarrow g\overline{u}'^i_L \gamma^\mu V_{\text{CKM}}^{ij} d_L^j W_\mu^+ + \text{h.c.} \tag{2.5}$$

From this relation, we see that $V_{\text{CKM}} \equiv U_L^{\dagger u} U_L^d$ is a natural result of the Higgs mechanism and that the matrix describes quark mixing in the SM weak sector. V_{CKM} was first introduced by Cabibbo, Kobayashi and Maskawa (CKM) [14, 15].

As will be seen in the next section, the CKM matrix gives rise to *CP* violation in the SM.

2.2 *CP* violation

2.2.1 The CKM matrix

Within the SM, *CP* violation occurs through the CKM quark mixing matrix,

$$V_{\text{CKM}} = \begin{pmatrix} V_{ud} & V_{us} & V_{ub} \\ V_{cd} & V_{cs} & V_{cb} \\ V_{td} & V_{ts} & V_{tb} \end{pmatrix} , \tag{2.6}$$

when more than one of the elements is complex. To explicitly illustrate its complex nature, it is convenient to use the Wolfenstein parameterization [16],

$$V_{\text{CKM}} = \begin{pmatrix} 1 - \frac{\lambda^2}{2} & \lambda & A\lambda^3(\rho - i\eta) \\ -\lambda & 1 - \frac{\lambda^2}{2} & A\lambda^2 \\ A\lambda^3(1 - \rho - i\eta) & -A\lambda^2 & 1 \end{pmatrix} + \mathcal{O}(\lambda^4) , \tag{2.7}$$

where λ is the sine of the Cabibbo angle, $\sin\theta_C \approx 0.22$, and A, ρ and η are real parameters. The unitarity of the CKM matrix produces six equations describing triangles in the complex plane. The Unitarity Triangle is one of these triangles governed by the equation

$$V_{ub}^* V_{ud} + V_{cb}^* V_{cd} + V_{tb}^* V_{td} = 0 . \tag{2.8}$$

Eq. 2.8 is normalized by $V_{cb}^* V_{cd}$ and yields the familiar Unitarity Triangle depicted in Fig. 2.1. The three interior angles of the unitarity triangle shown in Fig. 2.1 are

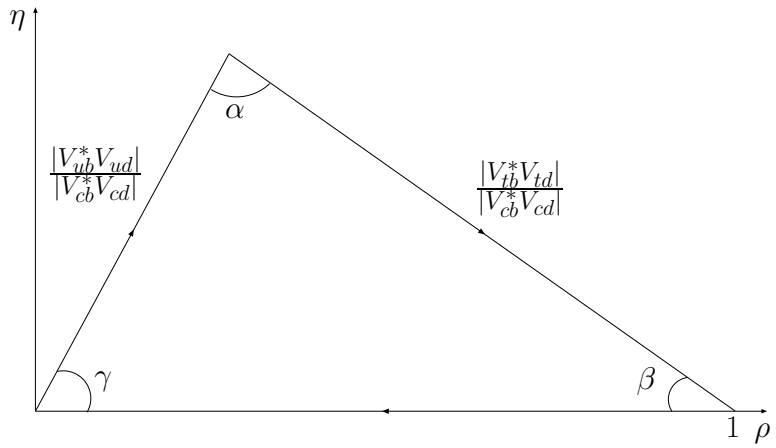

Figure 2.1: The Unitarity Triangle in the (ρ, η) plane.

defined

$$\alpha = \arg\left[-\frac{V_{td}V_{tb}^*}{V_{ud}V_{ub}^*}\right], \qquad \beta = \arg\left[-\frac{V_{cd}V_{cb}^*}{V_{td}V_{tb}^*}\right], \qquad \gamma = \arg\left[-\frac{V_{ud}V_{ub}^*}{V_{cd}V_{cb}^*}\right] . \tag{2.9}$$

By measuring the parameters of the CKM matrix, experiments constrain the Unitarity Triangle to determine the extent of CP violation in the Standard Model and hopefully reveal physics unaccounted for by the Standard Model. The $B^0 \to D^{*+}D^{*-}$ decay is most sensitive to the angle β as will be discussed in more detail in Section 2.3.

2.2.2 Time-dependent *CP* violation

In a time-dependent B analysis, the time evolution of the state $|\psi(t)\rangle = \alpha(t)|B^0\rangle + \beta(t)|\overline{B}^0\rangle$ is given by the Schroedinger equation:

$$i\frac{\partial}{\partial t}\begin{pmatrix}\alpha\\ \beta\end{pmatrix} = \mathcal{H}\begin{pmatrix}\alpha\\ \beta\end{pmatrix} \equiv \begin{pmatrix} m_{11} - \frac{i}{2}\Gamma_{11} & m_{12} - \frac{i}{2}\Gamma_{12} \\ m_{21} - \frac{i}{2}\Gamma_{21} & m_{22} - \frac{i}{2}\Gamma_{22}\end{pmatrix}\begin{pmatrix}\alpha\\ \beta\end{pmatrix} . \tag{2.10}$$

The $\arg(m_{12})$ is the phase of mixing between the flavor eigenstates, and Γ_{12} is the complex coupling to common decay modes of B^0 and $\overline{B}^0$. *CPT* invariance guarantees that $m_{11} = m_{22}$, $\Gamma_{11} = \Gamma_{22}$, $m_{21} = m_{12}^*$ and that $\Gamma_{21} = \Gamma_{12}^*$. The eigenvectors of the Hamiltonian are the mass eigenstates,

$$\begin{aligned} |B_L\rangle &= p|B^0\rangle + q|\overline{B}^0\rangle \\ |B_H\rangle &= p|B^0\rangle - q|\overline{B}^0\rangle \ , \end{aligned} \tag{2.11}$$

where $|B_L\rangle$ and $|B_H\rangle$ are the lighter and heavier states, respectively, and where p and q satisfy the relationships

$$\frac{q}{p} = \sqrt{\frac{m_{12}^* - \frac{i}{2}\Gamma_{12}^*}{m_{12} - \frac{i}{2}\Gamma_{12}}} = \frac{\Delta m - \frac{i}{2}\Delta\Gamma}{2(m_{12} - \frac{i}{2}\Gamma_{12})} \tag{2.12}$$

$$|p|^2 + |q|^2 = 1 \ . \tag{2.13}$$

The mass difference, $\Delta m = m_H - m_L$, and the decay width difference, $\Delta\Gamma = \Gamma_H - \Gamma_L$ are obtained by diagonalizing the Hamiltonian matrix in Eq. 2.10. Eq. 2.10 is easily solved for the time-dependent, mass eigenstates:

$$\begin{aligned} |B_L(t)\rangle &= e^{-im_L t - \Gamma_L t/2}|B_L\rangle \\ |B_H(t)\rangle &= e^{-im_H t - \Gamma_H t/2}|B_H\rangle \ . \end{aligned} \tag{2.14}$$

Using Eq. 2.11, the time-dependent, flavor eigenstates are

$$\begin{aligned} |B^0(t)\rangle &= e^{-iMt - \Gamma t/2}\left(\cos(\Delta m t/2)|B^0\rangle + i\frac{q}{p}\sin(\Delta m t/2)|\overline{B}^0\rangle\right) \\ |\overline{B}^0(t)\rangle &= e^{-iMt - \Gamma t/2}\left(\cos(\Delta m t/2)|\overline{B}^0\rangle + i\frac{p}{q}\sin(\Delta m t/2)|B^0\rangle\right) \ , \end{aligned} \tag{2.15}$$

assuming $\Delta\Gamma \ll \Delta m$ for simplicity.

CP violation can be measured when B^0 and $\overline{B}^0$ mesons decay into the same final state f. The decay amplitudes for such a decay are

$$A = \langle f|\mathcal{H}|B^0\rangle$$
$$\overline{A} = \langle f|\mathcal{H}|\overline{B}^0\rangle \ . \tag{2.16}$$

The decay rates are given by the magnitude square of the amplitudes, which, using Eq. 2.15, can be expressed as:

$$|\langle f|\mathcal{H}|B^0(t)\rangle|^2 = e^{-\Gamma t}|A|^2\left[\frac{1}{2}(1+|\lambda|^2) + \frac{1}{2}(1-|\lambda|^2)\cos(\Delta m t) - \mathrm{Im}\lambda\,\sin(\Delta m t)\right]$$
$$|\langle f|\mathcal{H}|\overline{B}^0(t)\rangle|^2 = e^{-\Gamma t}|A|^2\left[\frac{1}{2}(1+|\lambda|^2) - \frac{1}{2}(1-|\lambda|^2)\cos(\Delta m t) + \mathrm{Im}\lambda\,\sin(\Delta m t)\right] \ , \tag{2.17}$$

where

$$\lambda = \frac{q}{p}\frac{\overline{A}_f}{A_f} \ . \tag{2.18}$$

The asymmetry is constructed by dividing the difference of the two decay rates by their sum,

$$a_{f_{CP}} = \frac{1-|\lambda|^2}{1+|\lambda|^2}\cos(\Delta m t) - \frac{2\,\mathrm{Im}\lambda}{1+|\lambda|^2}\sin(\Delta m t) \ . \tag{2.19}$$

The parameter λ is the measure of CP violation and will be further explored.

CP violation manifests itself in three ways:

- CP violation in decay (direct CP violation), which occurs in both charged and neutral decays, when the amplitude for a decay and its CP conjugate process have different magnitudes;

- CP violation in mixing, which occurs when two neutral mass eigenstates cannot be chosen to be CP eigenstates;

- *CP* violation in the interference between decays with and without mixing which occurs in decays into final states that are common to B^0 and $\overline{B}^0$.

The differences in these manifestations are all contained within the parameter λ.

Direct *CP* violation is manifest in the ratio of the amplitude A_f to its *CP* conjugate amplitude $\overline{A}_{\overline{f}}$. Two types of phases occur in these amplitudes. The first type of phases occur in the complex parameters in the Lagrangian. In the Standard Model these phases occur only in the CKM matrix and are often called "weak" phases. The second type of phase can appear in the scattering or decay amplitudes even when the Lagrangian is real. Such phases do not violate *CP* because they appear in A_f and $\overline{A}_{\overline{f}}$ with the same sign. Their origin is possible contribution from intermediate on-shell states in the decay process, that is an absorptive part of an amplitude that has contributions from coupled channels. Usually the dominant re-scattering is due to strong interactions so they are called "strong" phases. To illustrate, it is useful to write the amplitudes with their explicit weak and strong phases, $e^{i\phi_i}$ and $e^{i\delta_i}$, respectively, as:

$$A_f = \sum_i A_i e^{i(\delta_i+\phi_i)}, \qquad \overline{A}_{\overline{f}} = \eta_f \sum_i A_i e^{i(\delta_i-\phi_i)} \ , \tag{2.20}$$

where η_f is the *CP* eigenvalue of the final state. The convention-independent ratio is then

$$\left|\frac{\overline{A}_{\overline{f}}}{A_f}\right| = \left|\frac{\sum_i A_i e^{i(\delta_i-\phi_i)}}{\sum_i A_i e^{i(\delta_i+\phi_i)}}\right| \ . \tag{2.21}$$

If *CP* is conserved, then the weak phases are all equal, but if $|\overline{A}_{\overline{f}}/A_f| \neq 1$, then *CP* is violated in the decay. It should be noted that *CP* violation will not occur unless at

least two terms with different weak phases also have different strong phases, because

$$|A|^2 - |\overline{A}|^2 = -2\sum_{i,j} A_i A_j \sin(\phi_i - \phi_j)\sin(\delta_i - \delta_j) \ . \tag{2.22}$$

Because charged particles do not mix, *CP* violation in decay is the only *CP* violation for charged mesons. In neutral mesons, direct *CP* violation competes with the other types of *CP* violation.

Eq. 2.12 can be expressed as

$$\left|\frac{q}{p}\right|^2 = \left|\frac{m_{12}^* - \frac{i}{2}\Gamma_{12}^*}{m_{12} - \frac{i}{2}\Gamma_{12}}\right| \ . \tag{2.23}$$

If *CP* is conserved, then the mass eigenstates are also *CP* eigenstates; there is no phase difference between m_{12} and Γ_{12}; and $|q/p| = 1$. For the neutral B system, *CP* violation in mixing can be measured through semileptonic decays [13].

The final type of *CP* violation, violation from interference between decay with and without mixing, can occur in neutral B meson decay without the presence of either of the other types of *CP* violation. Recall from Eq. 2.18 the definition of λ. If $|\lambda| \neq 1$, then *CP* violation is manifest through either decay or mixing, but if $\mathrm{Im}\lambda \neq 0$, then *CP* violation is manifest through the interference between decays with and without mixing. If λ is explicitly expressed in terms of the decay and mixing weak phases, ϕ_D and ϕ_M, then

$$\lambda = \frac{q}{p}\frac{\overline{A}_f}{A_f} = \eta_f e^{2i(\phi_M - \phi_D)} \ , \tag{2.24}$$

which has a non-vanishing imaginary part although its magnitude is clearly unity. In the next section we will see how the parameter λ for the $B^0 \to D^{*+}D^{*-}$ decay relates to the parameters of the CKM matrix.

2.3 $B^0 \to D^{*+}D^{*-}$ theory

The leading, contributing diagrams to the $B \to D^{(*)+}D^{(*)-}$ are shown in Fig. 2.2. To see how the CKM parameters enter into the *CP* parameter λ, consider only the tree diagram, Fig. 2.2a. For the decay $B^0 \to D^+D^-$ [17],

$$\lambda_{tree} = \left(\frac{V_{tb}^* V_{td}}{V_{tb} V_{td}^*}\right)\left(\frac{V_{cd}^* V_{cb}}{V_{cd} V_{cb}^*}\right)$$
$$\Rightarrow \ \mathrm{Im}(\lambda_{tree}) = -\sin 2\beta \ , \tag{2.25}$$

meaning that a measurement in this channel could be compared to the $B^0 \to J/\psi\, K_S^0$ measurement. However this assumes that the contribution to the decay from the penguin diagrams in Fig. 2.2b and Fig. 2.2c is negligible. This assumption however is based on calculating hadronic decays in an effective field theory assuming factorization. The validity of these calculations is, as with all hadronic calculations, model-dependent. The exchange diagram in Fig. 2.2d, which is expected to be suppressed by a factor of order $f_B/m_B \sim \mathcal{O}(\lambda^2)$, does not have a different weak phase and so would not contaminate the measurement in the same way as the penguin diagrams.

Taking into account the penguin diagrams in Fig. 2.2 the amplitudes which go into Eq. 2.18 become

$$A_f = V_{cd} V_{cb}^* T + V_{td} V_{tb}^* P$$
$$\overline{A}_f = V_{cd}^* V_{cb} T + V_{td}^* V_{tb} P \ , \tag{2.26}$$

where T is the tree-dominated term and P is the penguin-only contribution. Both terms have comparable magnitude CKM contributions so one cannot quickly dis-

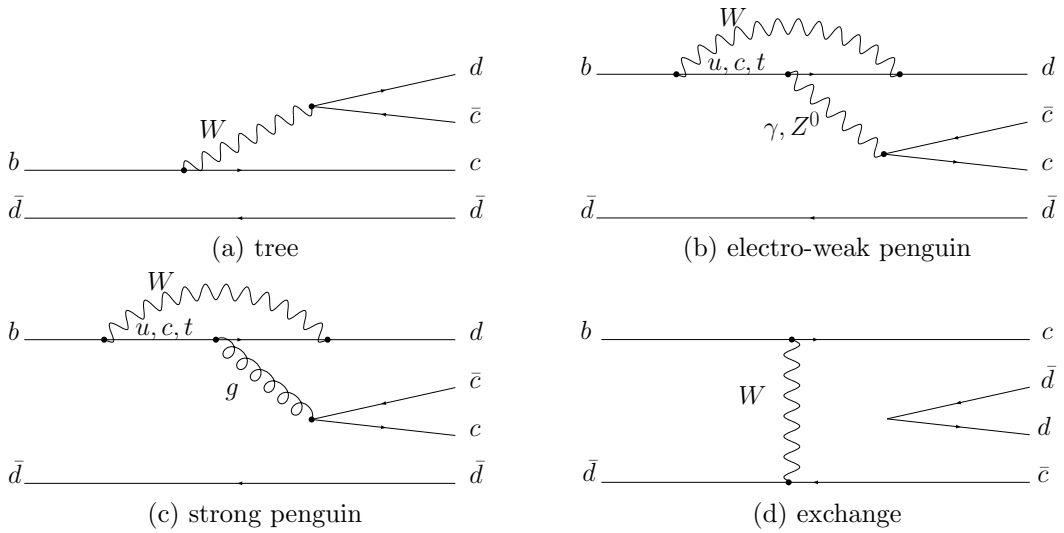

Figure 2.2: Leading diagrams for the $B^0 \to D^{*+}D^{*-}$ decay.

count the P term. Taking into account the relative strong phase, δ, between the P and T contributions, the CP violation parameter λ becomes

$$\lambda_f = \eta_f \frac{e^{-i\beta} - |R|e^{i\delta}}{e^{i\beta} - |R|e^{i\delta}} \ . \tag{2.27}$$

R is defined

$$R = zr \qquad z = \frac{V_{td}^* V_{tb}}{V_{cd}^* V_{cb}} \qquad r = \frac{P}{T} = |r|e^{i\delta} \ ; \tag{2.28}$$

z is the ratio of CKM matrix elements; and r is the ratio of the penguin-only term to the tree-dominated term. An important note is that R depends on the CKM ratio z, which in turn depends upon the weak angles α and β, meaning that the small $|R|$ limit is not *a priori* justified. Putting λ back into Eq. 2.19 leads to cosine and sine coefficients of

$$C_f = \frac{-2|R|\sin\beta\sin\delta}{1+|R|^2-2|R|\cos\beta\cos\delta} \tag{2.29}$$

and

$$S_f = \eta_f \frac{\sin 2\beta - 2|R|\sin\beta\cos\delta}{1+|R|^2-2|R|\cos\beta\cos\delta} \, , \tag{2.30}$$

respectively. These coefficients simplify in the small $|R|$ limit to

$$C_f \approx -2|R|\sin\beta\sin\delta \qquad S_f \approx \eta_f(\sin 2\beta + 2|R|\sin\beta\cos 2\beta\cos\delta) \ , \tag{2.31}$$

which simplifies to the Eq. 2.25 when $|R| = 0$. Using the factorization hypothesis, $|R| \approx 0.03$ [18], so a small $|R|$ limit may be justified. Elsewhere, the effect of the penguin contamination on the measurement of $\sin 2\beta$ was estimated to be 2% [19, 20, 21], also assuming factorization. Precision measurements in this decay channel, when compared with $B^0 \to J/\psi\, K^0_S$, would help to quantify the effects of penguin diagrams and could provide insights into the validity of the factorization hypothesis.

In addition to the possible penguin contamination, the $B^0 \to D^{*+}D^{*-}$ decay has the added complication that it is not a pure *CP* eigenstate. Because the D^* is a vector meson, and the B is a pseudo-scalar, there are three partial waves in the final state, $L = 0, 1, \text{or } 2$. The $L = 0$, "S-wave", and $L = 2$, "D-wave", states are *CP* even while the $L = 1$, "P-wave" state is *CP* odd. The contribution from different partial wave amplitudes dilutes the asymmetry, changing the decay rates in Eq. 2.17 to

$$\begin{aligned} \Gamma(B^0(t) \to D^{*+}D^{*-}) &= \Gamma_+(1+a) + \Gamma_-(1-a) \\ \Gamma(\overline{B}^0(t) \to D^{*+}D^{*-}) &= \Gamma_+(1+a) + \Gamma_-(1-a) \ , \end{aligned} \tag{2.32}$$

where Γ_+ and Γ_- are the *CP*-even and *CP*-odd decay widths respectively and a is given by Eq. 2.19. Constructing the asymmetry,

$$a_{B^0\to D^{*+}D^{*-}} = \frac{\Gamma(B^0(t) \to D^{*+}D^{*-}) - \Gamma(\overline{B}^0(t) \to D^{*+}D^{*-})}{\Gamma(B^0(t) \to D^{*+}D^{*-}) + \Gamma(\overline{B}^0(t) \to D^{*+}D^{*-})} = Da \ , \tag{2.33}$$

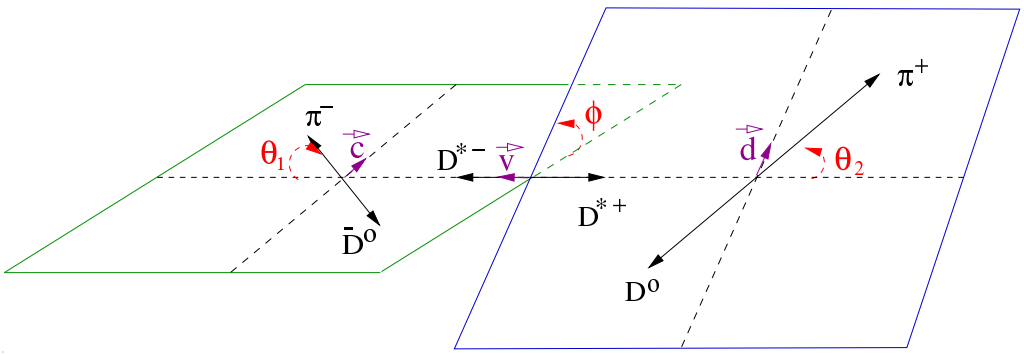

Figure 2.3: The $B^0 \to D^{*+}D^{*-}$ decay in the helicity basis.

where

$$D = \frac{\Gamma_+ - \Gamma_-}{\Gamma_+ + \Gamma_-} = \frac{\Gamma_S + \Gamma_D - \Gamma_P}{\Gamma_S + \Gamma_D + \Gamma_P} = 1 - \frac{2\Gamma_P}{\Gamma_{total}} \tag{2.34}$$

is the dilution factor. Determining the P-wave contribution to the decay rate is sufficient to determine the dilution caused by the mixture of CP final states, however a full angular analysis to extract all three partial amplitudes and relative phases would generally provide better understanding of contributions from penguin diagrams and provide a better handle on errors [2].

The differential decay amplitude is most naturally derived in the helicity basis, with two transverse polarizations (± 1) and one longitudinal polarization (0) [22], with angles defined in Fig. 2.3. In this basis, the differential decay rate is

$$\begin{aligned}
\frac{1}{\Gamma}\frac{d^4\Gamma}{d\cos\theta_1 d\cos\theta_2 d\phi dt} = \frac{9}{16\pi}\frac{1}{|A_0|^2 + |A_{+1}|^2 + |A_{-1}|^2} \times \\
\Big\{ \frac{1}{2}\sin^2\theta_1 \sin^2\theta_2 \left(|A_{+1}|^2 + |A_{-1}|^2\right) + 2\cos^2\theta_1 \cos^2\theta_2 |A_0|^2 \\
+ \sin^2\theta_1 \sin^2\theta_2 \left[\cos 2\phi\, \mathrm{Re}(A_{+1}A_{-1}^*) - \sin 2\phi\, \mathrm{Im}(A_{+1}A_{-1}^*)\right] \\
- \frac{1}{2}\sin 2\theta_1 \sin 2\theta_2 \left[\cos\phi\, \mathrm{Re}(A_{+1}A_0^* + A_{-1}A_0^*)\right. \\
\left. - \sin\phi\, \mathrm{Im}(A_{+1}A_0^* - A_{-1}A_0^*)\right] \Big\} .
\end{aligned} \tag{2.35}$$

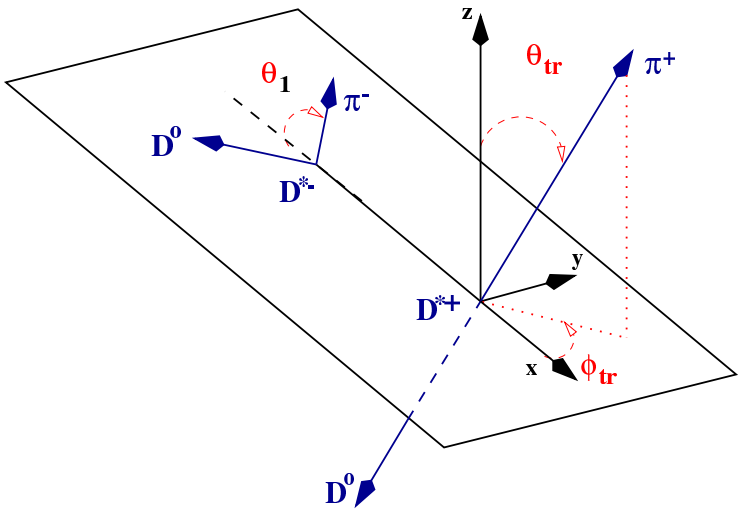

Figure 2.4: The $B^0 \to D^{*+}D^{*-}$ decay in the transversity basis.

While the helicity amplitudes, A_{+1}, A_{-1}, and A_0, can be related to the S-, P-, and D-wave eigenstates, the transversity basis provides a more convenient formalism for determining the CP-odd component of the decay rate.

The transversity basis is defined by the angles shown in Fig. 2.4. The angle θ_1 is the same in both bases. The transformation of the angular coordinates is

$$\begin{aligned} \cos\theta_2 &= \sin\theta_{tr}\cos\phi_{tr} \\ \sin\theta_2\cos\phi &= \sin\theta_{tr}\sin\phi_{tr} \\ \sin\theta_2\sin\phi &= \cos\theta_{tr} \ , \end{aligned} \tag{2.36}$$

and the decay rate becomes

$$\frac{1}{\Gamma}\frac{\mathrm{d}^4\Gamma}{\mathrm{d}\cos\theta_1\mathrm{d}\cos\theta_{tr}\mathrm{d}\phi_{tr}\mathrm{d}t} = \frac{9}{16\pi}\frac{1}{|A_0|^2+|A_\parallel|^2+|A_\perp|^2}\times$$
$$\Big\{2\cos^2\theta_1\sin^2\theta_{tr}\cos^2\phi_{tr}|A_0|^2 + \sin^2\theta_1\sin^2\theta_{tr}\sin^2\phi_{tr}|A_\parallel|^2$$
$$+\sin^2\theta_1\cos^2\theta_{tr}|A_\perp|^2 - \sin^2\theta_1\sin 2\theta_{tr}\sin\phi_{tr}\,\mathrm{Im}(A_\parallel^* A_\perp)$$
$$+\frac{1}{\sqrt{2}}\sin 2\theta_1\sin^2\theta_{tr}\sin 2\phi_{tr}\,\mathrm{Re}(A_0^* A_\parallel)$$
$$-\frac{1}{\sqrt{2}}\sin 2\theta_1\sin 2\theta_{tr}\cos\phi_{tr}\,\mathrm{Im}(A_0^* A_\perp)\Big\}\ , \tag{2.37}$$

for B^0 with amplitudes of

$$A_\parallel = \frac{1}{\sqrt{2}}(A_{+1}+A_{-1})$$
$$A_\perp = \frac{1}{\sqrt{2}}(A_{+1}-A_{-1})\ . \tag{2.38}$$

For the $\overline{B}^0$ decay, the sign of $A_\perp$ flips. The transversity amplitudes can be related to the S-, P-, and D-wave contributions to the decay rate by

$$A_S = \frac{1}{\sqrt{3}}(\sqrt{2}A_\parallel - A_0), \qquad A_P = A_\perp, \qquad A_D = \frac{1}{\sqrt{3}}(A_\parallel + \sqrt{2}A_0)\ , \tag{2.39}$$

meaning that measuring $|A_\perp|^2$ would provide the CP-odd fraction and allow an undiluted measurement of sin2β. Integrating Eq. 2.37 over ϕ_{tr} and θ_1 yields

$$\frac{1}{\Gamma}\frac{d\Gamma}{d\cos\theta_{tr}} = \frac{3}{4}(1-R_\perp)\sin^2\theta_{tr} + \frac{3}{2}R_\perp\cos^2\theta_{tr}\ , \tag{2.40}$$

where

$$R_\perp = \frac{|A_\perp^0|^2}{|A_0^0|^2+|A_\parallel^0|^2+|A_\perp^0|^2}\,, \tag{2.41}$$

where the ^{0} superscript denotes the value of the amplitude at $t=0$. This means that the CP-odd fraction can be extracted from a one-dimensional, one-parameter

fit. To this point, *BABAR* [23] analyses of *CP* violation in the $B^0 \to D^{*+}D^{*-}$ decay have followed this approach, measuring $R_\perp = 0.125 \pm 0.044(\text{stat}) \pm 0.007(\text{syst})$. The Belle Collaboration has also measured $R_\perp = 0.19 \pm 0.08 \pm 0.01$ [24].

For a time dependent *CP* analysis of the $B^0 \to D^{*+}D^{*-}$ decay, the explicit time dependence of the amplitudes in Eq. 2.37 is

$$A_j(t) = \frac{\sqrt{2}A_j^0}{\sqrt{1+|\lambda_j|^2}} e^{-imt-\Gamma t/2}\left(\cos\frac{\Delta m_d t}{2} + i\eta_j\lambda_j \sin\frac{\Delta m_d t}{2}\right) , \tag{2.42}$$

where $j = \perp, \|, 0$ and η_j is the *CP* eigenvalue for the j^{th} amplitude, 1 for $j = \|, 0$ and -1 for $j = \perp$. The different *CP* parameters λ_j arise from the fact that the relative contribution of the penguin diagrams need not be the same for the three transversity amplitudes. This means that in Eq. 2.19 there is a cosine coefficient, C_j, and a sine coefficient, S_j, for each of the three transversities,

$$\begin{aligned} C_j &= \frac{1-|\lambda_j|^2}{1+|\lambda_j|^2} \\ S_j &= \frac{2\,\text{Im}\lambda_j}{1+|\lambda_j|^2} \ . \end{aligned} \tag{2.43}$$

In the limit of no penguin contribution, $\lambda_j = \lambda$ for all three amplitudes and is the same as for the $B^0 \to J/\psi K_S^0$ mode. Being able to determine all three λ_j's is contingent on determining the three A_j^0's from a full time-dependent angular analysis.

2.4 Full angular analysis measurement

The amplitudes A_j^0 in Eq. 2.42 represent six degrees of freedom—three magnitudes and three phases. One magnitude is constrained via normalization, and only

the two phase differences are physically relevant, leaving only 4 free parameters. The determination of three of these parameters is possible using a flavor-averaged, time-integrated, full angular analysis. In such a case, Eq. 2.37 becomes

$$\frac{1}{\Gamma}\frac{d^3\Gamma}{d\cos\theta_1 d\cos\theta_{tr} d\phi_{tr}} = \frac{9}{16\pi}\frac{1}{|A_0^0|^2+|A_\parallel^0|^2+|A_\perp^0|^2}\times$$
$$\Big\{2\cos^2\theta_1\sin^2\theta_{tr}\cos^2\phi_{tr}|A_0^0|^2+\sin^2\theta_1\sin^2\theta_{tr}\sin^2\phi_{tr}|A_\parallel^0|^2$$
$$+\sin^2\theta_1\cos^2\theta_{tr}|A_\perp^0|^2+\frac{1}{\sqrt{2}}\sin 2\theta_1\sin^2\theta_{tr}\sin 2\phi_{tr}\,\mathrm{Re}(A_0^{0*}A_\parallel^0)\Big\}\ , \qquad (2.44)$$

which can be used to extract the parameters in a three-dimensional angular fit. Using factorization, the three magnitudes have been computed to be $|A_0^0|^2 = 0.55$, $|A_\parallel^0|^2 = 0.39$, and $|A_\perp^0|^2 = 0.06$ [25], which is in agreement with calculations done by Ref. [19] and Ref. [26].

A full angular analysis would test the predictions of the factorization models for this and similar decays and enable better models to be computed. Large deviations in the measured parameters from the predictions could signal a larger than expected penguin contribution or contributions from physics beyond the Standard Model. In addition including the time dependence of the A_j in a full time-dependent, angular analysis would be sensitive to $\cos 2\beta$, helping to reduce the trigonometric ambiguity in the determination of β from $\sin 2\beta$. To this point, observations in the $B^0 \to D^{*+}D^{*-}$ mode have been consistent with Standard Model predictions within the statistical and systematic errors. However, to date, a full angular analysis has not been performed.

2.5 Summary

The $B^0 \to D^{*+}D^{*-}$ decay provides an important cross check to the sin2β measurements through other channels. A full angular analysis could also provide insight into the contribution of penguin diagrams to this mode and provide feedback to models based on factorization. Large deviations from the Standard Model predictions could signal larger penguin contributions and lead to improved models of hadronic decays, or it could point the way for discovery of processes mediated by processes beyond the Standard Model [27, 28, 29]. The $B^0 \to D^{*+}D^{*-}$ decay provides a window into several aspects of the Standard Model and provides avenues to future discovery.

Chapter 3

PEP-II B Factory and the *BABAR* Detector

In 1987, Pier Oddone proposed that an asymmetric e^+e^- collider would be an ideal environment to study *CP* violation in the B meson decays at the $\Upsilon(4S)$ resonance. From this was born the B Factory, a high-luminosity, asymmetric collider designed to produce millions of $B\overline{B}$ pairs annually for the study of *CP* violation and other rare processes.

Data used in this dissertation was collected using the *BABAR* detector at the PEP-II B Factory at the Stanford Linear Accelerator Center (SLAC) between 1999 and 2007. The total integrated luminosity at the $\Upsilon(4S)$ resonance is $425.7\,\text{fb}^{-1}$ totaling $(467 \pm 5) \times 10^6$ $B\overline{B}$ pairs.

In this chapter, I provide an overview of PEP-II and the *BABAR* detector, drawings of which are in Figs. 3.1 and 3.2. A more complete description of the *BABAR* detector is contained in Ref. [30] from which much of the content of this chapter is derived.

3.1 PEP-II

The PEP-II B Factory is an asymmetric e^+e^- collider using the main SLAC linac as the injector. A 9 GeV electron beam collides with a 3.1 GeV positron beam at the $\Upsilon(4S)$ resonance. The $\Upsilon(4S)$ decays into coherent pairs of $B\overline{B}$ mesons, which

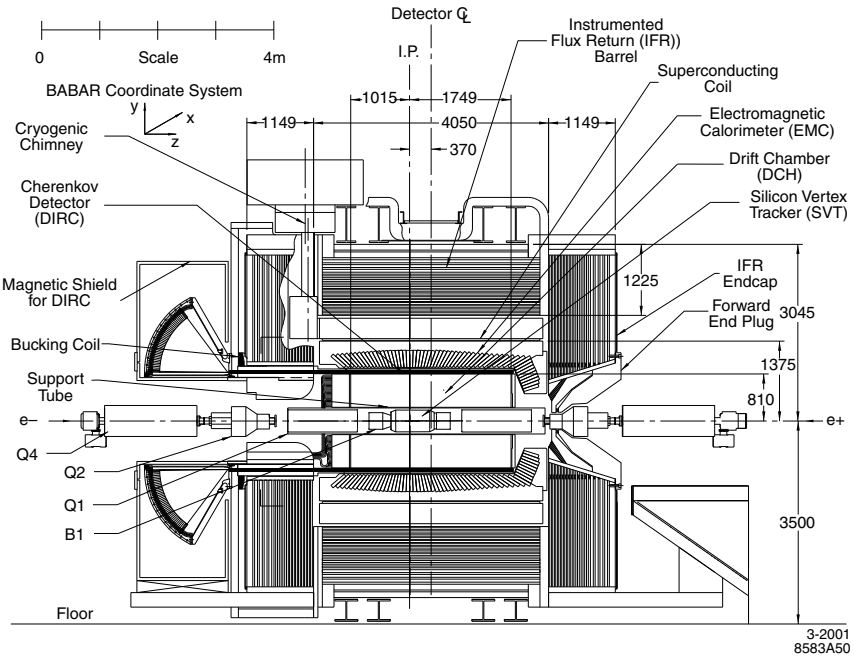

Figure 3.1: A drawing of the *BABAR* detector in the $y - z$ plane.

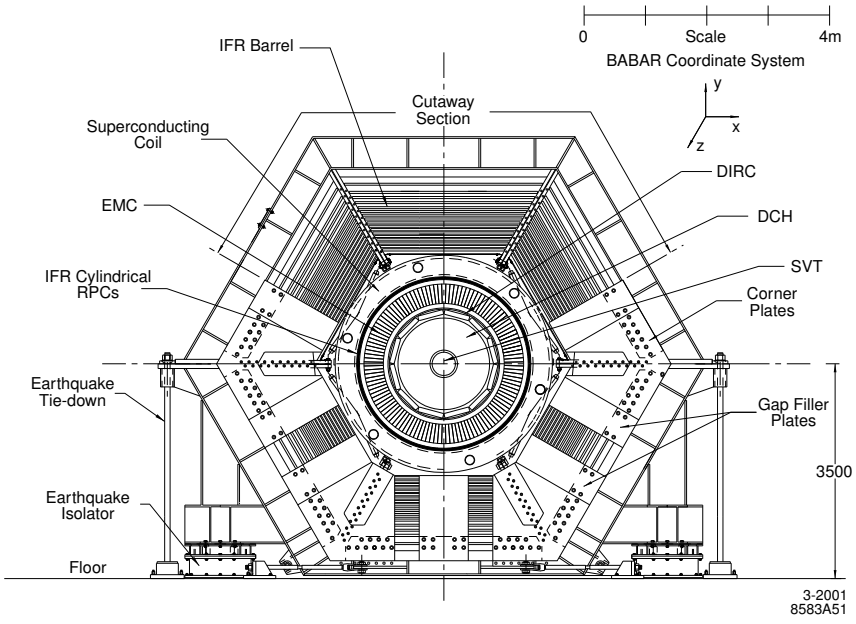

Figure 3.2: A drawing of the *BABAR* detector in the $x - y$ plane.

	Design		Current	
Parameter	HER	LER	HER	LER
Energy (GeV)	8.99	3.1	8.99	3.1
Current (mA)	750	2140	1900	3000
RF voltage (MV)	14.0	3.4	16.0	4.05
Number of bunches	1658		1730	
Bunch Length (mm)	11		12.5	13.5
Horizontal emittance (nm)	49		73	36
Vertical emittance (nm)	2		1	1
β_y^* (mm)	15–25		11	10
β_x^* (cm)	50		74	21
ξ_y	0.03		0.074	0.058
Luminosity ($\times 10^{33}\,\mathrm{cm}^{-2}\mathrm{s}^{-1}$)	3.0		12	

Table 3.1: PEP-II design and current parameters.

provide an rich laboratory to study time-dependent *CP* phenomena. Because of the beam's asymmetric energies, the $\Upsilon(4S)$ has a boost of $\beta\gamma = 0.56$ with respect to the lab frame, which allows for the resolution of the decay vertices of the two B daughters.

PEP-II consists of the refurbished PEP storage ring that serves as the high-energy ring (HER) and a new low energy storage ring (LER). The design instantaneous luminosity goal was $3 \times 10^{33}\,\mathrm{cm}^{-2}\mathrm{s}^{-1}$, however the the instantaneous luminosity has since topped out at $1.2 \times 10^{34}\,\mathrm{cm}^{-2}\mathrm{s}^{-1}$ [31]. Additional design and typical operating values for PEP-II are in Table 3.1. First collisions were established in PEP-II in July 1998. The data taking at the *BABAR* detector began in May 1999, and the last $\Upsilon(4S)$ data was taken in December 2007, after which data was taken at the $\Upsilon(3S)$ and $\Upsilon(1S)$ resonances as well as scanning above the $\Upsilon(4S)$. Data taking with *BABAR* ended in April 2008.

Table 3.2 shows the cross-section breakdown at the $\Upsilon(4S)$ resonance. At this

$e^+e^- \rightarrow$	Cross-section (nb)
$b\overline{b}$	1.05
$c\overline{c}$	1.30
$s\overline{s}$	0.35
$u\overline{u}$	1.39
$d\overline{d}$	0.35
$\tau^+\tau^-$	0.94
$\mu^+\mu^-$	1.16
e^+e^-	~ 40

Table 3.2: Cross-sections at $\sqrt{s} = E_{\Upsilon(4S)}$

energy the $B\overline{B}$ cross-section accounts for roughly one quarter of the total $q\overline{q}$ cross-section.

The *BABAR* detector has been designed to capitalize on the asymmetric characteristics of PEP-II and study rare processes at $\sqrt{s} = E_{\Upsilon(4S)}$. The detector is composed of several components The inner most component is a silicon vertex tracker used to provide the precise vertex measurements critical to time-dependent *CP* violation measurements. This is surrounded by a drift chamber, an imaging Cherenkov detector and an electromagnetic calorimeter. These detectors reside within the 1.5 T solenoid. The flux retrun of the solenoid is also instrumented with resistive plate chambers and limited streamer tubes to identify and track muons. Each of these detector systems as well as the electronics and computing which support them are described in the remaining sections of this chapter.

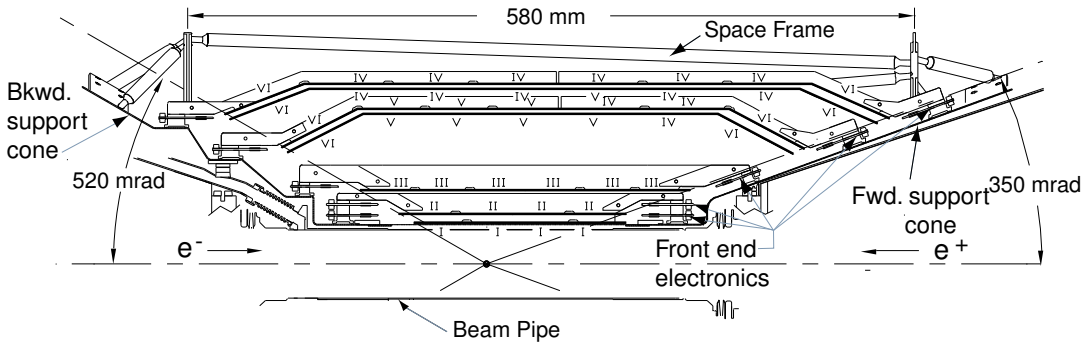

Figure 3.3: Drawing of the SVT: longitudinal section.

3.2 Silicon Vertex Tracker (SVT)

To provide the precise decay vertex information required for time-dependent *CP* measurements, *BABAR* uses a five-layer silicon vertex tracker (SVT). The design of the SVT is dominated by the need to provide sub-100 μm vertex resolution and achieve stand-alone tracking capabilities for tracks with a transverse momentum down to 50 MeV/c. To achieve these goals, *BABAR* employs a 5-layer SVT consisting of two-sided silicon sensors. The innermost layer is just 3.4 cm in radius while the outermost portions of the detector are 14.4 cm in radius. Figures 3.3 and 3.4 show the design and orientation of the SVT layers and their constituent sensors. The outer two layers are arched to increase the coverage without increasing the length and to decrease the crossing angle.

The SVT sensors are 300 μm thick double-sided silicon strip devices. They use high resistivity n-type substrates with p^+ strips on one side and n^+ strips on the other. The ϕ strips are bonded from the center to each end where they are read

Layer/ view	Radius (mm)	Readout pitch (μm)	Floating strips	Strip length (mm)
$1z$	32	100	1	40
1ϕ	32	50–100	0–1	82
$2z$	40	100	1	48
2ϕ	40	55–110	0–1	88
$3z$	54	100	1	70
3ϕ	54	110	1	128
$4z$	91–127	210	1	104
4ϕ	91–127	100	1	224
$5z$	114–144	210	1	104
5ϕ	114–144	100	1	265

Table 3.3: Parameters of the SVT sensors by layer and side.

out. The z strips are brought to the ends via traces; layers four and five gang two strips together to reduce the number of readout channels. Table 3.3 contains the specifics of the strip pitch and dimensions of the sensors in each layer. The typical depletion voltage is 25–35 V and the sensors are operated at about 10 V above their depletion. To reduce channel noise, the inter-strip capacitance and series resistance were kept to a minimum.

3.2.1 SVT electronics

To meet the stringent requirements of for high signal to noise, flexibility, precision and radiation hardness, the *BABAR* SVT uses the custom-built ATOM (A Time-Over-threshold Machine) IC depicted in Fig. 3.5 for the data readout. The ATOM chips output a digital time-over-threshold signal whose width is a quasi-logarithmic function of the integrated charge. After a L1 accept the hits are digitized by the ATOM chips and shipped out of the detector to the link cards where they are mul-

tiplexed onto fibers and sent to the read-out modules (ROM). Power and control commands are passed in to the SVT through the link cards also. The entire SVT system is represented schematically in Fig. 3.6.

3.2.2 SVT radiation monitoring (SVTRAD)

Because of its critical function and close proximity to the beam line, the SVT is monitored for exceptional radiation by a system of radiation sensors. Intense radiation can cause acute damage to the silicon sensors by creating pinhole shorts in the coupling capacitors or p-stop shorts between the p-stops and the metal. There is also damage caused by prolonged exposure where silicon atoms are displaced from the bulk leading to imperfections that decrease charge collection efficiency, increase leakage current and depletion voltage, and eventually lead to type inversion. To protect the SVT, there are 12 silicon photo diodes and two CVD diamond sensors which monitor the radiation environment and have the ability to abort the PEP beams should the conditions become bad. In this way *BABAR* has been able to protect the SVT from severe damage throughout the lifetime of the experiment.

3.2.3 SVT performance

The *BABAR* SVT has maintained high performance throughout data taking. The average hit efficiency is 97%. Resolution has exceeded the design specifications with z resolution at 10–40 μm. (Resolutions by layer for both z and ϕ are in Fig. 3.7.) The final state of the $B^0 \to D^{*+}D^{*-}$ decay has two slow pions from

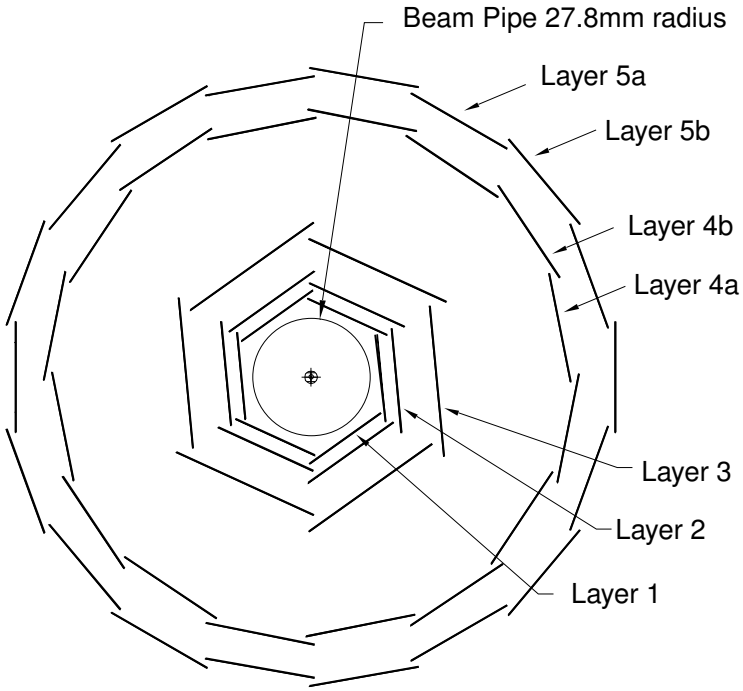

Figure 3.4: Drawing of the SVT: transverse section.

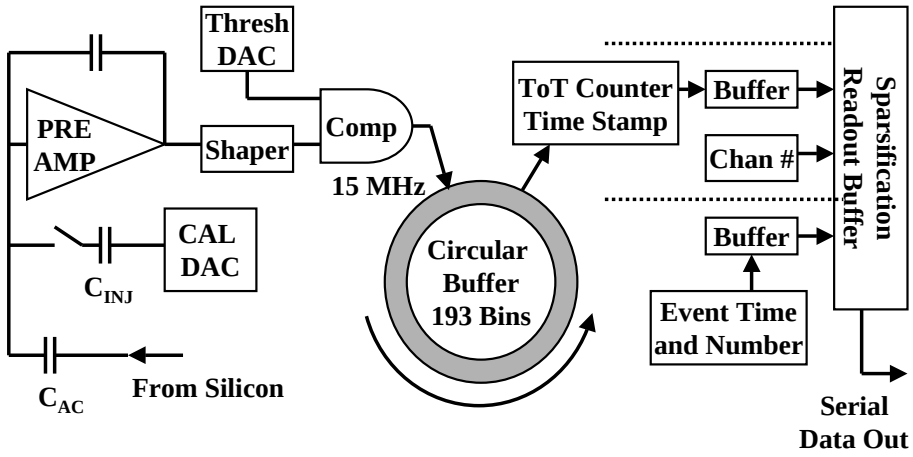

Figure 3.5: Schematic diagram for the ATOM chip circuitry for a single channel.

decays of the the two D^* mesons. Accurately and efficiently reconstructing these low momentum tracks can be a significant challenge. The *BABAR* SVT achieves a slow pion efficiency of better than 70% for pions with a transverse momentum greater than 50 MeV/c.

3.3 Drift Chamber (DCH)

The *BABAR* drift chamber (DCH) provides charged particle tracking and momentum measurement. It is nearly 3 m long and occupies the radial space from 23.6 cm to 80.9 cm, enclosing a volume of 5.2 m^3. The DCH is a small cell drift chamber with 40 layers of hexagonal cells, divided by fours into 10 superlayers. Fig. 3.8 depicts a transverse view of the first 4 superlayers. Each of the 7104 cells in the DCH has a tungsten-rhenium sense wire at the center, which is held at less than 1960 V, surrounded by aluminum field wires maintained at ground. To improve the field contours between superlayers guard wires at 340 V replace the field wires. The superlayers repeatedly alternate "stereo" angle from zero to a positive then negative angle with respect to the z-axis of the chamber. This alternation provides sensitivity to the z position within the chamber.

The DCH is filled with an 80:20 mixture of helium and isobutane. This has a much longer radiation length than argon based gas mixtures and has a smaller Lorentz angle, improving spatial resolution. The gas is kept at 4 mbar above atmospheric pressure and at a humidity of 3500 ppm. There are typically 21 primary ions per track per cell.

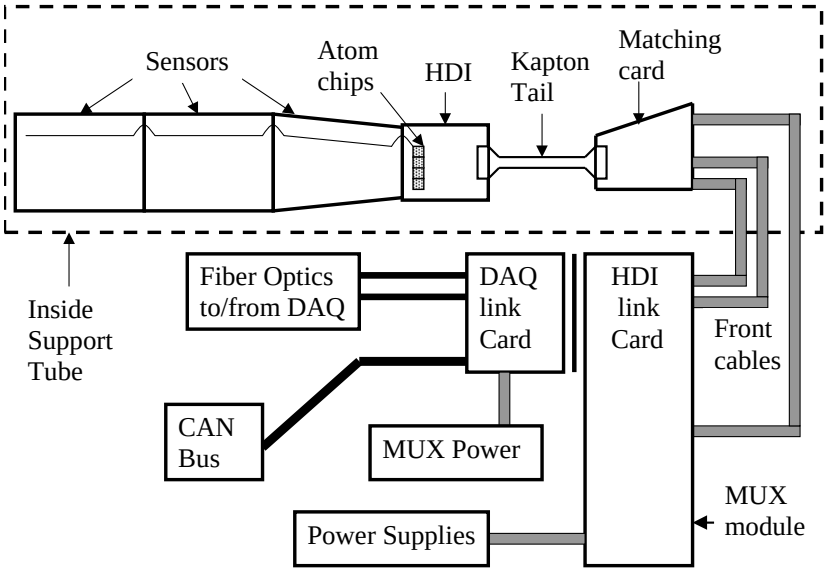

Figure 3.6: Block diagram of the SVT including power and DAQ.

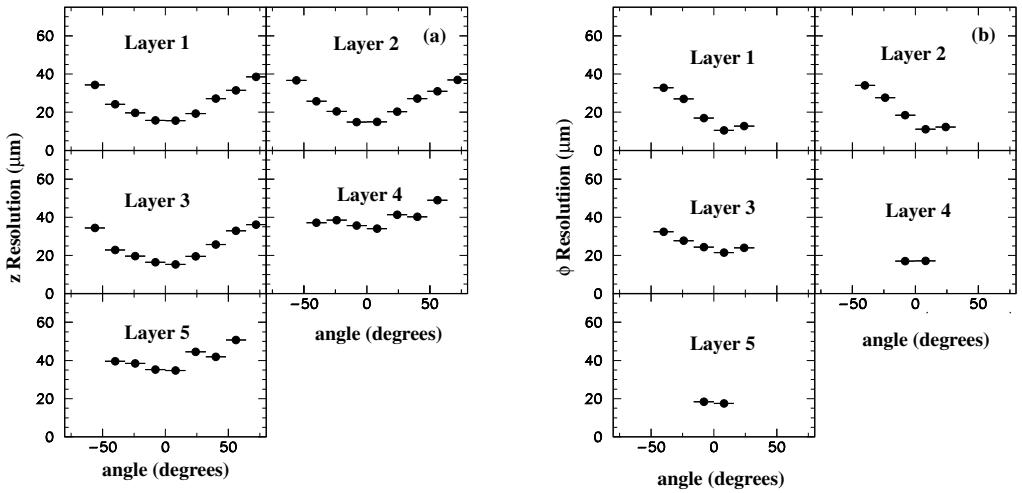

(a) z hit resolution

(b) ϕ hit resolution in μm along the surface of the sensor

Figure 3.7: SVT hit resolution.

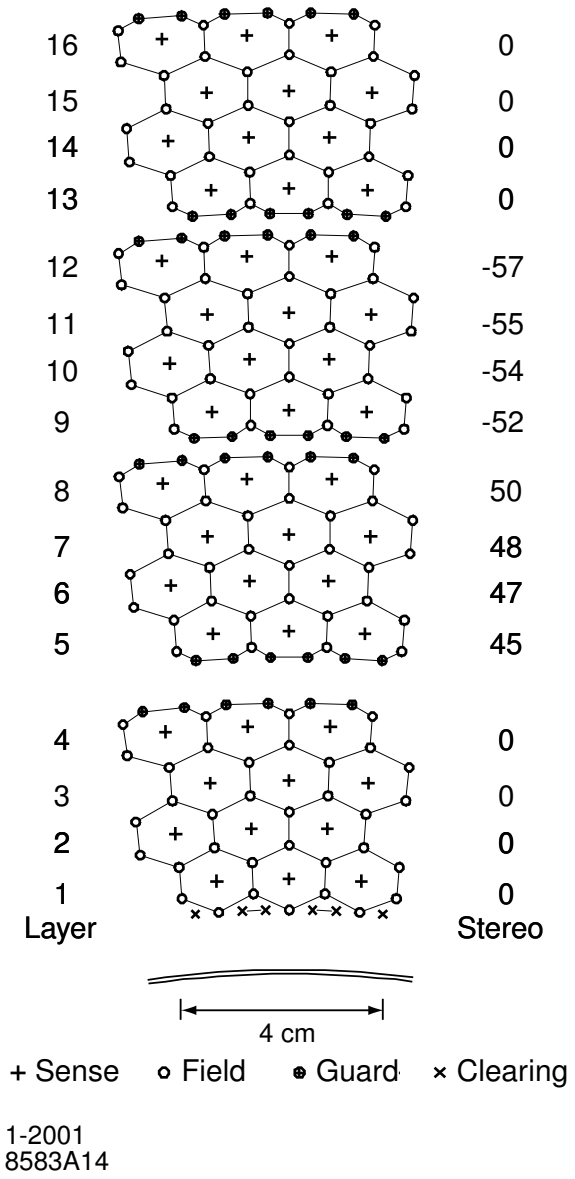

Figure 3.8: Schematic layout of the first four superlayers of the DCH. Lines have been added between the field wires to demarcate the cells.

DCH high voltage and readout electronics are all located on the backward end plate in order to minimize the material in front of the forward calorimeter. The DCH measures both drift time and accumulated charge. Readout via 16 sectors takes place when a L1 trigger is received. Time-to-distance relationships are derived offline from e^+e^- and $\mu^+\mu^-$ events and applied during tracking. Energy loss in the DCH, $\mathrm{d}E/\mathrm{d}x$, is also recorded and calibrated for use in particle identification. Typical $\mathrm{d}E/\mathrm{d}x$ resolution for Bhabha events is 7.5%.

3.4 Detector of Internally Reflected Cherenkov Light (DIRC)

Flavor tagging at *BABAR* requires charged particle identification to find kaons from $b \to c \to s$ decays that distinguish the B and $\overline{B}$ mesons. These kaons have momenta up to 2 GeV/c; however, most lie below 1 GeV/c. In addition, background suppression for the rare $B^0 \to \pi^+\pi^-$ decay from $B^0 \to K^\pm\pi^\mp$ or $B^0 \to K^+K^-$ is important to enable the measurement of the CKM angle α. The momenta of these pions lies from 1.7 GeV/c to 4.2 GeV/c. In order to meet these requirements, *BABAR* employs a novel ring imaging Cherenkov (RICH) detector. The Detector of Internally Reflected Cherenkov light (DIRC) provides K/π separation from about 0.7 GeV/c to 4.2 GeV/c. A brief description of this detector follows. Much of the material in this section is summarized from the more complete description in Ref. [32].

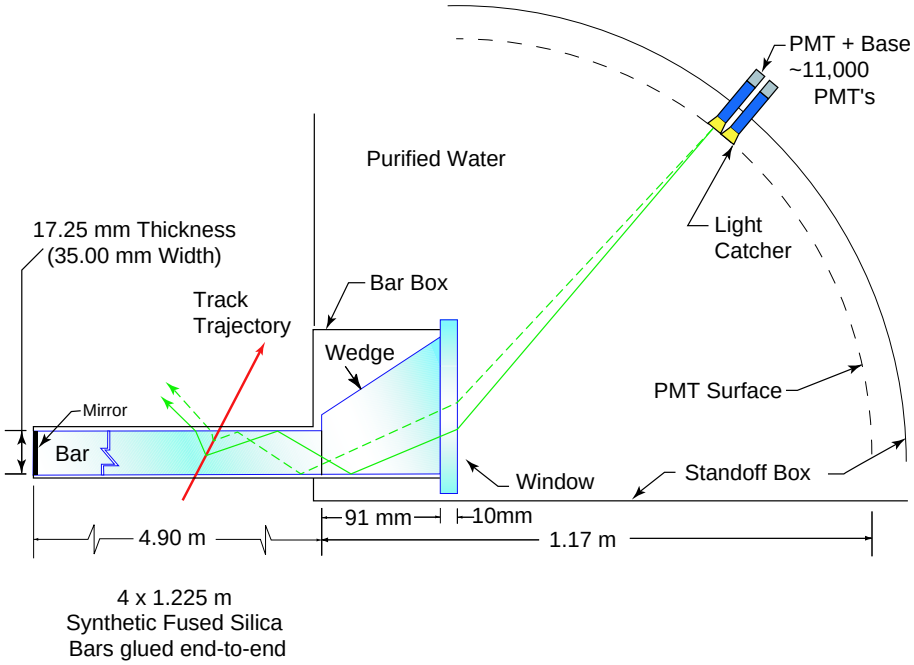

Figure 3.9: Schematic of principles of the DIRC detector.

3.4.1 DIRC construction

The DIRC uses internally reflected photons rather than transmitted photons to reconstruct the Cherenkov angle, $\cos\theta_C = 1/n\beta$, of particles passing through it. This novel approach was proposed by Blair Ratcliff in 1992 [33]. Its design minimizes the amount of material in front of the calorimeter, improving energy resolution.

As depicted in Fig. 3.9, the Cherenkov photons are generated in one of 144 synthetic fused silica bars ($n \approx 1.473$), which also transmits the internally reflected photons to the backward portion of the detector where they are imaged. Synthetic fused silica was used because of its small radiation length, radiation hardness, long attenuation length, small chromatic dispersion, and ability to achieve fine optical polish.

The silica bars of the DIRC are rectangular to within very strict tolerances—

35 mm wide, 12.25 mm thick, and 4.9 m long—with transmission coefficients of better than 98%/m. In order to perserve θ_C the faces are parallel to better than 25 μm. Each bar is attached to a silica wedge, which is attached to a silica window, that allows the internally reflected light to expand into the water-filled standoff box (SOB), where it is imaged onto photomultiplier tubes (PMTs). Twelve bars, their wedges and window are grouped into a sector, with twelve sectors in *BABAR*.

The Cherenkov photons are imaged in an array 10752 PMTs, with 26 mm photocathodes, on the toroidal surface of the SOB. Each PMT is fitted with a rhodium-plated, hexagonal light-catcher to reflect photons that would otherwise be lost onto the active area of the PMT, thereby increasing the active area of the detection surface to 90%. The PMTs and their HV bases provide timing resolution for hits down to 1.5 ns.

3.4.2 DIRC electronics and reconstruction

Data arrives from the phototubes in front-end boards where it is amplified, digitized and buffered. When there is a L1 trigger accept, these boards transfer data to the readout module (ROM), which performs data reduction by a cut on out-of-time hits and feature extraction before passing the data on for reconstruction. The electronics allow calibration of PMT gain and detector time response using a blue LED pulser for each sector in the SOB and using calibrations from the first 100k tracks from live data. These two calibration approaches yield consistent, stable results.

Event reconstruction associates PMT hits with tracks and performs particle identification. In the first step, PMT hits are associated to tracks using information from the DCH and hit times to disentangle ambiguities between backgrounds and other tracks in the event, and the track is assigned Cherenkov angles (θ_C, ϕ_C). In the second phase, the tracks are globally fit using an unbinned maximum likelihood formalism to determine their species (e, μ, π, K, or p). The overall $\Delta\theta_C$ for tracks is 2.5 mrad as measured using di-muon events. K/π separation is greater than 4σ up to momenta of 3 GeV/c and is still 2.5σ at 4.1 GeV/c.

Particle identification (PID) also comes from $\mathrm{d}E/\mathrm{d}x$ measurements in the SVT and DCH. In particular, in the momentum regime from 0.5 GeV/c to 1.5 GeV/c, $\mathrm{d}E/\mathrm{d}x$ information from the DCH is combined with the likelihood information from the DIRC to create a smooth transition for particle identification power as the primary PID detector shifts from the DCH to DIRC.

3.5 Electromagnetic Calorimeter (EMC)

The principle purpose of the *BABAR* electromagnetic calorimeter (EMC) is to provide reconstruction of photons and identification of electrons. The EMC detects electromagnetic showers ranging in energy from 20 MeV to 9 GeV. To measure extremely rare decays like $B^0 \to \pi^0\pi^0$, the EMC needs energy resolution of order 1–2%, and angular resolution of a few mrad. The EMC must also be capable of operating inside the 1.5 T *BABAR* solenoid.

To achieve these requirements the *BABAR* detector employs a calorimeter com-

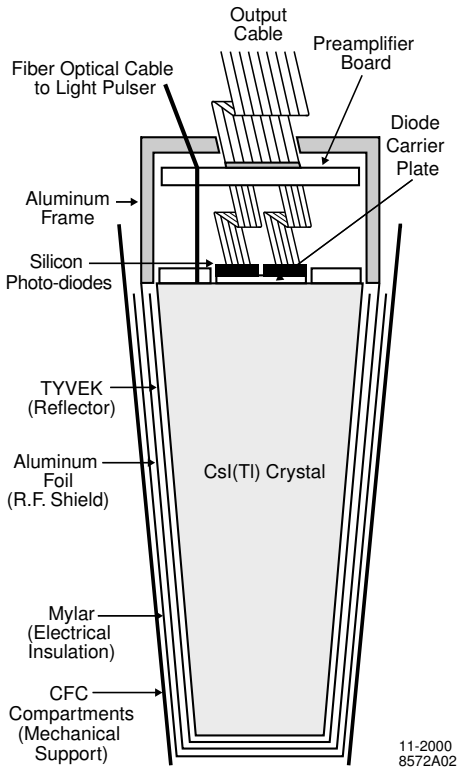

Figure 3.10: Drawing of the a single EMC crystal.

posed of thallium-doped cesium iodide (CsI(Tl)) crystals. These crystals are read out using silicon photodiodes matched to the scintillation spectrum of the crystals. Figure 3.10 shows a schematic diagram of a single crystal. These crystals are arranged in a carbon-fiber-epoxy (CFC) supports in 48 rings of 120 crystals in the barrel and 8 rings of 80–120 crystals in the forward endcap, as depicted in Fig. 3.11. This provides 90% coverage of the CM frame. There is no more than 0.6 radiation lengths in front of the barrel crystals and only 3 radiation lengths before the inner-most endcap crystals.

Two silicon photodiodes collect the scintillation light from each crystal, which is in turn amplified on the crystal before being sent on to the EMC crates for further

amplification and digitization before being shipped to the ROMs. The EMC electronics continuously read out the entire detector to the ROMs unlike other detectors which are only read out in full after a L1 accept.

The EMC is calibrated at low energies using a 6.13 MeV photon from a radioactive source that can flow in front of the crystals. At higher energies, Bhabha events are used and the energy is matched to GEANT-based simulation. Intermediate energies rely on logarithmic interpolation from the low and high energy regimes. Radiative Bhabha events are used for cluster energy corrections.

From the energy calibrations, we determine the energy resolution of the EMC. At low energy, it is $(5.0 \pm 0.8)\%$; at high energy, $(1.9 \pm 0.07)\%$. At the intermediate energys, decays of π^0, η, and $\chi_{c1} \to J/\psi\,\gamma$ are used, resulting in an energy dependence

$$\frac{\sigma_E}{E} = \frac{(2.32 \pm 0.03)\%}{\sqrt[4]{E(\,\mathrm{GeV})}} \oplus (1.85 \pm 0.12)\%\,,$$

higher than the design expectations, but in agreement with MC simulations. The angular resolution, determined from π^0 and η decays, is empirically parameterized as

$$\sigma_\theta = \sigma_\phi = \left(\frac{3.87 \pm 0.07}{\sqrt{E(\,\mathrm{GeV})}} \oplus 0.00 \pm 0.04 \right) \mathrm{mrad}\,,$$

slightly better than expected from MC simulations. When combining information from the DCH, DIRC, and EMC, tight electron selectors achieve 94.8% efficiency with only 0.3% pion misidentification rate for momenta in the range $0.5 < p < 2$ GeV/c.

3.6 Instrumented Flux Return (IFR)

The steel of the flux return of the *BABAR* solenoid is interleaved with detector layers to provide muon and neutral hadron identification. The instrumented flux return (IFR) plays an important role in the reconstruction of muons for B flavor tagging, J/ψ reconstruction, semi-leptonic b and c decays, τ decays, and K_L^0 detection for CP studies.

The *BABAR* IFR originally consisted of interleaved layers of steel with resistive plate chambers (RPCs). The RPC system was based on chambers using Bakelite as the resistive plates rather than the more traditional glass. The setup for a *BABAR* RPC is in Fig. 3.12. Initially, these detectors provided excellent timing, large signals, and high efficiency. Soon after installation, many RPC modules suffered dramatic losses in efficiency. This was later traced to manufacturing problems problems with the linseed oil coating on the inner surfaces of the Bakelite that would cause it to break down, drip and run at higher temperatures. This led to upgraded RPCs being installed in the forward endcap and eventually the complete upgrade of the barrel muon system to a limited streamer tube (LST) based detector [34].

The LST upgrade at *BABAR* began with the top and bottom sextants of the barrel in the summer of 2004, and was expanded to the entire barrel in the fall of 2006. The *BABAR* LST modules, seen in Fig. 3.13, consist of gold plated anode wire within a PVC tube. In conjunction with z-planes installed perpendicular to the anode wires, the new LST system is able to provide effective tracking information on muons. Since their installation the IFR efficiency has recovered and even exceeds

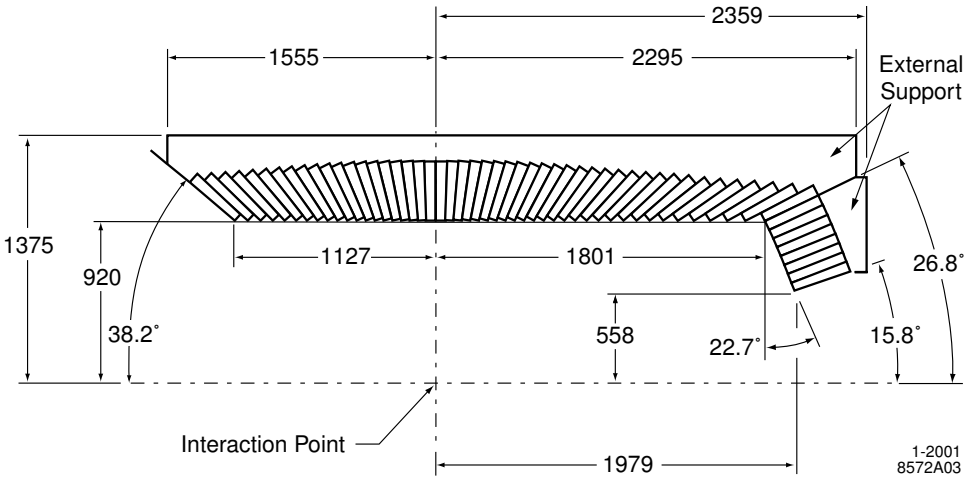

Figure 3.11: Top half of the longitudinal cross-section of the EMC showing the arrangement of the crystals. Dimensions are given in mm.

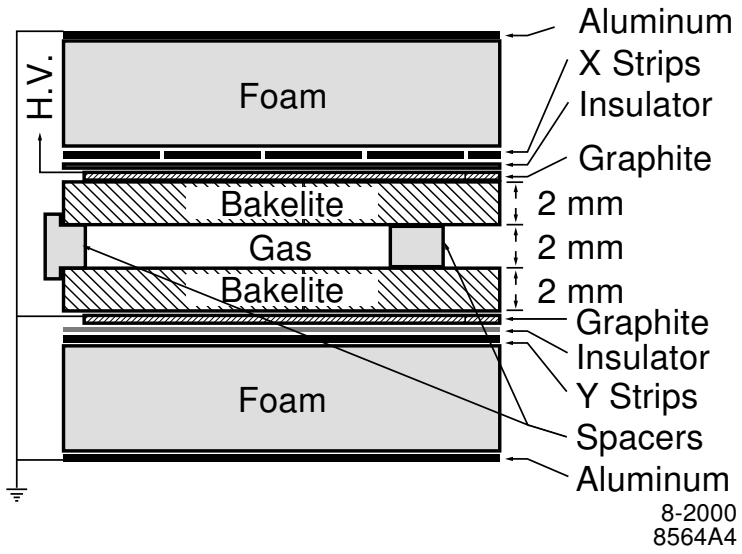

Figure 3.12: Cross-section of an RPC with the schematics of the high voltage connection.

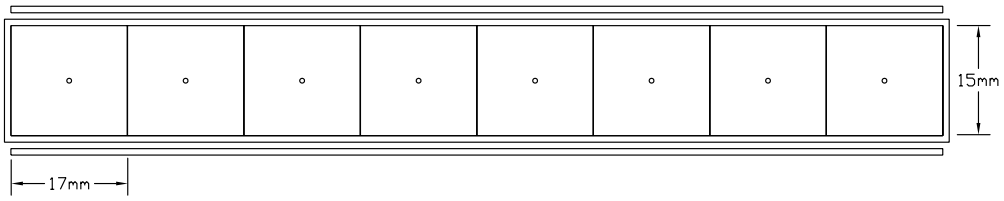

Figure 3.13: Cross-section of an LST.

the original RPC system, see Fig. 3.14.

The RPC detector uses a gas mixture of 60% argon, 35.6% freon and 4.4% isobutane. The LSTs use 89% carbon dioxide, 3% argon and 8% isobutane. The RPC HV is up to 10 kV while the LSTs operate at 5.5 kV.

Muon candidates are identified in the IFR using information from the SVT and DCH to extrapolate tracks into the IFR accounting for non-uniform magnetic fields, multiple scattering and average energy loss. Variables used to discriminate muons include: the predicted vs. measured number of interaction lengths transversed, the number and width of the hits per layer, the χ^2 for the geometric match of the cluster centroids and the projected track, and the χ^2 of a polynomial fit to the two-dimensional IFR clusters. Using these variables, the *BABAR* IFR achieves 90% efficiency for muon detection for the momentum range $1.5 < p < 3.0$ GeV/c with a fake rate from pions of 6–8%. Tighter selection is also possible, see Fig. 3.14.

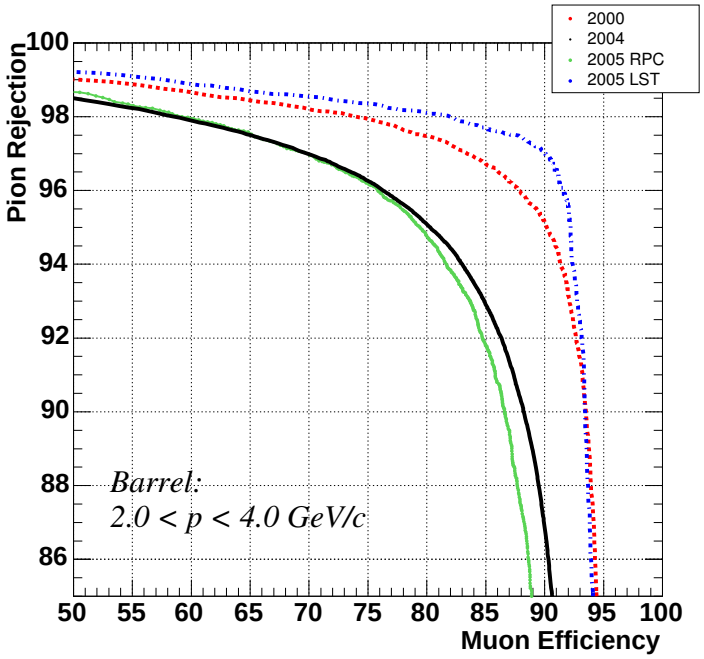

Figure 3.14: Muon efficiency of the barrel system. The dashed red curve is the original RPC installation; the solid back were the RPCs in 2004; the solid green is the RPCs in 2005; and the dotted blue is the LSTs in 2005.

3.7 The *BABAR* trigger, DAQ and computing systems

The *BABAR* online computing systems are a critical portion of the experiment, responsible for data acquisition and processing as well as monitoring general detector health and basic data quality.

The *BABAR* trigger system requires high efficiency to collect physics events while maintaining excellent background rejection. The trigger system can regularly sustain a final output of around 300 Hz. Priority is given to $B\overline{B}$ events where we require 99% efficiency. In addition, we require 95% efficiency for continuum events and 90–95% efficiency for $\tau^+\tau^-$ events. The *BABAR* trigger is an open trigger, striving to capture all interesting events.

3.7.1 Level 1 (L1) trigger

The Level 1 (L1) trigger uses data from the DCH, EMC, and IFR to determine when the full detector should be read out. The L1 trigger system is depicted schematically in Fig. 3.15. The trigger setup allows for redundancy and orthogonal triggering to measure efficiencies and ensure broad coverage of interesting events.

For the DCH data, the track segment finder (TSF) modules process the data looking for 3- or 4-layer track segments within an eight-cell pivot group of a DCH superlayer that point back to the interaction region. The TSF modules pass the segments to the binary link tracker (BLT), which links the segments into longer tracks, and to a transverse momentum discriminator (PTD), which is able to extract high momentum tracks from the segments in the axial superlayers. After the *BABAR*

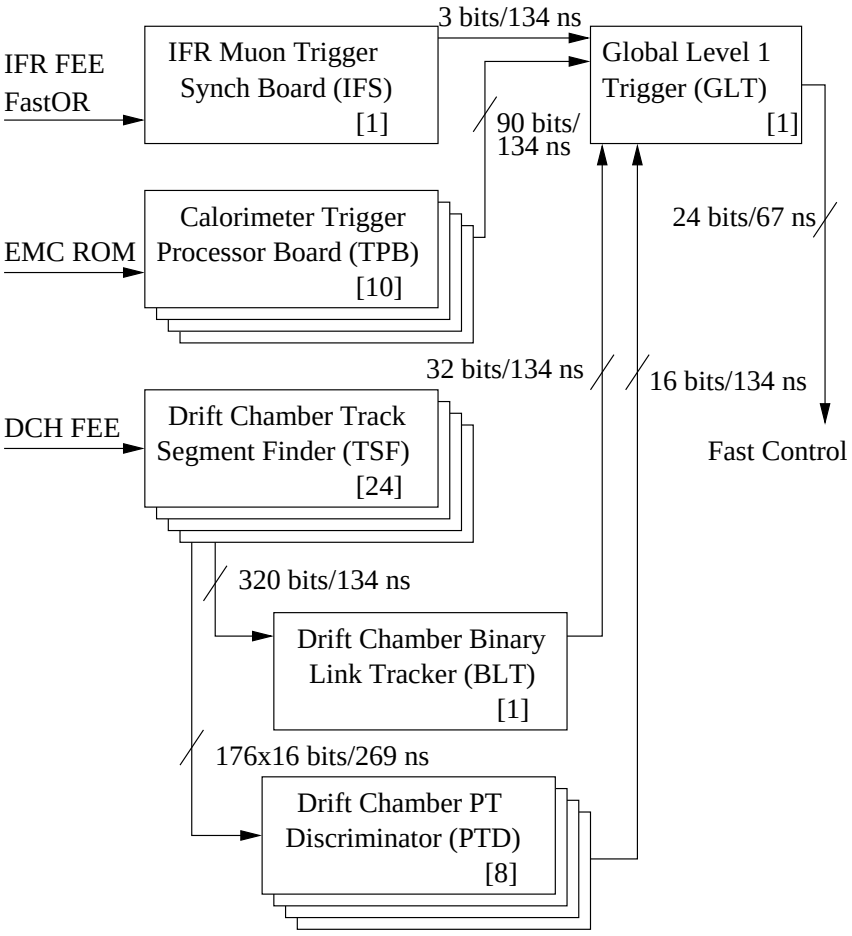

Figure 3.15: A schematic representation of the L1 trigger.

Run 4 the PTDs were replaced with z_0-$p_{\rm T}$ discriminators (ZPDs) which also allowed determination of the z_0 of a track to about 4 cm, and a cut could be used to reject beam-pipe interactions.

For triggering the EMC is partitioned into 280 towers (240 barrel and 40 end-cap) each of which reports the sum of the crystal energies over 20 MeV. EMC data is collected by the calorimeter trigger processor boards (TPBs) of the electromagnetic trigger (EMT) every 269 ns. The TPBs convert the tower data into ϕ-maps based on thresholds and the estimated time of the energy deposition, corrected for timing jitter.

There is also an IFR trigger (IFT) for triggering on $\mu^+\mu^-$ and cosmic rays. The IFT divides the IFR into 10 sectors (1 per barrel sextant and 1 per end door half). The trigger algorithm creates trigger objects in sectors where 4 of the 8 trigger layers have hits within a 134 ns window.

Trigger ϕ-maps from the BLT, PTDs/ZPDs, EMT and IFT are combined by the global Level 1 trigger (GLT). The GLT performs basic matching between DCH and EMC and calculates the centroid of the timing distribution from the highest priority trigger, rounded to the nearest 67 ns (99% of events lie within 77 ns). If trigger criteria are met, then a L1Accept is generated.

The L1 trigger performance is excellent, with $> 99.9\%$ of generic $B\overline{B}$ events triggered. Specific efficiencies, $\varepsilon_{B\to\tau\nu} = 99.7$, are also excellent. Continuum efficiency is 98–99.9% while $\tau^+\tau^-$ efficiency is 95.4%.

3.7.2 Level 3 (L3) trigger

The Level 3 (L3) trigger runs on a 32-node computer farm. The filters have access to the full event data. L3 refines and augments the selections made in L1. The L3 trigger has three phases. The first is a classification phase that defines the L3 input lines based on a logical OR of the L1 output lines. The second phase comprises pass/fail scripts run on each L3 input line. These scripts can be very general allowing great flexibility in the trigger. The final phase forms the L3 output lines based on a logical OR of selected script flags. At L3, we also monitor luminosity based on well-known cross-sections and efficiencies and calculate event shape variables to produce $B\overline{B}$ enriched datasets from the continuum.

The average time to process an event is 4 ms per event per node. After the L3 trigger, the generic $B\overline{B}$ efficiency is still $> 99.9\%$, and $\varepsilon_{B\to\tau\nu} = 97.8\%$. Continuum efficiency is 96–99% and $\tau^+\tau^-$ efficiency is still 92%. Throughout the lifetime of the *BABAR* experiment, upgrades to the L3 computing farm have allowed for accommodating L1Accept rates upwards of 3 kHz, generated from higher luminosity and background conditions, without degradation of overall trigger performance.

3.7.3 Detector control and monitoring

The *BABAR* detector is controlled through a tightly-integrated online computer environment, depicted in Fig. 3.16. These systems coordinate data acquisition, detector calibration, detector monitoring, triggering, data quality monitoring and data storage. The major subsystems are online dataflow (ODF), online event process-

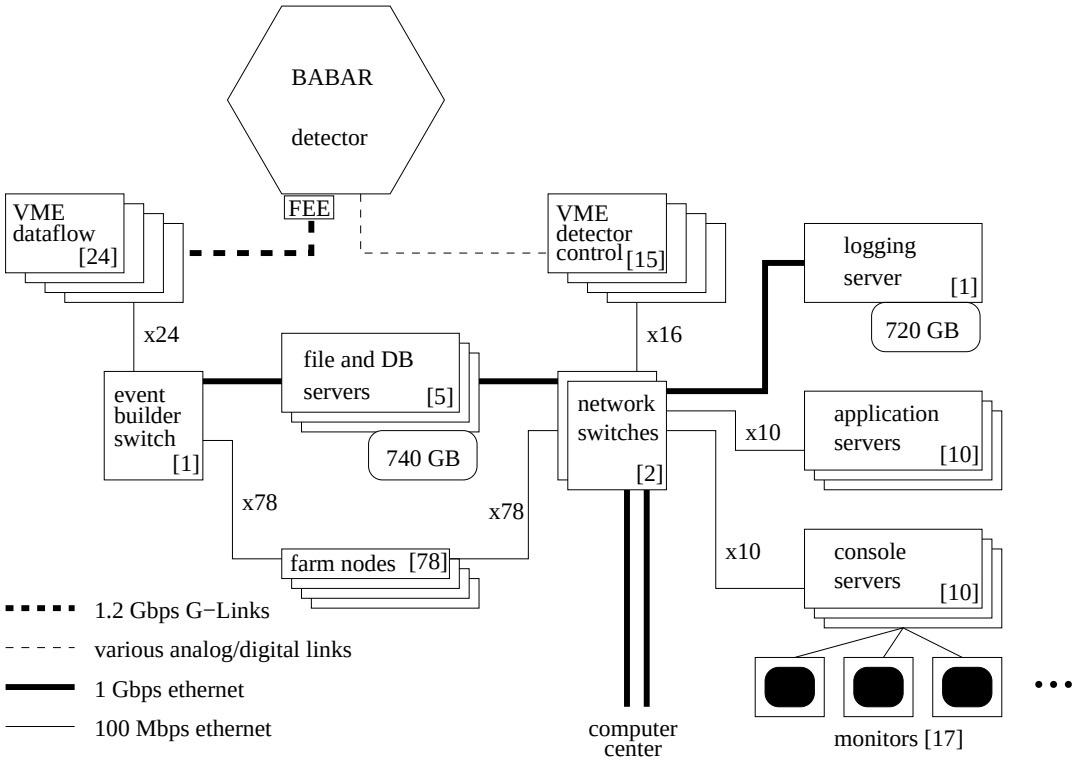

Figure 3.16: A schematic representation of the *BABAR* online computer systems.

ing (OEP), logging manager (LM), online detector control (ODC), and online run control (ORC).

ODF starts on the detector with the front-end electronics which are connected via optical fibers to 157 VME computer based readout modules (ROMs). Each ROM coordinates data acquisition from a portion of the the detector and supplies its data to the event builder which in turn feeds the L3 farm.

OEP hardware consists of the various farm nodes the make up the L3 farm and its associated data storage. The software running on these systems begin event reconstruction and make decisions about what will be saved to permanent storage. The L3 process was outlined in Sec. 3.7.2. Additionally, detector occupancies and reconstructed quantities are passed from L3 to a distributed histogram data as it is

recorded.

The LM system is responsible for writing data that passes all of the trigger and filter layers to permanent storage so that it can be fully reconstructed later.

Monitoring the power supplies, electronics, gas, cooling and environmental systems, as well as PEP-II conditions is the job of the ODC system. The *BABAR* detector uses The Experimental Physics and Industrial Control System (EPICS) as the basis for its ODC system. This system provides information to operators and system experts on the detector hardware, and handles the transitions of PEP-II from injection to data taking modes.

The *BABAR* ORC system configures and initiates data acquisition using the ODC system. It also coordinates detector calibration and monitors essential services needed for efficient data taking. All these systems working together have resulted in very high operational efficiency for the *BABAR* detector.

3.8 Central event reconstruction

After data acquisition by *BABAR*, the data goes through a centralized reconstruction process. Here, tracks and neutral clusters are reconstructed and matched together. Basic PID quantities are computed and tracks and clusters are organized into basic lists.

Charged tracks are reconstructed separately in the SVT and DCH via pattern recognition routines. The two sets of tracks are then combined to form longer tracks. The tracks where an SVT/DCH match cannot be made are kept also, because these

may be low momentum tracks or tracks from particles like K_S^0 which do not originate at the primary vertex. After the pattern recognition routines have formed tracks, they are fit with a simple helix fitter, ignoring material interactions, and then refit with a Kalman filter fitter using a pion mass hypothesis. The Kalman filter fitter includes effects of multiple scattering and energy loss using a detailed detector model. The final vertex fit provides a measurement of the helix parameters for each track.

EMC clusters are formed from from sets of adjacent crystals with energies above 20 MeV. The energy weighted centroid of these clusters is calculated, and they are added to a list of neutral candidates. This list is matched with the track list to separate clusters caused by charged particles from those potentially caused by a neutral particle. In addition, hadronic showers are separated from electromagnetic showers using the lateral energy profile of the cluster, LAT, defined as:

$$\mathrm{LAT} = \frac{\sum_{i=3}^{N} E_i r_i^2}{\sum_{i=3}^{N} E_i r_i^2 + E_1 r_0^2 + E_2 r_0^2}\,, \tag{3.1}$$

where E_i is the energy of the ith crystal in the cluster such that $E_1 > E_2 > ... > E_N$, r_i is the distance from the centroid of the cluster to the center of the ith crystal, and r_0 is the average distance between two crystals, 5 cm in *BABAR*. Electromagnetic showers have a more compact profile than hadronic showers.

After basic reconstruction is completed, the track and neutral candidates are combined into lists meeting different quality criteria. These list form the basis for the reconstruction of composite particles which will be described in the next chapter.

Chapter 4

B meson reconstruction and signal yields

4.1 Data sample

Data used in the results of this dissertation is from the entire the entire *BABAR* data set taken at the $\Upsilon(4S)$ resonance from 1999 to 2007. This represents an on-peak integrated luminosity of 425.6 fb^{-1} and $(467 \pm 5) \times 10^6$ $B\overline{B}$ pairs. Events were taken from the `BToDD` skim, which includes 18 different $B \to D^{(*)}_{(s)} D^{(*)}$ decay modes. The Monte Carlo (MC) that includes full detector simulation used to constrain and validate this analysis was produced through the *BABAR* central MC production. It is based on the `EvtGen` [35] physics generators and uses `GEANT4` [36] for the detector modeling. We use two primary sets of MC with full detector simulation. The first is signal MC, which has has been generated with one of the B^0 ($\overline{B}^0$) mesons decaying to $D^{*+}D^{*-}$. This MC sample has around 110k fully reconstructed signal candidates which is about 120 times the expected signal yield. The second MC dataset is a set of generic $\Upsilon(4S) \to B^0\overline{B}^0$, $\Upsilon(4S) \to B^+B^-$, and $e^+e^- \to q\overline{q}$ decays, where $q = u, d, s, c$. This MC set tries to include all possible sub-decay modes of these processes and has been scaled to match the total integrated luminosity of the data. This generic MC data contains the $B^0 \to D^{*+}D^{*-}$ decay with the branching ratio measured in data and is used to study expected backgrounds.

Decay Mode	Branching Fraction (%)
$D^0 \to K^-\pi^+$	3.82 ± 0.07
$D^0 \to K^-\pi^+\pi^0$	13.5 ± 0.6
$D^0 \to K^-\pi^+\pi^-\pi^+$	7.70 ± 0.25
$D^0 \to K^0_S\pi^+\pi^-$	2.88 ± 0.19
D^0 total	27.9
$D^+ \to K^-\pi^+\pi^+$	9.52 ± 0.34
$D^+ \to K^0_S\pi^+$	1.47 ± 0.06
$D^+ \to K^+K^-\pi^+$	1.00 ± 0.04
D^+ total	11.99

Table 4.1: D meson decay modes and branching fractions used in this analysis.

The analysis of $B^0 \to D^{*+}D^{*-}$ decays relies on fully reconstructed B^0 mesons[1]. D^{*+} mesons are reconstructed in the decays $D^{*+} \to D^0\pi^+$ and $D^{*+} \to D^+\pi^0$. Table 4.1 lists the decay modes and branching fractions [37] of the D mesons. The remainder of this chapter details the reconstruction of signal candidates and the signal yield. An earlier version of this data was used to measure the branching fractions of the $B \to D^{(*)}D^{(*)}$ modes [38], and all of the selection criteria are based on the studies done there.

4.2 Event pre-selection

Events are selected from the `AllEvents` stream in online prompt reconstruction (OPR). Because B events tend to be more isotropic and $c\bar{c}$, $s\bar{s}$, $u\bar{u}$, and $d\bar{d}$ continuum events more jet-like, we pre-select events that have their ratio of the second-to-zeroth Fox-Wolfram moments (R_2) [39] to be less than 0.6. Although the D^{*+} meson decays include $D^{*+} \to D^0\pi^+$ and $D^{*+} \to D^+\pi^0$, we do not include B^0

[1]Unless explicitly stated charge conjugation is implied throughout this dissertation.

candidates with two soft π^0 from the D^* decays.

4.3 Track selection

The charged pion candidates that go into the reconstruction of the $D^{(*)}$ mesons are taken from the *BABAR* list, `GoodTracksVeryLoose`. This list requires that the track have $|d_0| < 1.5\,\text{cm}$ and $|z_0| < 2.5\,\text{cm}$. d_0 is the minimum distance to the beam spot in the $x - y$ plane, and z_0 is the z position of the track at d_0.

Charged kaons are derived from the intersection of the `GoodTracksLoose` list and the `KLHNotPion` list. The `GoodTracksLoose` list has the additional requirements that $p < 10\,\text{GeV}/c$ and that $p_T > 50\,\text{MeV}/c$ on top of the `GoodTracksVeryLoose` requirements. The `KLHNotPion` list only requires that the candidate be inconsistent with the pion hypothesis based on a likelihood formed from energy loss in the trackers and PID data from the DIRC. For the case of $D^0 \to K^-\pi^+$, no PID selection is used and the kaon candidate comes from `GoodTracksLoose`.

4.4 Composite particle reconstructions

4.4.1 π^0 reconstruction

The π^0 candidates are taken from the `pi0AllDefault` list which consists of $\pi^0 \to \gamma\gamma$ candidates reconstructed from EMC clusters. The photons used are required to have a lab energy of 0.030–10.0 GeV and a LAT, defined in Eq. 3.1, of 0.0–0.8. The π^0 candidate is required to have a mass of 115–150 MeV/c^2. The list also includes π^0 candidates where the two γ's were merged into a single EMC

cluster.

4.4.2 K_S^0 reconstruction

The K_S^0 candidates come from the `KsVeryTight` list, which is made up of $K_S^0 \to \pi^+\pi^-$ decays. The pion candidates come from the `ChargedTracks` list, which contains all reconstructed charged tracks and assumes a pion mass hypothesis. These candidates are fit using the `TreeFitter`, a Kalman filter based fitting algorithm [40], which includes a geometric constraint. The mass of the fitted candidate must fall within 15 MeV/c^2 of the nominal K_S^0 mass, have a momentum greater than 200 MeV/c, and must have the χ^2 probability of the fit greater than 0.001.

4.4.3 D meson reconstruction

The composite D meson candidates must have a mass within 20 MeV/c^2 of the nominal mass except in the $D^0 \to K^-\pi^+\pi^0$ decays where a looser $\pm 40\,\mathrm{MeV}/c^2$ cut is applied. Candidates are also required to have a center of mass momentum of 1.2–2.2 GeV/c. Candidates meeting these requirements receive a mass constrained fit before being paired with soft pions to form D^{*+} mesons.

4.4.4 D^* reconstruction

Soft pions used to form the D^{*+} mesons are required to have a CM momentum less than 450 MeV/c. In the case of the π^0 there is also a lower bound of 70 MeV/c. The soft pion candidates and mass constrained D meson candidates are combined

to form D^{*+} candidates. The $\Delta m \equiv m_{D^{*+}} - m_D$ is required to be in the range of 139.6–151.3 MeV/c^2 for the charged soft pions and 135.0–146.3 MeV/c^2 for the neutral. The $(D^0\pi^+)$ candidates are vertex fit with a beam-constraint to improve resolution, but no requirement is made on the quality of the fit.

4.5 B meson reconstruction and selection

B^0 candidates are formed from the combination of two D^* candidates. The B^0 candidate is then refit using the `TreeFitter` updating the daughter particles. This fit is required to converge for the candidate to be considered. Final selection of B^0 candidates is based on cuts on two variables: the mass likelihood and ΔE.

The mass likelihood is formed from a product of the the likelihoods of the D and D^* daughters: a Gaussian for each D and a sum of two Gaussian functions for the Δm.

$$\begin{aligned}\mathcal{L}_{\text{mass}} = & G(m_D; m_{D_{\text{PDG}}}, \sigma_{m_D}) \times G(m_{\bar{D}}; m_{\bar{D}_{\text{PDG}}}, \sigma_{m_{\bar{D}}}) \times \\ & [f_{\text{core}} G(\Delta m_{D^{*+}}; \Delta m_{D^{*+},\text{PDG}}, \sigma_{\Delta m,\text{core}}) \\ & + (1 - f_{\text{core}}) G(\Delta m_{D^{*+}}; \Delta m_{D^{*+},\text{PDG}}, \sigma_{\Delta m,\text{tail}})] \times \\ & [f_{\text{core}} G(\Delta m_{D^{*-}}; \Delta m_{D^{*-},\text{PDG}}, \sigma_{\Delta m,\text{core}}) \\ & + (1 - f_{\text{core}}) G(\Delta m_{D^{*-}}; \Delta m_{D^{*-},\text{PDG}}, \sigma_{\Delta m,\text{tail}})] \ . \end{aligned} \tag{4.1}$$

The different Gaussian functions are centered on the values from the PDG [37]. The width of the Gaussian functions for the D mesons are taken from the error on the D mass from the vertex fit. The widths of the "core" and "tail" Gaussian functions

	$(K\pi)$	$(K\pi\pi^0)$	$(K\pi\pi\pi)$	$(K^0_S\pi\pi)$	$(K^0_S\pi)$	$(K\pi\pi)$	$(KK\pi)$
$(K\pi)$	13.0	12.3	12.7	11.7	0	8.4	0
$(K\pi\pi^0)$		8.4	8.7	8.0	0	5.7	0
$(K\pi\pi\pi)$			8.5	8.2	0	6.6	0
$(K^0_S\pi\pi)$				0	0	0	0

Table 4.2: Cuts on $-\ln(\mathcal{L}_{\rm mass})$ by D decay mode.

of the Δm are taken from signal MC. Distributions of $-\ln(\mathcal{L}_{\rm mass})$ are shown in Fig. 4.1.

ΔE is the difference between the B^0 candidate energy and the beam energy in the center-of-mass frame,

$$\Delta E \equiv E^*_B - E_{\rm beam}\,.$$

A distribution of ΔE in data, shown in Fig. 4.2, clearly shows the signal peak at zero. In this analysis, we cut on ΔE to reduce the background from random combinations of tracks.

The cuts on $-\ln(\mathcal{L}_{\rm mass})$ and ΔE were optimized, per D decay mode, using generic MC to maximize the signal significance of the total signal. The $-\ln(\mathcal{L}_{\rm mass})$ cuts are in Table 4.2, and the $|\Delta E|$ cuts are in Table 4.3. If more than one B^0 candidate is selected per event then the candidate with the best $-\ln(\mathcal{L}_{\rm mass})$ is kept. This has been shown to select the correct B^0 candidate in excess of 95% of the time. For an event to be used in the time-dependent *CP* fit then the tag side vertex must also have converged, $|\Delta t| < 20\,{\rm ps}$ and $\sigma_{\Delta t} < 2.5\,{\rm ps}$. The flavor tagging is described in Sec. 4.6.

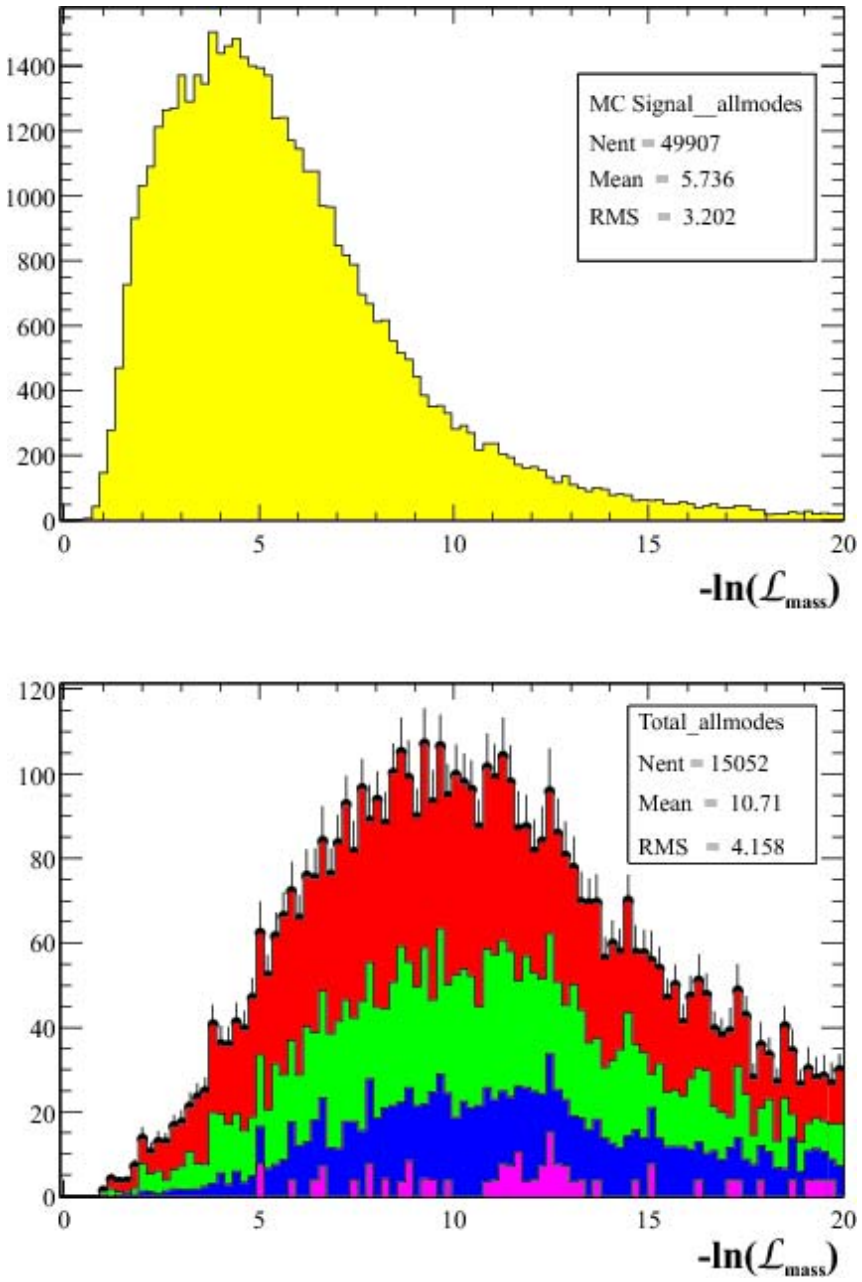

Figure 4.1: The $-\ln(\mathcal{L}_{\rm mass})$ distributions for signal and background. The top plot shows the distribution in pure signal MC. The bottom is background from generic MC scaled to relative luminosity. Red is B^+B^- background; green is $B^0\overline{B}^0$ background; blue is $c\overline{c}$ background; and magenta is $u\overline{u} + d\overline{d} + s\overline{s}$ background.

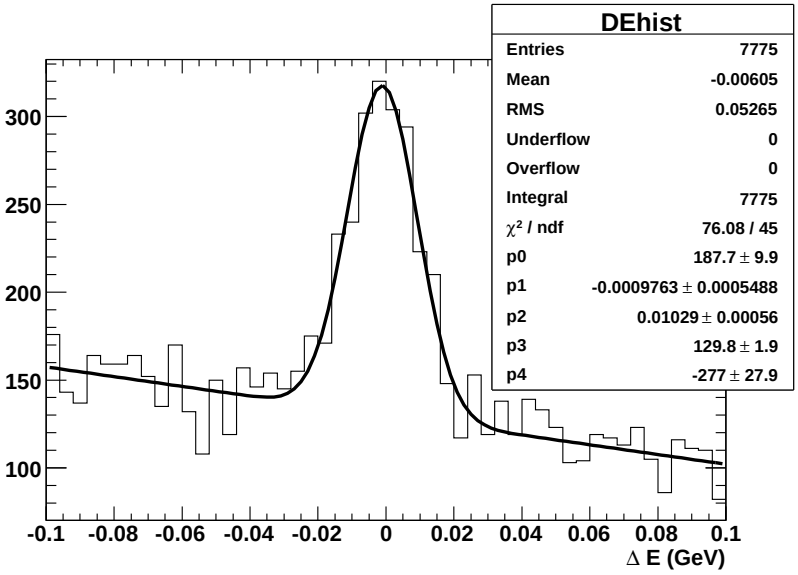

Figure 4.2: Distribution of ΔE in data. This sample is before final event selection and uses cuts $-\ln(\mathcal{L}_{\rm mass}) < 10$ and $m_{\rm ES} > 5.27\,{\rm GeV}/c^2$ to enrich the signal. The curve is a Gaussian plus a line and is only an illustration.

	$(K\pi)$	$(K\pi\pi^0)$	$(K\pi\pi\pi)$	$(K^0_S\pi\pi)$	$(K^0_S\pi)$	$(K\pi\pi)$	$(KK\pi)$
$(K\pi)$	31.6	35.4	34.6	24.9	0	26.1	0
$(K\pi\pi^0)$		27.6	28.0	22.3	0	19.2	0
$(K\pi\pi\pi)$			23.9	21.0	0	19.2	0
$(K^0_S\pi\pi)$				0	0	0	0

Table 4.3: Cuts on $|\Delta E|$ in MeV by D decay mode.

4.6 B flavor tagging

The $\Upsilon(4S)$ decays primarily to a $B^0\overline{B}^0$ or B^+B^- pair. Since the $\Upsilon(4S)$ has $S = 1$ and $J = 1$, the two daughters B are in the anti-symmetric $L = 1$ state. These daughters are also produced coherently and evolve thus until one decays. The remaining B daughter will then evolve according to Eq. 2.17. Fully reconstructing one B provides $t_{\rm rec}$. The other B in the event is used for tagging and provides $t_{\rm tag}$. The majority of B meson decays are flavor-specific, and by analyzing the makeup of the daughter tracks, it is possible to determine the flavor of the B^0 ($\overline{B}^0$) at the time of decay. Using the two decay times, the time-dependent decays rates of Eq. 2.17 become

$$\begin{aligned} f_{B_{\rm tag}=B^0}(\Delta t \equiv t_{\rm rec} - t_{\rm tag}) \propto e^{-\Gamma|\Delta t|} \Bigg\{ 1 + \frac{1-|\lambda|^2}{1+|\lambda|^2}\cos(\Delta m \Delta t) \\ - \frac{2{\rm Im}\lambda}{1+|\lambda|^2}\sin(\Delta m \Delta t) \Bigg\} \\ f_{B_{\rm tag}=\overline{B}^0}(\Delta t \equiv t_{\rm rec} - t_{\rm tag}) \propto e^{-\Gamma|\Delta t|} \Bigg\{ 1 - \frac{1-|\lambda|^2}{1+|\lambda|^2}\cos(\Delta m \Delta t) \\ + \frac{2{\rm Im}\lambda}{1+|\lambda|^2}\sin(\Delta m \Delta t) \Bigg\} \, . \end{aligned} \tag{4.2}$$

where λ was defined in Eq. 2.18. Measurement of Δt and determination of the tag flavor [41] were key in the design of the *BABAR* detector.

Determining Δt is possible because of the asymmetry of the beam energies. This gives the $\Upsilon(4S)$ rest frame a boost of $\beta\gamma = 0.56$ in the lab frame. This increases the average distance between the two B decays in the lab frame from around $30\,\mu$m, with no boost, to about $250\,\mu$m along the boost axis, making an accurate measurement of the spacial separation of the two B decays possible. It is

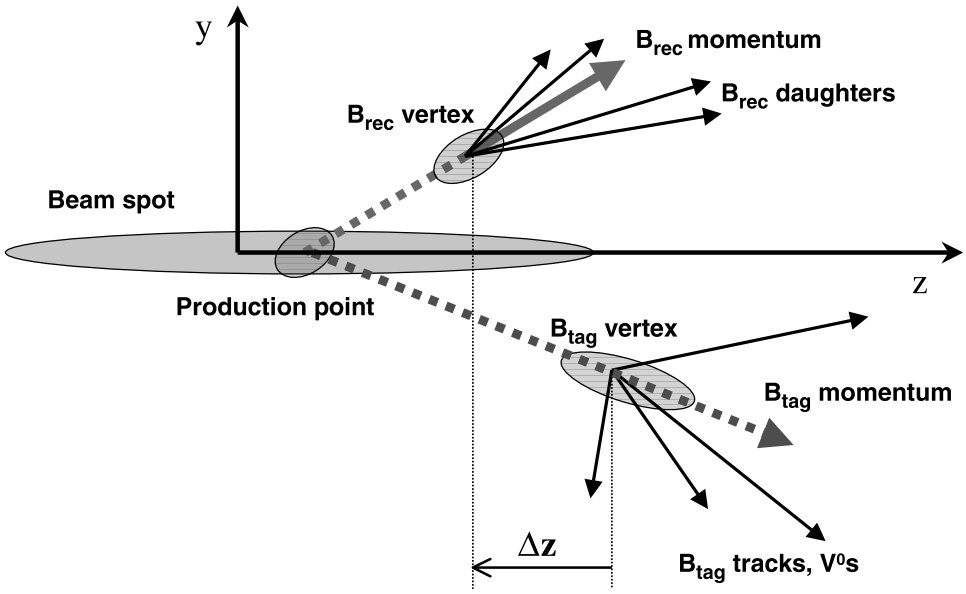

Figure 4.3: Representation of the two time measurement technique for time-dependent *CP* violation.

from this separation that Δt is computed.

$$\Delta z = \beta\gamma\gamma^*_{\rm rec} c\Delta t + \gamma\beta^*_{\rm rec}\cos\theta^*_{\rm rec} c(\tau_{B^0} + |\Delta t|)\,, \tag{4.3}$$

where $\theta^*_{\rm rec}$ is the polar angle, $\beta^*_{\rm rec}$ is the velocity, and $\gamma^*_{\rm rec}$ is the boost factor of the fully reconstructed B^0 candidate in the CM frame. Figure 4.3 depicts the basic technique that goes into measuring Δz. The SVT provides precise measurements of the decay vertexes, which along with the boost is used to compute Δt and its uncertainty $\sigma_{\Delta t}$. The resolution on Δt achieved by this procedure is around 1.1 ps and is dominated by the error on the tagging B vertex. More on the Δt resolution is in Sec. 6.2.

Determining the flavor of the tag B is done based on the information derived from the tracks not used in the fully reconstructed B daughter. The presence of leptons, kaons and/or pions can indicate the flavor of the B. These particles are

produced during the $b \to c \to s$ transitions of the b quark. Pions from D^* decays are also used to aid tagging. The charge of the lepton or kaon distinguishes the B flavor. The decays $B^0 \to D^{*-}\pi^+$ have a hard pion and a soft pion with opposite charge which can be used to determine the flavor because the conjugate decay will swap the charge of the hard and soft pion. Flavor tagging using kaons and pions suffers from pollution from doubly-Cabibbo suppressed decays. The effect is $\mathcal{O}(2\%)$ or less and is treated as a systematic error to the *CP* asymmetry parameters [42].

The *BABAR* flavor tagging is accomplished via several neural networks which look at quantities of the the tracks not used in the reconstructed B to determine the flavor of the tagging B. Tracking and PID quantities are first passed to several neural net sub-taggers, each shown in Fig. 4.4. Each sub-tagger is looking for specific signatures that determine the flavor. For example, there are electron and muon sub-taggers to look for leptons suitable for determining the flavor. The output of the various sub-taggers is turned over to the B Tagger neural net which has a continuous output from $-1(\overline{B}^0)$ to $1(B^0)$, shown in Fig. 4.5. Based on this output the event is assigned to one of six mutually exclusive tagging categories shown in Table 4.4, or if it does not meet any of the criteria, it is considered untagged. The tagging efficiency $\varepsilon_{\rm tag} = (74.33 \pm 0.11)\%$, however due to miss-tagging probabilities, w, the effective tagging performance $Q \equiv \varepsilon_{\rm tag}(1-2w)^2 = 31.2\%$. I discuss determining these quantities and their effects on the time-dependent *CP* measurement in Chapter 6.

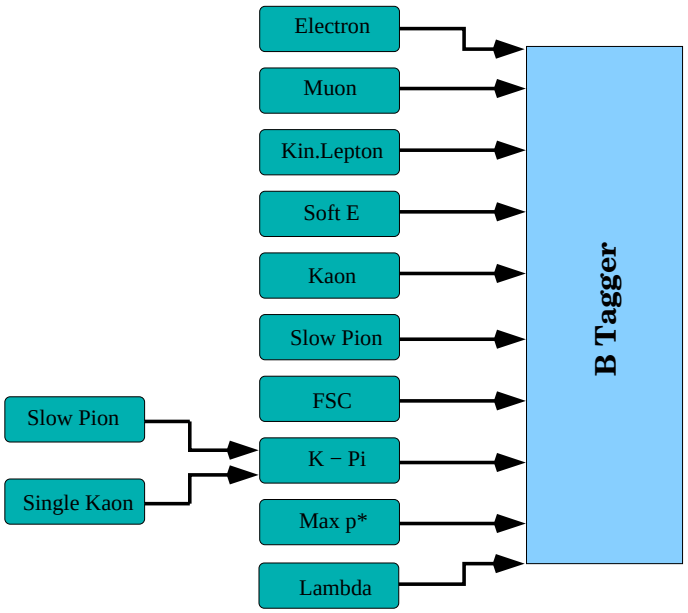

Figure 4.4: Sub-taggers of the *BABAR* flavor tagging routine.

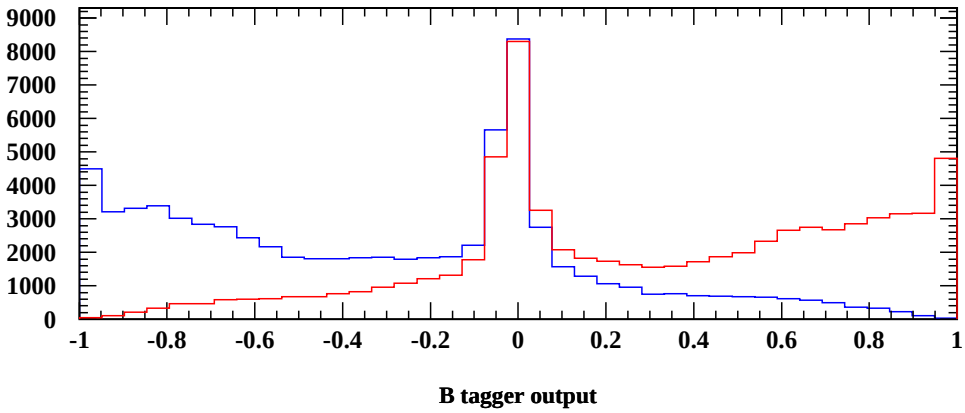

Figure 4.5: Output of the B Tagger neural net, -1 indicates $\overline{B}^0$ and 1 B^0. The blue histogram is true $\overline{B}^0$. The red is true B^0.

Category	Definition
`Lepton`	$\|NN\| > 0.8$ and ($\|$ElectronTag$\| > 0.8$ or $\|$MuonTag$\| > 0.8$)
`Kaon I`	$\|NN\| > 0.8$ and $\|$ElectronTag$\| < 0.8$ and $\|$MuonTag$\| < 0.8$
`Kaon II`	$0.6 < \|NN\| < 0.8$
`Kaon-Pion`	$0.4 < \|NN\| < 0.6$
`Pion`	$0.2 < \|NN\| < 0.4$
`Other`	$0.1 < \|NN\| < 0.2$

Table 4.4: Tagging category definitions based on the output of the B Tagger neural net, NN.

4.7 Signal yields

4.7.1 Yield extraction

To separate the signal from the background, we rely on a fit to the quantity $m_{\rm ES}$ defined as:

$$m_{\rm ES} \equiv \sqrt{(s/2 + p_{\rm beam}p_B)^2/E^2_{\rm beam} - p^2_B}\,. \tag{4.4}$$

The signal distribution is modeled as a Gaussian and the combinatorial background is modeled as and ARGUS threshold function [43],

$$f_{m_{\rm ES,bg}} = m_{\rm ES}\sqrt{1 - 4{m_{\rm ES}}^2/s}e^{\kappa\left(1-4{m_{\rm ES}}^2/s\right)}\,, \tag{4.5}$$

where the κ parameter controls the shape of the distribution. In the yield fit the mean and width of the signal Gaussian, the ARGUS parameter κ, and the signal fraction are allowed to float. Using this technique we fit the data to obtain a preliminary signal yield of 961 events with a purity of 67%. The $m_{\rm ES}$ distribution is shown in Fig. 4.6. This yield is in line with the expected yield given the branching fraction and integrated luminosity. This fit helps to guide further efforts to characterize peaking backgrounds and validate fitting procedures.

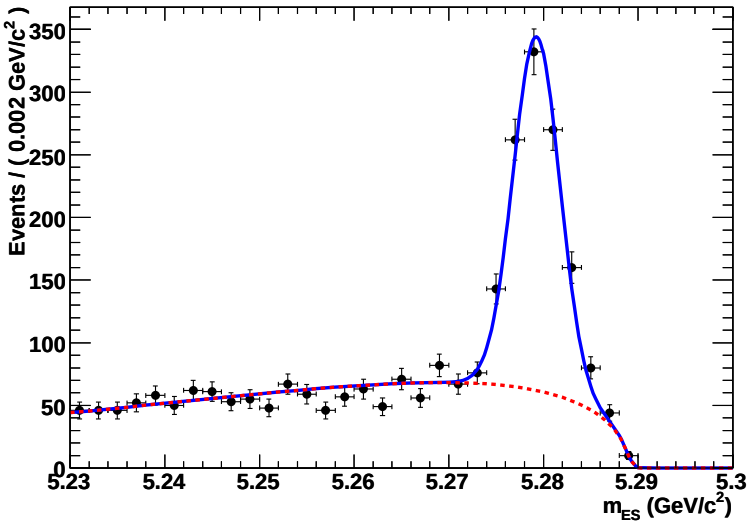

Figure 4.6: Fit to the $m_{\rm ES}$ distribution in data. The blue cure is the signal plus the background, and the red is the background contribution.

4.7.2 Peaking background

Some background sources may tend to peak in the same region as the signal Gaussian. These pose the potential of over-estimating the signal. To evaluate possible peaking background sources, we rely on generic MC data. This MC sample receives full detector simulation and is reconstructed using the same procedure as the data. The MC is reduced via weighting to the integrated luminosity of the data sample. We fit the $m_{\rm ES}$ distribution of this sample the same as the data, shown in Fig. 4.7a. After this initial fit, we remove all of the events that were generated with our signal modes and fix all of the parameters in the fit except the signal fraction. We then fit the remaining sample again, see Fig. 4.7b. From this fit, we find that $(1.6 \pm 1.9)\%$ of the signal peak is background. In subsequent fits we fix the fraction of the peaking background to this value and vary its value as a systematic error.

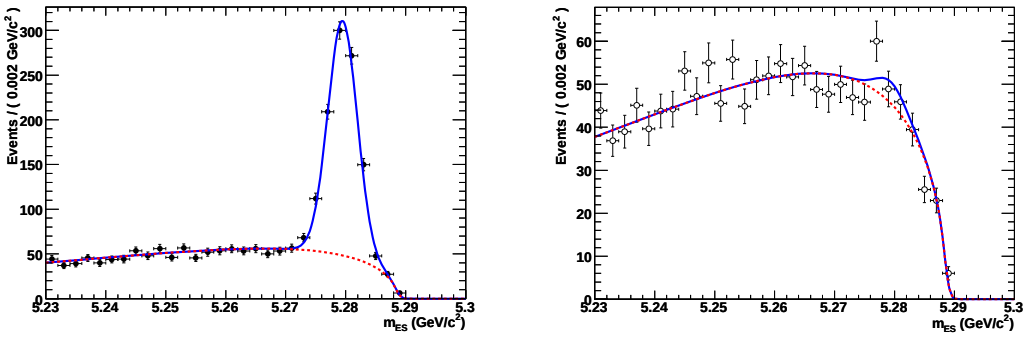

(a) All generic events

(b) Only background events

Figure 4.7: Distributions of $m_{\rm ES}$ taken from generic MC samples weighted to integrated luminosity.

Using our MC, we can further investigate the nature of the peaking background. We find that the principle source of our peaking background is from misreconstructed $B^+ \to D^{*+}\overline{D}^{*0}$ decays, where a slow π^- from the event is combined with the $\overline{D}^0$ from the $\overline{D}^{*0}$ decay to fake a D^{*-} candidate. If we further remove this decay mode from the MC sample, then the peaking fraction drops to 0.2%, confirming that it is the primary contributor. The previous branching fraction measurement [38], which measured both $B^0 \to D^{*+}D^{*-}$ and $B^+ \to D^{*+}\overline{D}^{*0}$, reported a cross feed of 1.8% from $B^+ \to D^{*+}\overline{D}^{*0}$, consistent with our peaking fraction.

Chapter 5

Transversity angle analysis for the *CP*-odd fraction

Section 2.3 discussed the complication in measuring sin2β from $B^0 \to D^{*+}D^{*-}$ decays arising from the different orbital angular momentum partial waves which contribute to the decay. Measuring the size of the *CP*-odd component of the amplitude will allow an undiluted measurement of sin2β. To accurately measure the *CP* content of the decay, we employ a time-integrated angular analysis of D^* daughters. This chapter details the techniques used for this measurement.

5.1 Angular Distribution

Recalling Eq. 2.37 for the full time-dependent angular distribution of $B^0 \to D^{*+}D^{*-}$ decays, integrating the equation over t, $\cos\theta_1$ and $\phi_{\rm tr}$, averaging the B flavor, and accounting for detector efficiency $\varepsilon(\theta_1, \theta_{\rm tr}, \phi_{\rm tr})$ produces

$$\frac{1}{\Gamma}\frac{\mathrm{d}\Gamma}{\mathrm{d}\cos\theta_{\rm tr}} = \frac{3}{4}(1-R_\perp)\sin^2\theta_{\rm tr} \times \left\{ \frac{1+\alpha}{2} I_0(\cos\theta_{\rm tr}) + \frac{1-\alpha}{2} I_\parallel(\cos\theta_{\rm tr}) \right\} + \frac{3}{2} R_\perp \cos^2\theta_{\rm tr} \times I_\perp(\cos\theta_{\rm tr}) \,, \tag{5.1}$$

where $R_\perp$ was defined in Eq. 2.41 and

$$\alpha = \frac{|A_0^0|^2 - |A_\parallel^0|^2}{|A_0^0|^2 + |A_\parallel^0|^2} \,. \tag{5.2}$$

The I_j acceptance functions are

$$I_0 = \frac{3}{2\pi}\int \mathrm{d}\cos\theta_1 \mathrm{d}\phi_{\mathrm{tr}} \varepsilon(\cos\theta_1, \cos\theta_{\mathrm{tr}}, \phi_{\mathrm{tr}}) \cos^2\theta_1 \cos^2\phi_{\mathrm{tr}}$$
$$I_{\parallel} = \frac{3}{4\pi}\int \mathrm{d}\cos\theta_1 \mathrm{d}\phi_{\mathrm{tr}} \varepsilon(\cos\theta_1, \cos\theta_{\mathrm{tr}}, \phi_{\mathrm{tr}}) \sin^2\theta_1 \sin^2\phi_{\mathrm{tr}}$$
$$I_{\perp} = \frac{3}{8\pi}\int \mathrm{d}\cos\theta_1 \mathrm{d}\phi_{\mathrm{tr}} \varepsilon(\cos\theta_1, \cos\theta_{\mathrm{tr}}, \phi_{\mathrm{tr}}) \sin^2\theta_1 \,. \tag{5.3}$$

The *BABAR* detector is unable to efficiently track particles with a transverse momentum less than 55 MeV/c, and this inefficiency leads to a distortion of the angular distributions, which, as seen in Fig. 2.4, are defined using the slow pions. The I_j include the distortions of the angular distributions due to detector inefficiency into our fit. For flat efficiency, i.e. constant I_j, Eq. 5.1 reduces to the very simple form of Eq. 2.40. The determination of the I_j is detailed in Sec. 5.2

Using Eq. 5.1, we can fit the $\cos\theta_{\mathrm{tr}}$ distribution and extract the *CP*-odd fraction $R_{\perp}$. To ensure an unbiased measurement, we model the acceptance moments and detector resolution. Because of small differences seen in the parameters describing the acceptance moments and resolution, these parameters are split into three based on the charges of the slow pions from the D^* mesons, $\pi^+\pi^0$, $\pi^+\pi^-$, and $\pi^0\pi^-$. The following sections describe the procedure for modeling and determining the angular acceptance and detector resolution and provide details of the $R_{\perp}$ measurement.

5.2 Angular acceptance moments

Because the *BABAR* detector does not have uniform efficiency for all $\cos\theta_{\mathrm{tr}}$, it can distort the measured distribution. This inefficiency is very closely correlated to

the ability of the detector to detect and reconstruct the soft pions from D^* decays. Figure 5.1 shows the effect that loosing soft tracks has on the distribution. The effect is very subtle, but can be seen when fitting the generated $\cos\theta_{\rm tr}$ distribution with Eq. 5.1 where the I_j moments are unity. We see that the $R_\perp$ value obtained from the generated $\cos\theta_{\rm tr}$ distribution where a cut on the $p_{\rm T} > 55\,{\rm MeV}/c$, Fig. 5.1b, agrees very well with that of the generated $\cos\theta_{\rm tr}$ distribution where the events have passed the full reconstruction and selection process, Fig. 5.1c. To model the acceptance moments, $I_j(\cos\theta_{\rm tr})$ we use a large sample of fully reconstructed signal MC and the technique of MC integration to evaluate the integrals in Eq. 5.3.

5.2.1 Monte Carlo integration

In general, one can estimate an integral of the form

$$\langle h \rangle = \int h(x) f(x) {\rm d}x \tag{5.4}$$

with data sampled from the normalized PDF $f(x)$ as

$$\langle h \rangle_N \approx \frac{1}{N} \sum_{i=1}^{N} h(x_i)\,, \tag{5.5}$$

where N is the number of points in the data sample. We can apply this on a bin by bin basis to the acceptance moments

$$I_j(z) = \int {\rm d}x{\rm d}y\, g_j(x,y)\varepsilon(x,y,z)\,,$$

where $g_0 = 3/2\pi y^2\cos^2 x$, $g_\parallel = 3/4\pi(1-y^2)\sin^2 x$, $g_\perp = 3/8\pi(1-y^2)$, $x = \phi_{\rm tr}$, $y = \cos\theta_1$, and $z = \cos\theta_{\rm tr}$. Thus, in bin k

$$I_j^k = \frac{n_{\rm bins}}{2N_{\rm gen}} \sum_i^{N_k} \frac{g_j(x_i,y_i)}{f_{\rm gen}(x_i,y_i,z_i)}\,, \tag{5.6}$$

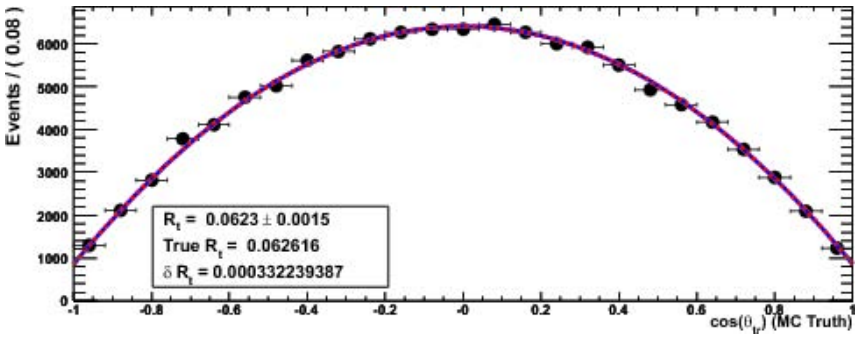

(a) Generated $\cos\theta_{\mathrm{tr}}$ distribution

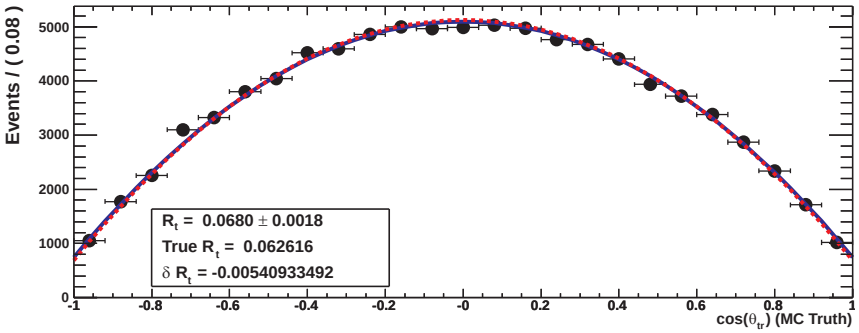

(b) Generated $\cos\theta_{\mathrm{tr}}$ distribution with slow pion $p_{\mathrm{T}} > 55\,\mathrm{MeV}/c$

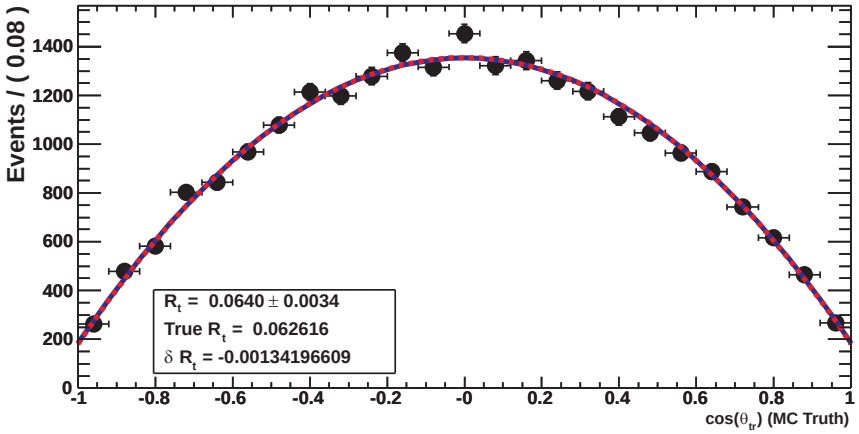

(c) Generated $\cos\theta_{\mathrm{tr}}$ distribution of events satisfying all reconstruction and selection criteria

Figure 5.1: Generated $\cos\theta_{\mathrm{tr}}$ distributions showing the effects of detector acceptance.

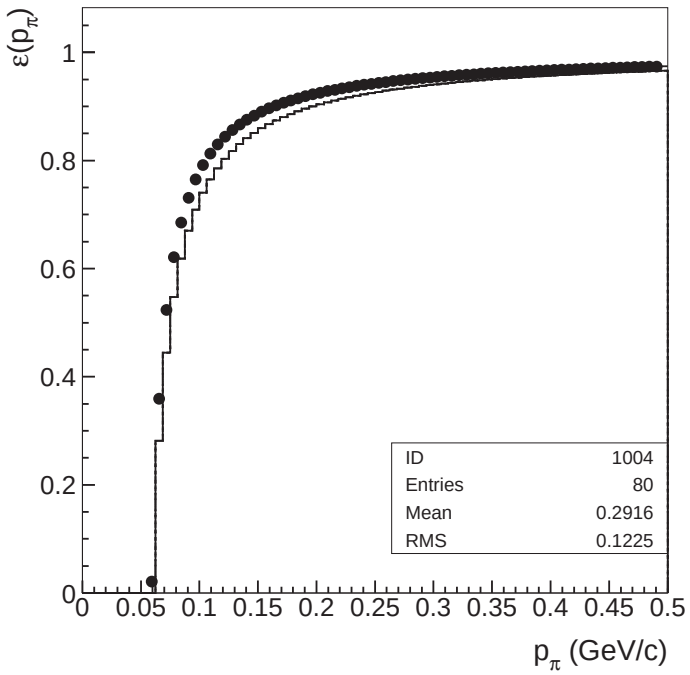

Figure 5.2: Slow pion efficiency as a function of momentum for data (points) and MC (histogram).

where $f_{\rm gen}$ is the full angular distribution in Eq. 2.44, $N_{\rm gen}$ is the total number of events generated, and N_k is the number of events reconstructed in bin k. The factor $2/n_{\rm bins}$ is the width of the bin for $n_{\rm bins}$ equal bins. The uncertainty for each bin is expressed as

$$\sigma_j^k = \left(\frac{n_{\rm bins}}{2N_{\rm gen}}\right)\sqrt{\sum_i^{N_k}\left(\frac{g_j(x_i,y_i)}{f_{\rm gen}(x_i,y_i,z_i)}\right)^2 - \frac{1}{N_{\rm gen}}\left(\sum_i^{N_k}\frac{g_j(x_i,y_i)}{f_{\rm gen}(x_i,y_i,z_i)}\right)^2}. \qquad (5.7)$$

5.2.2 Parameterization of acceptance moments

We apply the MC integration technique to our sample of signal MC generated with amplitudes $(A_\parallel, A_0, A_\perp) = (0.62, 0.74, 0.24)$. This MC sample was reconstructed identically to the data with the additional requirement that the B^0 be reconstructed with the same D modes that it was generated and that $m_{\rm ES} > 5.27\,{\rm GeV}/c^2$.

	$\pi^+\pi^-$ mode	$\pi^+\pi^0$ mode	$\pi^0\pi^+$ mode
I_0	$e_0 = 0.098 \pm 0.0007$	$e_0 = 0.046 \pm 0.0006$	$e_0 = 0.046 \pm 0.0006$
	$e_2 = 0.007 \pm 0.002$	$e_2 = 0.003 \pm 0.002$	$e_2 = 0.0007 \pm 0.002$
$I_\parallel$	$e_0 = 0.103 \pm 0.0009$	$e_0 = 0.047 \pm 0.0008$	$e_0 = 0.048 \pm 0.0007$
	$e_2 = 0.002 \pm 0.002$	$e_2 = 0.002 \pm 0.002$	$e_2 = 0.002 \pm 0.002$
$I_\perp$	$e_0 = 0.102 \pm 0.001$	$e_0 = 0.045 \pm 0.0008$	$e_0 = 0.045 \pm 0.0008$
	$e_2 = 0.005 \pm 0.002$	$e_2 = 0.005 \pm 0.002$	$e_2 = 0.006 \pm 0.002$

Table 5.1: Parameters of the acceptance moments for each of the three slow pion modes.

We additionally apply corrections to the MC based on differences in slow pion efficiency between data and MC. The efficiencies, shown in Fig. 5.2, as a function of momentum p can be parameterized separately for data and MC using

$$\epsilon(p) = \begin{cases} \epsilon_{max}\left(1 - \frac{1}{\beta(p-p_0)+1}\right) & \text{if } p > p_0 \\ 0 & \text{if } p \leq p_0 \end{cases}, \tag{5.8}$$

where $p_0 = 59\,\mathrm{MeV}/c$ is the cutoff, $\beta_{\mathrm{MC}} = 60$ and $\beta_{\mathrm{data}} = 78.6$. We use these parameterizations to correct the MC to better match the data.

We parameterize the acceptance moments as second-order even polynomials of $\cos\theta_{\mathrm{tr}}$,

$$I_j(\cos\theta_{\mathrm{tr}}) = e_{0,j} + e_{2,j}\cos^2\theta_{\mathrm{tr}}\,. \tag{5.9}$$

From Fig. 2.4, there is no reason to expect odd contributions to the efficiency moments, and when a $\cos\theta_{\mathrm{tr}}$ term is included it is consistent with zero. We also tried adding a fourth order term to the fit and found that this too was consistent with zero. These parameters are determined for each of the three slow pion modes using binned distributions of 40 bins. The results of the fit are shown in Fig. 5.3 and the parameter values are in Table 5.1.

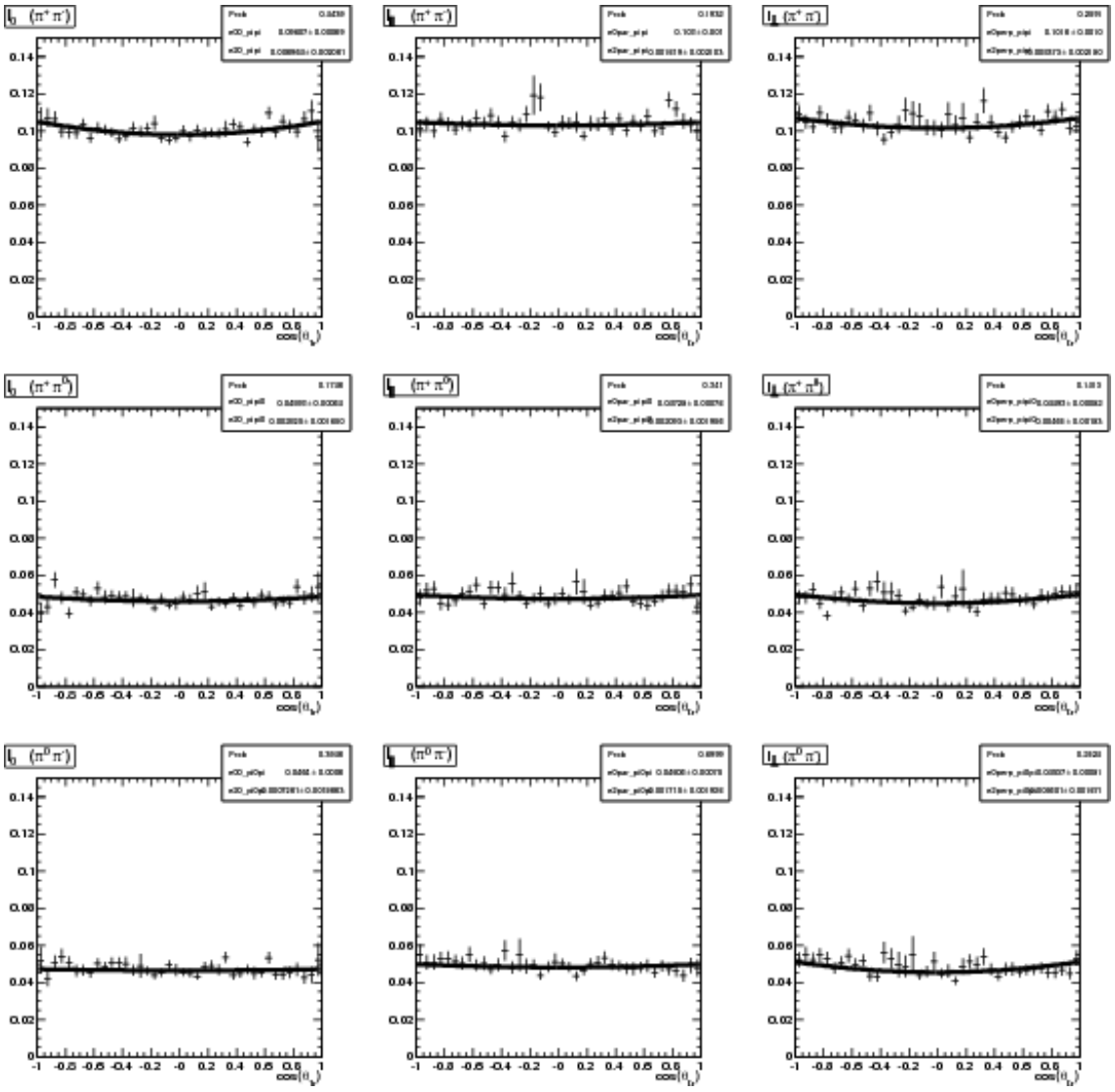

Figure 5.3: Acceptance moment distributions for the three moments (I_0, $I_\parallel$, $I_\perp$). The first line is for $\pi^+\pi^-$, the second $\pi^+\pi^0$, and the third $\pi^0\pi^-$.

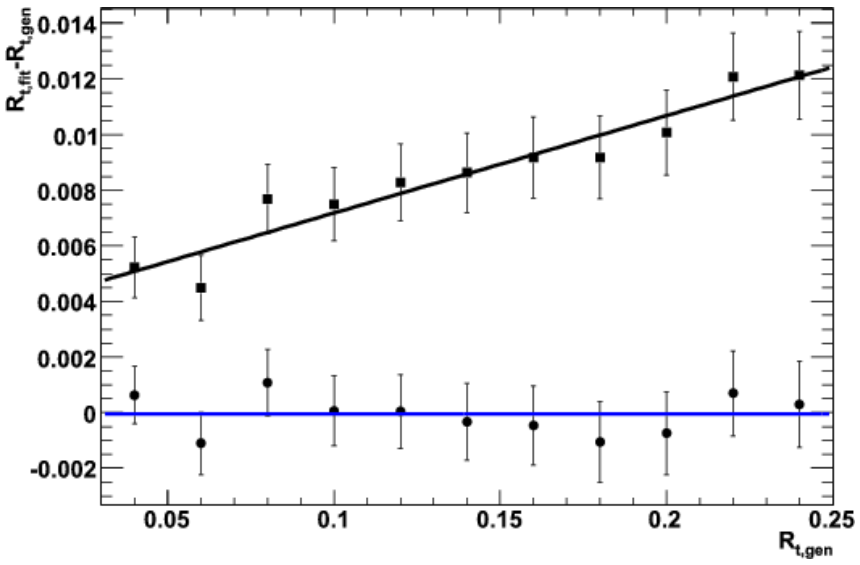

Figure 5.4: Deviation from generated $R_\perp$ for high statistics toy MC fits. Each point represents a single 200k event fit. The black line and square points are from fits where acceptance was neglected. The circular points are from fits which include acceptance. The blue line is zero.

5.2.3 Acceptance moment validation

To understand the effect of the acceptance on the measurement of $R_\perp$, we perform large-statistics toy MC experiments where we generate signal distributions according to Eq. 5.1, where the acceptance is modeled. We then fit these experiments with a PDF which ignores the acceptance and with a PDF which includes it. The difference from the generated $R_\perp$ is shown in Fig. 5.4, where a clear bias is visible in the points that neglect acceptance. It should be noted that because the acceptance moments are all similarly flat, the bias from neglecting the acceptance is smaller than that from the angular resolution which will be discussed in Sec. 5.3.

Additionally, we fit the true generated $\cos\theta_{\rm tr}$ distribution of the full signal MC data sample. When neglecting the detector acceptance, we find $R_\perp = 0.0676 \pm 0.0015$, larger than the generated $R_\perp = 0.0626$ and consistent with the toy MC

study. After including the acceptance, we find $R_\perp = 0.0614 \pm 0.0015$, consistent with the input $R_\perp$.

5.3 Angular resolution model

The finite measurement resolution of the detector smears the measured distribution of the angle $\theta_{\rm tr}$. We fold this in by convolving the angular distribution in Eq. 5.1 with a resolution model $\mathcal{R}(\theta_{\rm tr} - \theta'_{\rm tr})$, where $\theta'_{\rm tr}$ is the true generated $\theta_{\rm tr}$. This presents a problem because Eq 5.1 is a function of $z = \cos\theta_{\rm tr}$ defined on $[-1, 1]$ while the resolution is most naturally function is a function of $\theta_{\rm tr}$.

Given the probability $\mathcal{R}(\theta_{\rm tr} - \theta'_{\rm tr})$ of measuring $\theta_{\rm tr}$ given a true value of $\theta'_{\rm tr}$,

$$\begin{aligned} g(z; z') &= \sum \left| \frac{\mathrm{d}\theta_{\rm tr}}{\mathrm{d}z} \right| \mathcal{R}(\theta_{\rm tr} - \theta'_{\rm tr}) \\ &= \sum \left| \frac{1}{\sqrt{1 - z^2}} \right| \mathcal{R}(\theta_{\rm tr} - \theta'_{\rm tr}) \,, \end{aligned} \tag{5.10}$$

where the sum is over all of the $\theta'_{\rm tr}$ values that map onto the same z', namely $\theta'_{\rm tr} = \pm\cos^{-1} z' + 2\pi n$ and n is an integer. Convolving the physics PDF $P(z')$ with $\mathcal{R}$ yields

$$\begin{aligned} \tilde{P}(z) &= \int_{-1}^{1} P(z') g(z; z') \mathrm{d}z' \\ &= \frac{1}{\sqrt{1 - z^2}} \sum_n \int_{-1}^{1} \mathrm{d}z' P(z') \left[\mathcal{R}(\cos^{-1} z - (\cos^{-1} z' + 2\pi n) \right. \\ &\qquad \left. + \mathcal{R}((\cos^{-1} z - (-\cos^{-1} z' + 2\pi n) \right] \,. \end{aligned} \tag{5.11}$$

After changing variables, the relation simplifies to

$$\tilde{P}(z) = \frac{1}{\sqrt{1 - z^2}} \sum_n (-1)^n \int_{n\pi}^{(n+1)\pi} \mathrm{d}\theta'_{\rm tr} \sin\theta'_{\rm tr} P(\cos\theta'_{\rm tr}) \mathcal{R}(\theta_{\rm tr} - \theta'_{\rm tr}) \,. \tag{5.12}$$

We use Gaussian functions to model our resolution. These all have widths much narrower than π meaning that we can approximate the sum by keeping only the $n = -1, 0, 1$ terms.

5.3.1 Uncorrelated soft pions

There is a fraction of signal events where the true D meson is paired with a random soft pion from the event to for the D^* meson. These events satisfy the selection criteria, and must be accounted for in the fit. To estimate their magnitude we model the distribution as a truncated Gaussian centered at $\theta_{\rm tr} = \pi/2$,

$$P_{\rm misReco}(\theta_{\rm tr}) = \frac{1}{\sqrt{2\pi}\sigma_{\rm mis}} \frac{1}{\mathrm{erf}(\frac{\pi}{2\sqrt{2}\sigma_{\rm mis}})} e^{-\frac{(\theta_{\rm tr}-\pi/2)^2}{2\sigma^2_{\rm mis}}}, \tag{5.13}$$

normalized on the domain $[0, \pi]$. Changing variables to z yields

$$P_{\rm misReco}(z) = \frac{1}{\sqrt{1-z^2}} \frac{1}{\sqrt{2\pi}\sigma_{\rm mis}} \frac{1}{\mathrm{erf}(\frac{\pi}{2\sqrt{2}\sigma_{\rm mis}})} e^{-\frac{(\cos^{-1} z-\pi/2)^2}{2\sigma^2_{\rm mis}}}. \tag{5.14}$$

We include Eq. 5.13 in the fit to constrain the resolution and Eq. 5.14 as a component of the angular fit to extract $R_\perp$.

5.3.2 Parameterization of the angular resolution

We model the resolution function as the sum of three Gaussian functions, a narrow core Gaussian, an intermediate wide Gaussian, and a tail Gaussian. We also include Eq. 5.13 to model the portion coming from the mis-reconstructed slow pions

	$\pi^+\pi^0$	$\pi^+\pi^-$	$\pi^0\pi^-$
σ_{core}	0.033 ± 0.002	0.0231 ± 0.0003	0.054 ± 0.003
f_{core}	0.257 ± 0.026	0.423 ± 0.008	0.388 ± 0.043
σ_{wide}	0.092 ± 0.004	0.071 ± 0.001	0.125 ± 0.009
σ_{tail}	0.235 ± 0.011	0.224 ± 0.004	0.257 ± 0.026
f_{tail}	0.253 ± 0.022	0.171 ± 0.005	0.144 ± 0.013
σ_{mis}	0.622 ± 0.009	0.582 ± 0.009	0.645 ± 0.009
f_{mis}	0.169 ± 0.004	0.031 ± 0.001	0.163 ± 0.005

Table 5.2: Parameters of the resolution model extracted from signal MC.

for a total distribution:

$$\begin{aligned}\mathcal{R}(\theta_{\text{tr}} - \theta'_{\text{tr}}) = (1 - f_{\text{mis}}) \times [f_{\text{core}} G(\theta_{\text{tr}} - \theta'_{\text{tr}}; 0, \sigma_{\text{core}}) + f_{\text{tail}} G(\theta_{\text{tr}} - \theta'_{\text{tr}}; 0, \sigma_{\text{tail}}) \\ + (1 - f_{\text{core}} - f_{\text{tail}}) G(\theta_{\text{tr}} - \theta'_{\text{tr}}; 0, \sigma_{\text{wide}})] + f_{\text{mis}} P_{\text{misReco}}(\theta_{\text{tr}}; \pi/2, \sigma_{\text{mis}})\end{aligned} \tag{5.15}$$

Again the parameters are split into three based on the slow pion mode. We extract the resolution parameters in a fit to the signal MC. The extracted parameter values are in Table 5.2. To evaluate the effectiveness of the fit, we project the fit result onto θ_{tr} in eight bins of θ'_{tr}. The projections for each of the slow pion modes are shown in Figs. 5.5–5.7.

5.3.3 Angular resolution validation

To understand possible bias originating from neglecting angular resolution, we generated several toy MC experiments of 300k events using the full model of the detector acceptance and resolution. We then fit these toy events using the PDF convolved with the resolution function and one which ignores angular resolution. The results of this study can be seen in Fig. 5.8. The square points and black

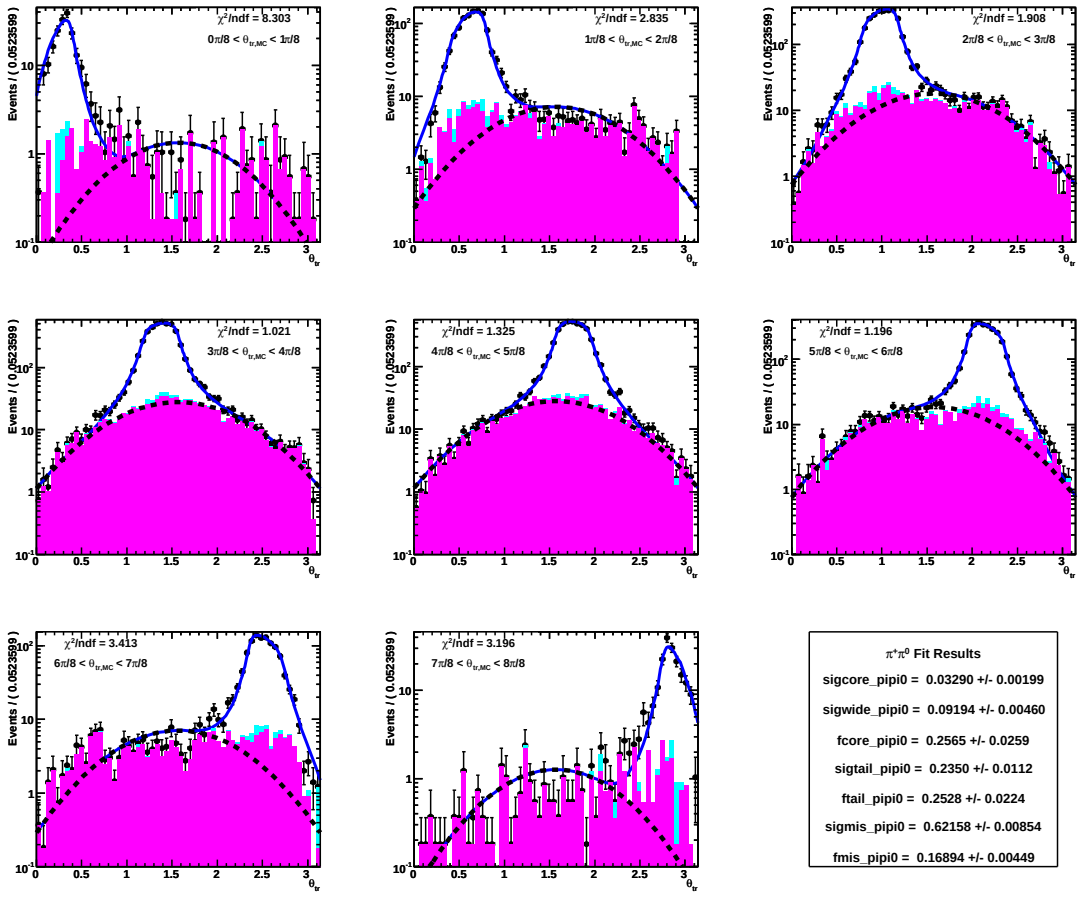

Figure 5.5: Projections of the $\pi^+\pi^0$ resolution function in bins of $\theta'_{\rm tr}$. The magenta histogram are events where the slow pion actually came from the other B. The cyan histogram is where the slow pion came from the signal B but was not the true slow pion. The dashed line is the contribution from $P_{\rm misReco}$

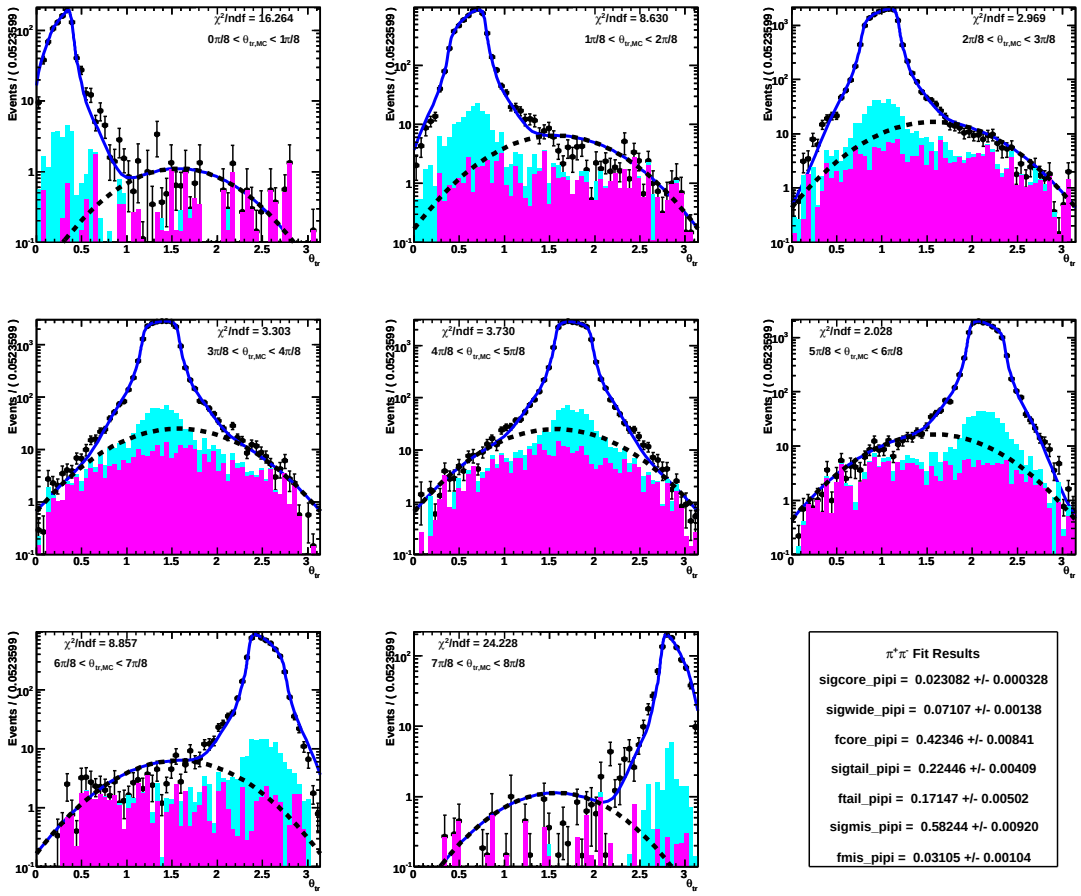

Figure 5.6: Projections of the $\pi^+\pi^-$ resolution function in bins of $\theta'_{\rm tr}$. The magenta histogram are events where the slow pion actually came from the other B. The cyan histogram is where the slow pion came from the signal B but was not the true slow pion. The dashed line is the contribution from $P_{\rm misReco}$

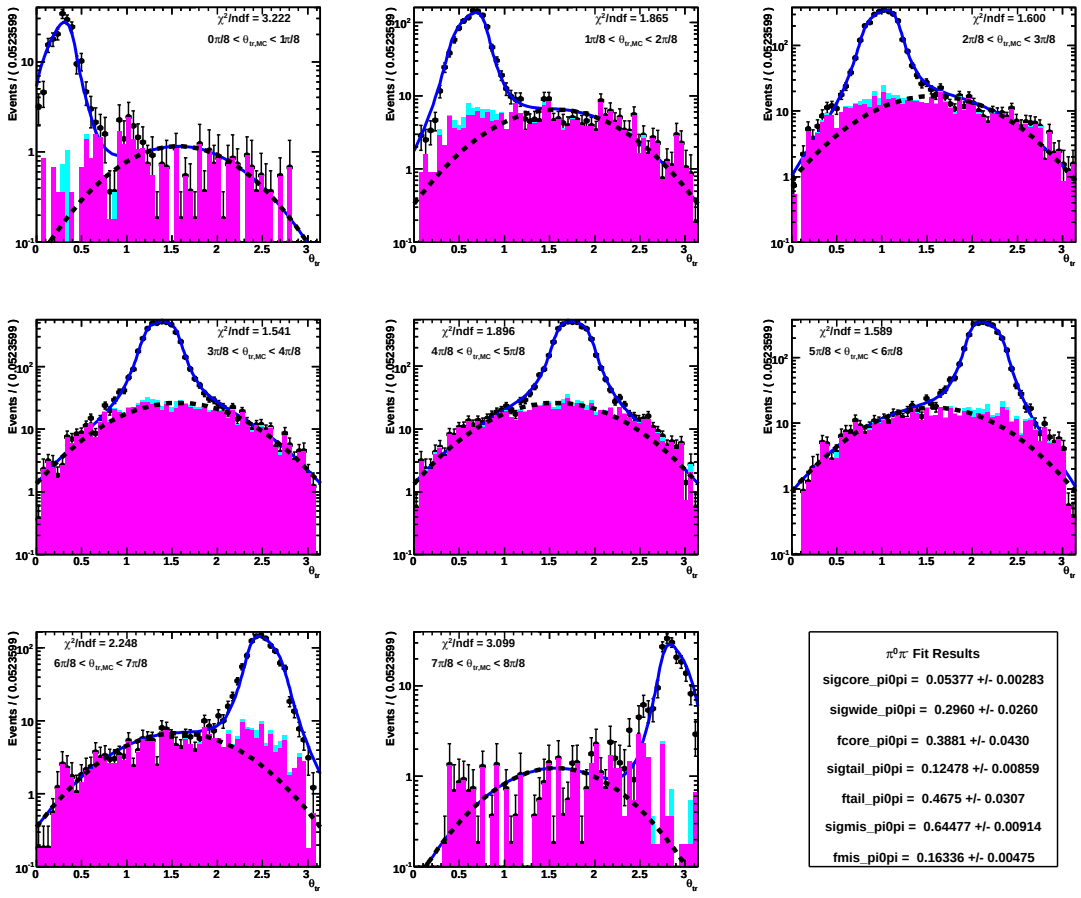

Figure 5.7: Projections of the $\pi^0\pi^-$ resolution function in bins of $\theta'_{\rm tr}$. The magenta histogram are events where the slow pion actually came from the other B. The cyan histogram is where the slow pion came from the signal B but was not the true slow pion. The dashed line is the contribution from $P_{\rm misReco}$

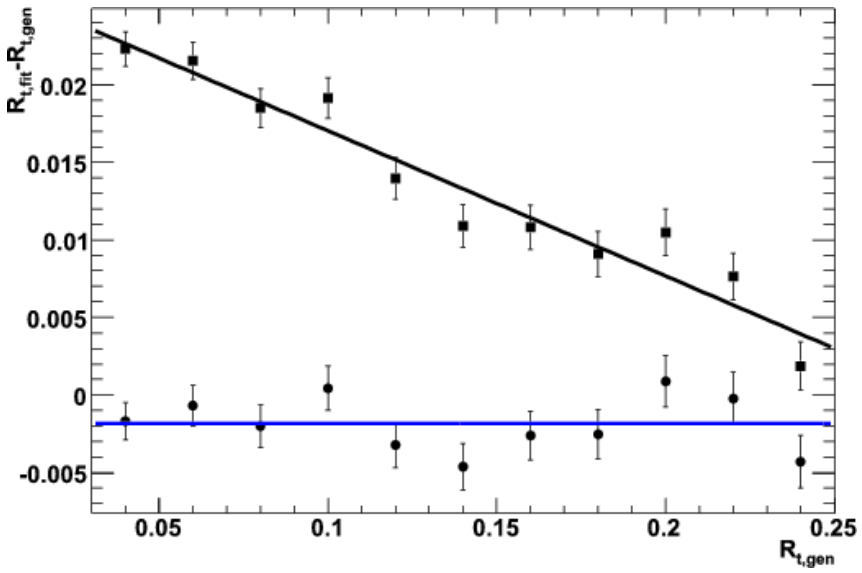

Figure 5.8: Toy MC study where each point is a 300k event experiment generated using the full detector resolution model. The square points and black line are from fits using a model that neglects detector resolution. The circular points and blue line are from a model that includes detector resolution.

line show a clear bias. This bias is also much larger than the one observed when neglecting the acceptance. From the circular points and blue line, we see that including the resolution in the fit removes the bias.

In addition, we fit our sample of signal MC assuming ideal resolution. We find $R_\perp = 0.0841 \pm 0.0015$ which is significantly larger than the generated $R_\perp = 0.0626$ and consistent with the expectation from Fig. 5.8. When we convolve our resolution model with the signal PDF in Eq. 5.1 and include the component for the misreconstructed pions Eq. 5.14, we find $R_\perp = 0.0614 \pm 0.0017$.

5.4 Angular fit description and validation

The fit to extract the *CP*-odd fraction $R_\perp$ is an unbinned maximum likelihood fit to the $m_{\rm ES}$ and $\cos\theta_{\rm tr}$ distributions for each of the three slow pion modes

simultaneously. The likelihood is then defined as

$$\mathcal{L} = \prod_i \mathcal{L}_i = e^{-(N_{\rm sig}-N_{\rm bg})} \prod_i [N_{\rm sig} \times \mathcal{F}_{\rm sig}(m_{{\rm ES},i}) \times \mathcal{F}_{\rm sig}(\cos\theta_{{\rm tr},i}) + N_{\rm bg} \times \mathcal{F}_{\rm bg}(m_{{\rm ES},i}) \times \mathcal{F}_{\rm bg}(\cos\theta_{{\rm tr},i}) + (N_{\rm sig} f_{\rm peak}) \times \mathcal{F}_{\rm sig}(m_{{\rm ES},i}) \times \mathcal{F}_{\rm sig}(\cos\theta_{{\rm tr},i})] \ . \quad (5.16)$$

We define the components of the fit as follows: $\mathcal{F}_{\rm sig}(m_{\rm ES})$ is a Gaussian function whose mean and width are free, $\mathcal{F}_{\rm sig}(\cos\theta_{\rm tr})$ is the PDF in Eq. 5.1 convolved with the resolution model in Eq 5.15 with the parameters of the acceptance and resolution fixed to those extracted from signal MC, $\mathcal{F}_{\rm bg}(m_{\rm ES})$ is the ARGUS function in Eq. 4.5 with a shape parameter κ that floats, and $\mathcal{F}_{\rm bg}(\cos\theta_{\rm tr}) = 1+b_2\cos^2\theta_{\rm tr}$ with b_2 allowed to vary. Additionally the signal and background yields ($N_{\rm sig}$ and $N_{\rm bg}$) of each of the three slow pion modes float in the fit. The parameter $f_{\rm peak}$ was extracted in Sec. 4.7.2 and is fixed. Because the peaking background shape is the same as that of signal, it is indistinguishable from signal. The peaking background need not be the same shape as the signal, and to evaluate the effect of this assumption, the shape and relative contribution are varied as a source of systematic error. In the nominal fit, the α parameter in Eq. 5.1 is fixed to zero.

5.4.1 Toy MC validation

We validate the likelihood fitter using toy MC generated using the PDF described above and with values $R_\perp = 0.14$ and $\alpha = 0$. The free parameters are generated with values expected from preliminary fits to data. We generate 200 data-sized experiments and fit each. The distribution of the $R_\perp$, its error and pull,

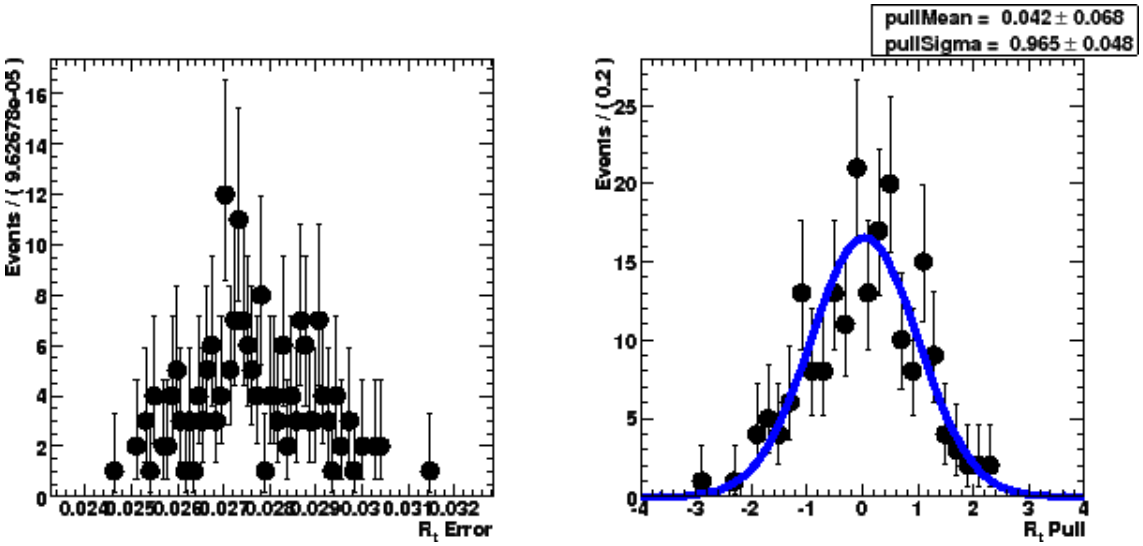

Figure 5.9: Plots showing the distributions from 200 toy MC experiments. The left is $R_\perp$; the center is its error; and the right is the pull overlaid with a Gaussian fit.

$(R_{\perp,\text{fit}} - R_{\perp,\text{gen}})/\sigma_{R_\perp}$, are shown in Fig. 5.9. The pull distribution has a mean consistent with zero and a width consistent with one indicating no bias and reasonable errors from the fit.

We also scan $R_\perp$ to ensure that the fitter is stable over the expected range of the parameter using 100k event toy MC experiments. The deviations from the generated values are shown in Fig. 5.10. Significant deviation is not observed.

5.4.2 Full MC validation

Because the fitter is unbiased when tested using toy MC, we next test the fitter using our two samples of MC generated using full detector simulation. The signal MC sample was generated with $R_\perp = 0.0626$ and $\alpha = 0.179$. The result of the fit is $R_\perp = 0.0614 \pm 0.0017$, and the projections are shown in Fig. 5.11. The second sample is our sample of generic MC which has been weighted to the luminosity. This sample

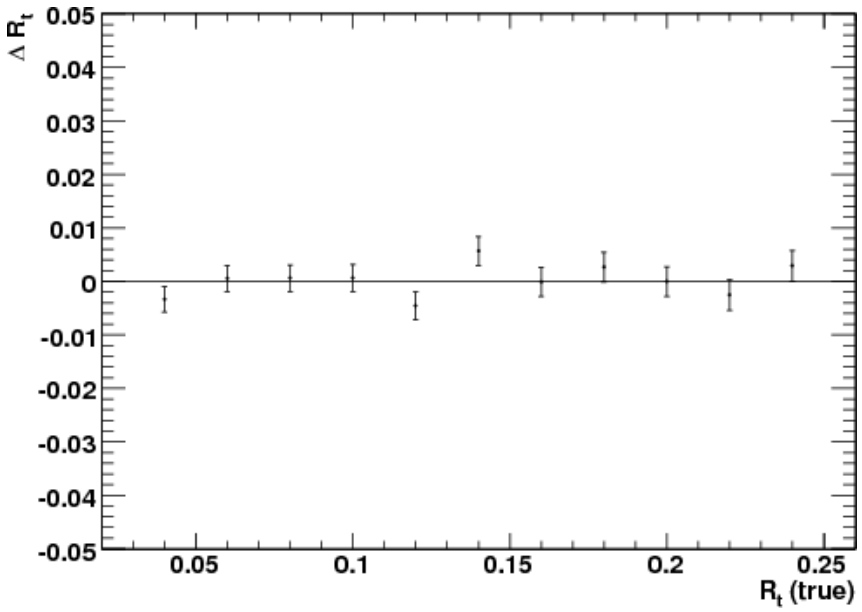

Figure 5.10: Deviations from the generated value of $R_\perp$ for toy MC experiments with 100k events over the expected range of $R_\perp$.

was generated with amplitudes $(A_0, A_\parallel, A_\perp) = (0.96, 0.56, 0.47)$ corresponding to $R_\perp = 0.222$. The fit resulted in $R_\perp = 0.207 \pm 0.031$ and the projections are in Fig. 5.12. In both of these validations, we do not find any significant bias.

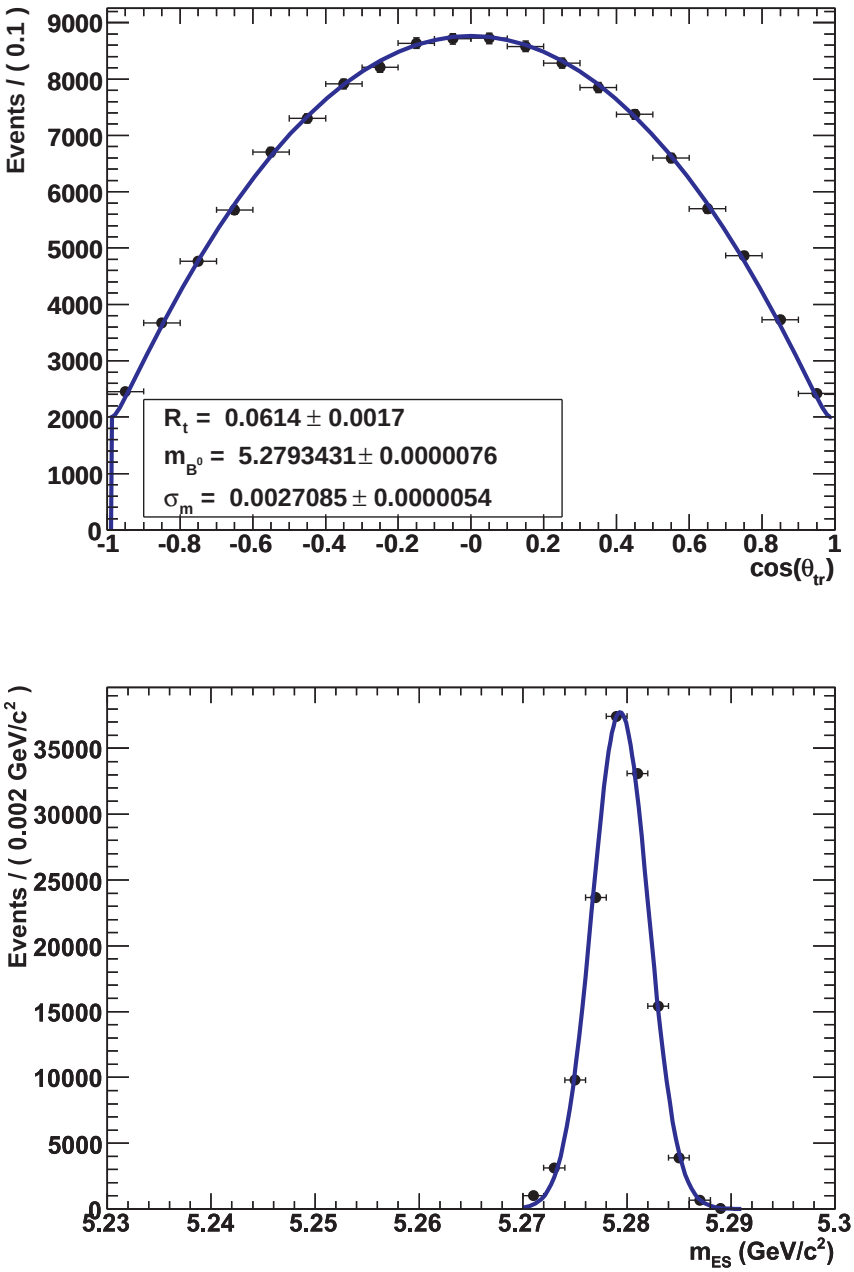

Figure 5.11: Projection of the signal MC fit result unto $\cos\theta_{\rm tr}$ (top) and $m_{\rm ES}$ (bottom).

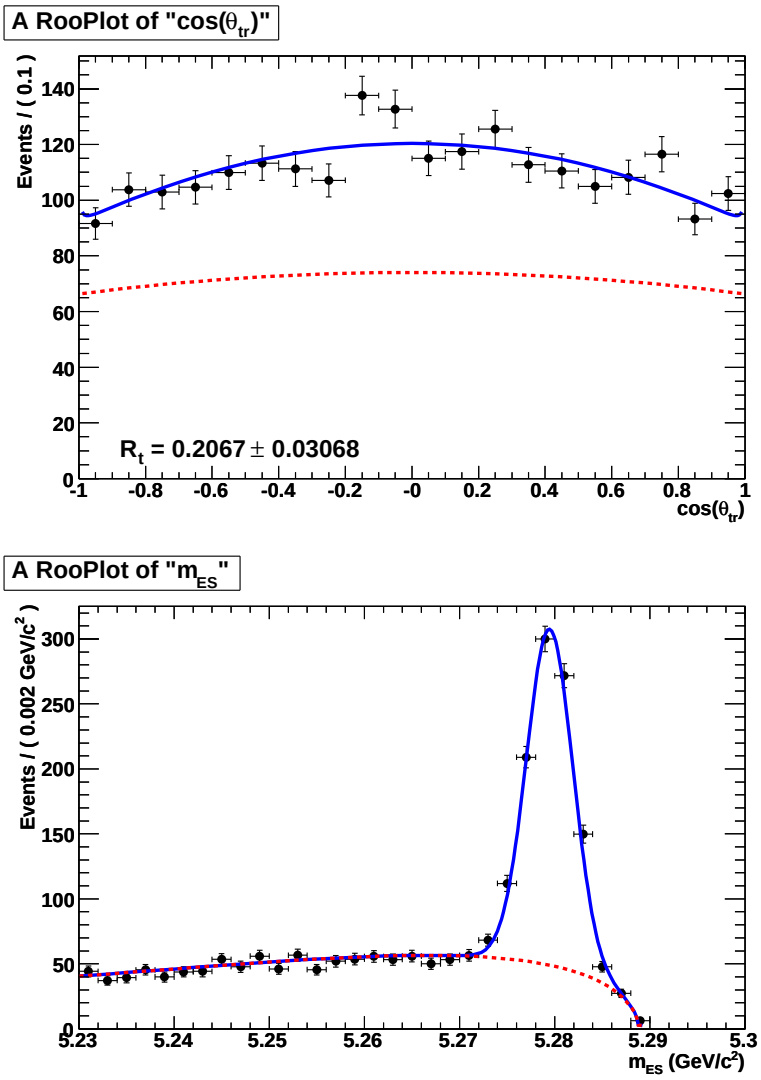

Figure 5.12: Projection of the generic MC fit result onto $\cos\theta_{\rm tr}$ (top) and $m_{\rm ES}$ (bottom). The dashed red line represents the contribution from the background.

Systematics source	$\delta R_\perp$
Angular Resolution Parameters	0.0006
Angular Resolution Uncorrelated	0.0036
Acceptance Moments Parameters	0.0024
α parameter scan	0.0026
Peaking background	0.0014
Background model	0.0002
Potential fit bias	0.0017
TOTAL	0.0055

Table 5.3: Systematic uncertainties of $R_\perp$.

5.5 Angular fit systematic errors

Using a random offset, we blind the value of $R_\perp$ to evaluate the systematic uncertainties. The blind value from the nominal fit is $R_\perp = 0.353 \pm 0.028$. A summary of the systematic uncertainties is in Table 5.3.

5.5.1 Angular resolution model

In the nominal fit, we fix the parameters of the resolution model to those in Table 5.2 extracted from signal MC. To evaluate our sensitivity to these values, we generate 100 random parameter sets based on the error matrix from the nominal parameters. We refit the data using these parameter sets and look at the distribution of the deviation of $R_\perp$. We fit these distributions with a Gaussian function and assign the width plus the magnitude of the mean as the error. The errors for the three slow pion modes are added in quadrature to ascertain the total systematic error. The distributions are shown in Fig. 5.13. The total systematic is 0.00058.

We parameterize the mis-reconstructed signal as a truncated Gaussian func-

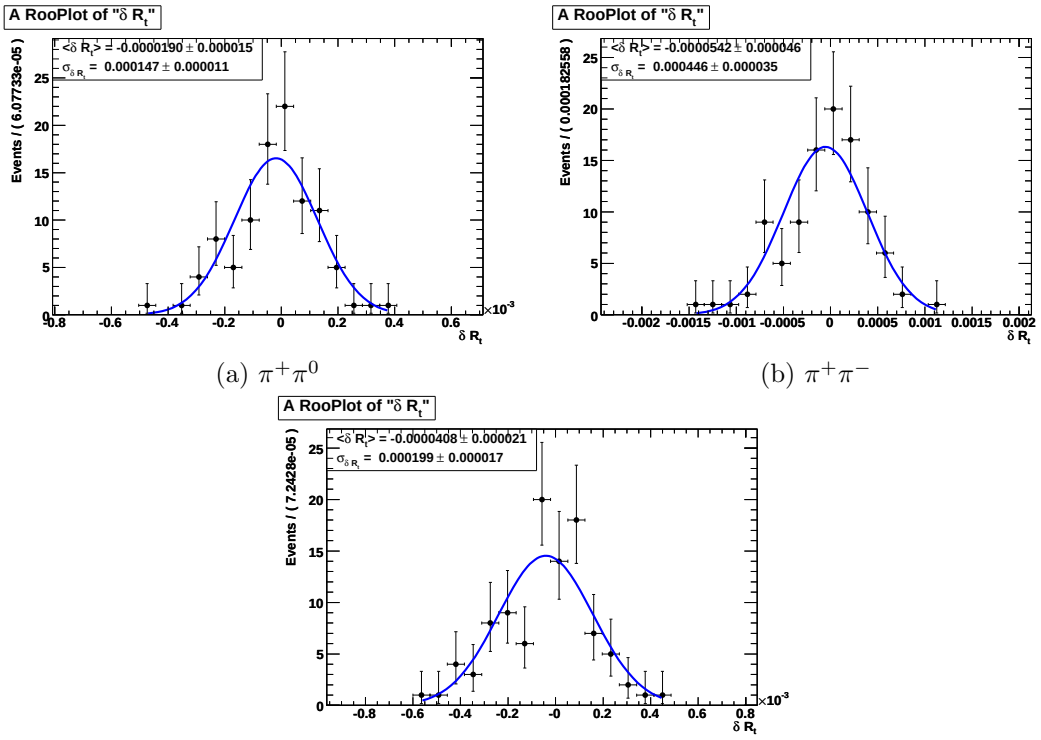

(a) $\pi^+\pi^0$ (b) $\pi^+\pi^-$

(c) $\pi^0\pi^-$

Figure 5.13: Distribution of $\delta R_\perp$ from fits using randomized resolution parameters.

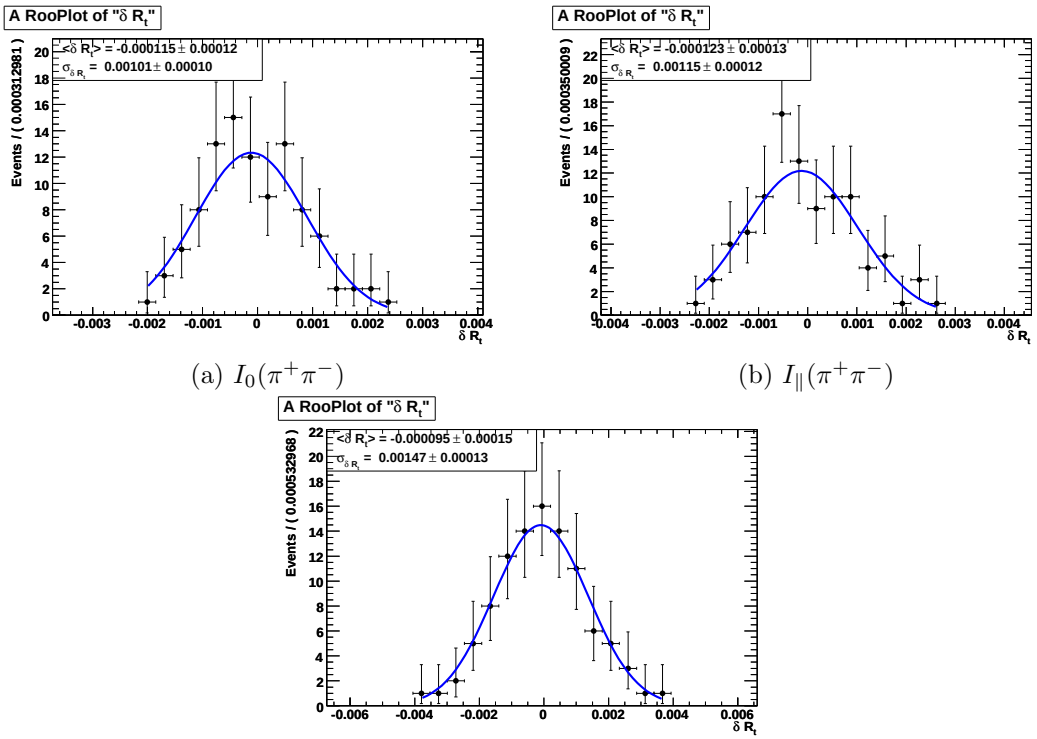

(a) $I_0(\pi^+\pi^-)$ (b) $I_{\|}(\pi^+\pi^-)$

(c) $I_{\perp}(\pi^+\pi^-)$

Figure 5.14: Distribution of $\delta R_{\perp}$ from fits using randomized acceptance moment parameters for the $\pi^+\pi^-$ acceptance moments

tion centered at $\pi/2$. As a conservative estimate of its effect, we drop the misreconstructed portion and refit the data. The deviation with respect to the nominal fit configuration yields a systematic uncertainty of 0.0036.

5.5.2 Angular acceptance parameters

The parameters used in the detector acceptance moments are also fixed in the nominal fit. We evaluate the systematic associated with this similarly to that from the resolution parameters. The distributions of $\delta R_{\perp}$ are in Figs. 5.14–5.16. The quadratic sum of the nine uncertainties is 0.0024.

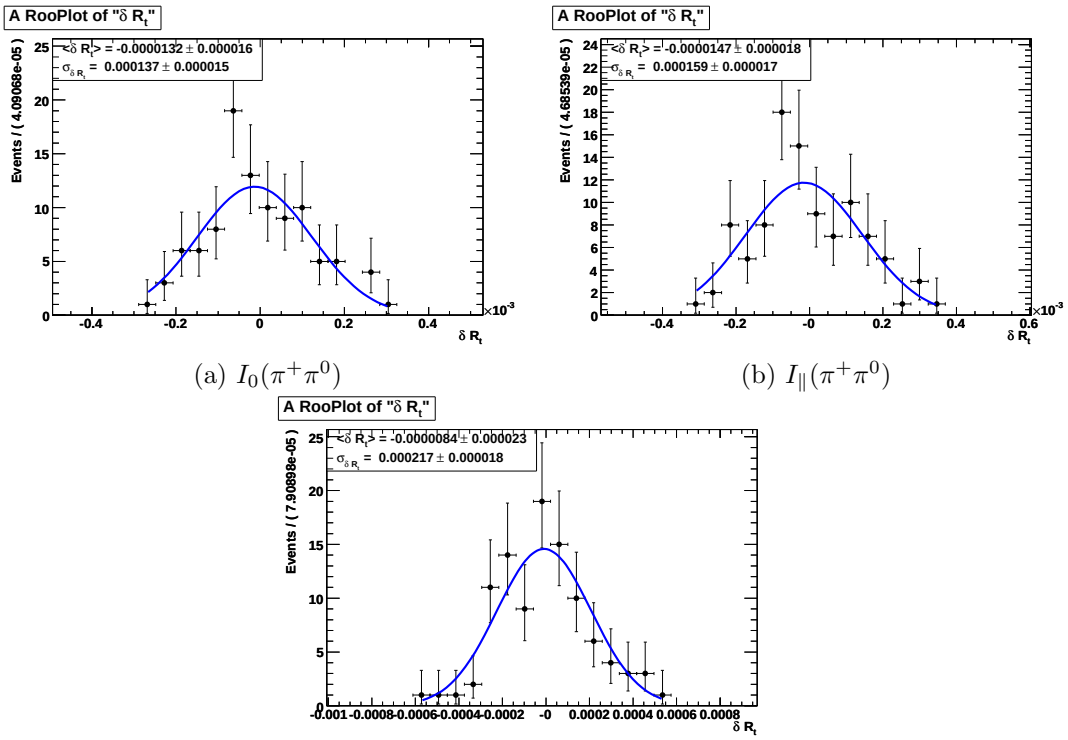

(a) $I_0(\pi^+\pi^0)$

(b) $I_\parallel(\pi^+\pi^0)$

(c) $I_\perp(\pi^+\pi^0)$

Figure 5.15: Distribution of $\delta R_\perp$ from fits using randomized acceptance moment parameters for the $\pi^+\pi^0$ acceptance moments.

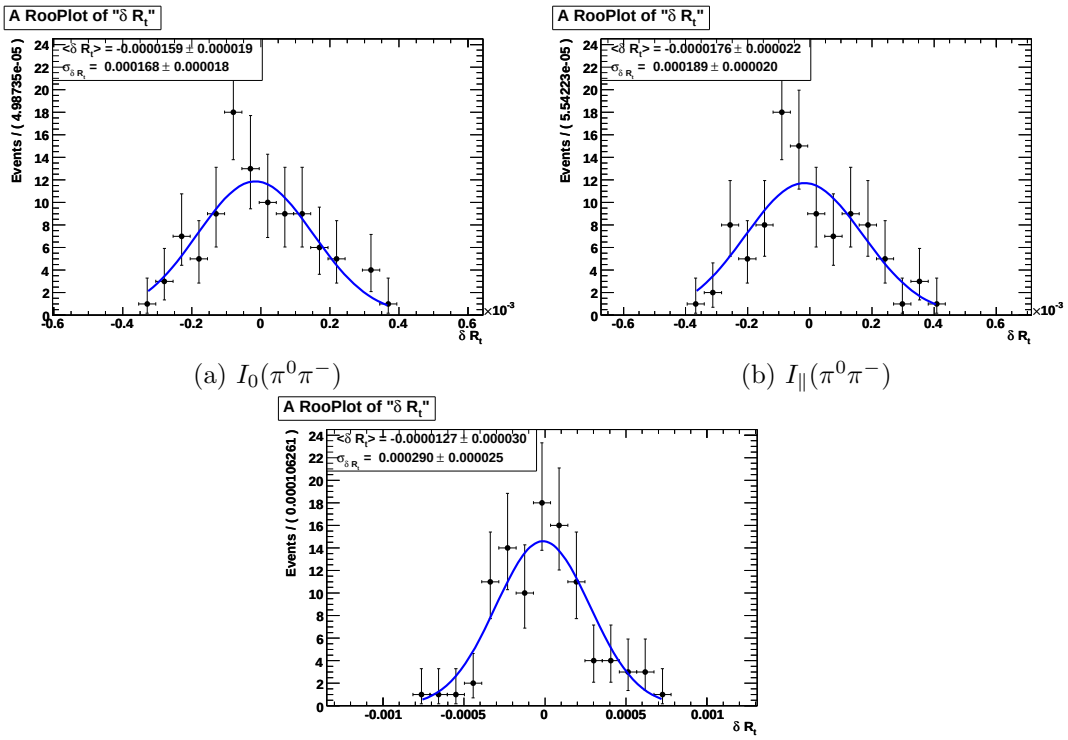

(a) $I_0(\pi^0\pi^-)$

(b) $I_{\parallel}(\pi^0\pi^-)$

(c) $I_{\perp}(\pi^0\pi^-)$

Figure 5.16: Distribution of $\delta R_{\perp}$ from fits using randomized acceptance moment parameters for the $\pi^0\pi^-$ acceptance moments.

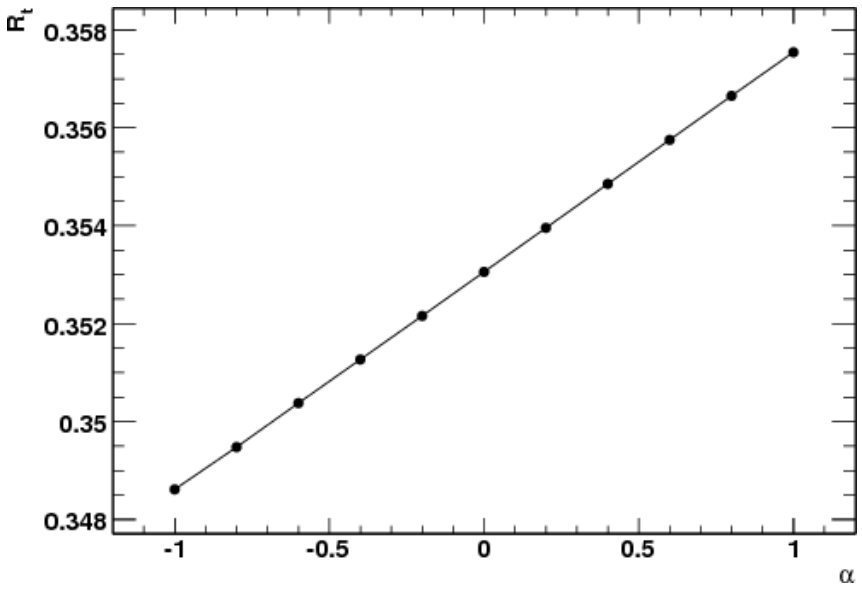

Figure 5.17: Blind values of $R_\perp$ as a function of α. The statistical error bars have been suppressed for clarity.

5.5.3 Parameter α

The parameter α, the asymmetry between the *CP*-even amplitudes, is fixed to zero in the nominal fit. We scan α from -1 to 1 to see what the dependence of $R_\perp$ is on α, Fig. 5.17. As a systematic we take the difference in the values of $R_\perp$ at $\alpha = \pm 1$ divided by $\sqrt{12}$. This yields 0.0026.

5.5.4 Peaking background

In the nominal fit peaking background is essentially ignored. To estimate the uncertainty due to this assumption we change the peaking background $\cos\theta_{\rm tr}$ PDF to be that of the background instead of that of the signal. The fraction $f_{\rm peak}$ is kept fixed at 1.6%. The difference with respect to the nominal fit 0.0014 is the systematic error. We also varied the width of the peaking background $m_{\rm ES}$ component $\times 1.5$

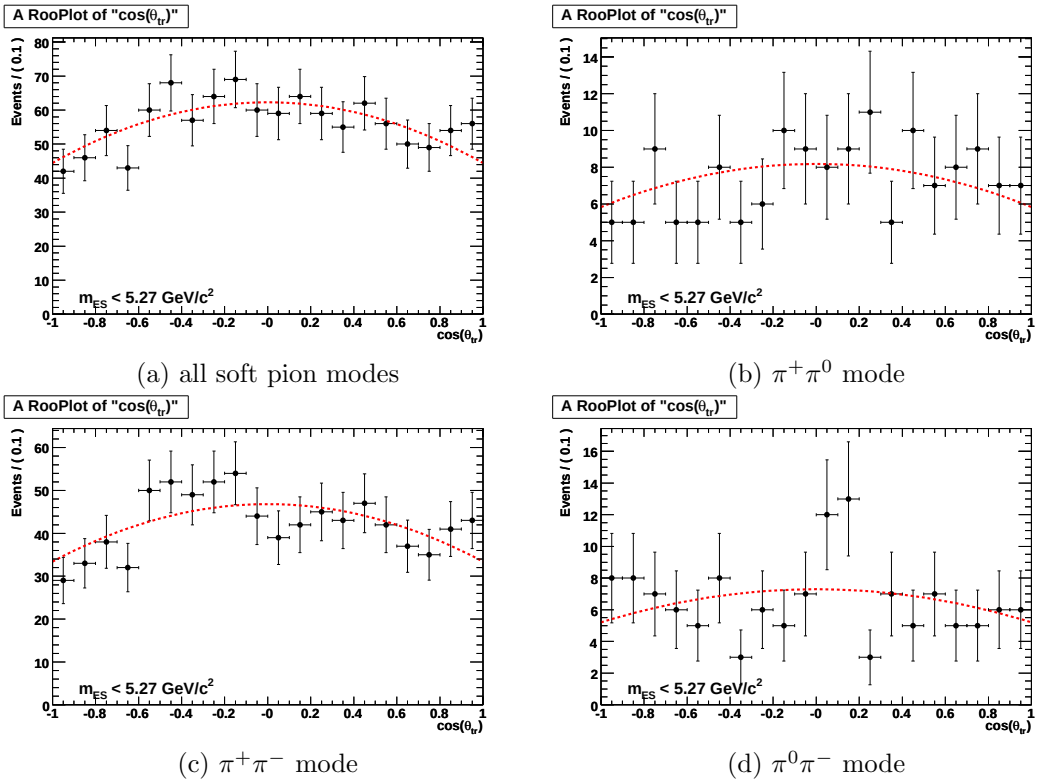

(a) all soft pion modes

(b) $\pi^+\pi^0$ mode

(c) $\pi^+\pi^-$ mode

(d) $\pi^0\pi^-$ mode

Figure 5.18: Distribution of $\cos\theta_{\rm tr}$ data for the sideband $m_{\rm ES} < 5.27\,{\rm GeV}/c^2$. The red dashed line is the background contribution from the fit.

and found that this is negligible.

5.5.5 Background Model

The $\cos\theta_{\rm tr}$ background model is a second-order even polynomial. This is constrained by the $m_{\rm ES}$ sidebands in the fit, Fig. 5.18. We change the parameterization to include a fourth-order term and allow the corresponding b_4 parameter to vary in the fit. We find that b_4 is consistent with zero and the difference in $R_\perp$, 0.00018, is assigned as a systematic.

Shape parameters		Signal yields		Background Yields	
κ	-61.1 ± 6.2	$N_{\mathrm{sig},\pi^+\pi^-}$	766 ± 39	$N_{\mathrm{bg},\pi^+\pi^-}$	1205 ± 45
b_2	-0.287 ± 0.073	$N_{\mathrm{sig},\pi^+\pi^0}$	89 ± 13	$N_{\mathrm{bg},\pi^+\pi^0}$	233 ± 17
m_{B^0}	5.27927 ± 0.00012	$N_{\mathrm{sig},\pi^0\pi^-}$	100 ± 12	$N_{\mathrm{bg},\pi^0\pi^-}$	186 ± 15
σ_{B^0}	0.00270 ± 0.00012				

Table 5.4: Values of floating parameters in the fit to data to extract $R_\perp$.

5.5.6 Potential fit bias

Our MC validation of the likelihood fit is limited by the statistical power of our MC samples. We see no significant biases and as a systematic error we assign the error on $R_\perp$ from the signal MC, 0.0017, as the associated systematic error.

5.6 Results

After evaluating the systematic uncertainty on $R_\perp$, we reveal the blinded value from the fit and find

$$R_\perp = 0.158 \pm 0.028(\mathrm{stat}) \pm 0.006(\mathrm{syst})\,. \tag{5.17}$$

The projection of the fit onto the data is in Fig. 5.19. Values for the other floating parameters in the fit are given in Table 5.4.

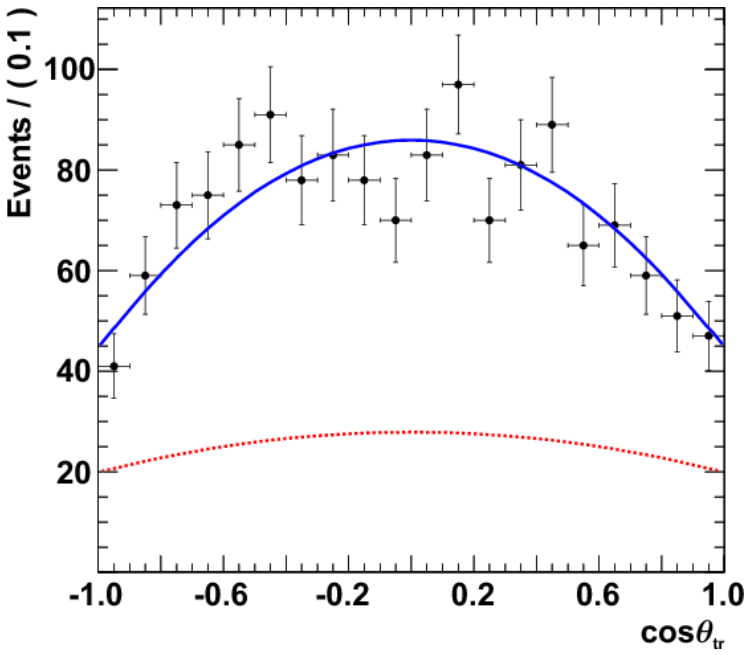

Figure 5.19: The fit result projected onto $\cos\theta_{\rm tr}$ for data where $m_{\rm ES} > 5.27\,{\rm GeV}/c^2$. The solid blue line is the total PDF, and the dashed red line is the background contribution.

Chapter 6

Time-dependent *CP* analysis

From Eqs. 2.37 and 2.42, we can derive a time-dependent decay rate similar to Eq. 2.17,

$$\begin{aligned}\frac{1}{\Gamma}\frac{\mathrm{d}^2\Gamma(\overset{(-)}{B^0}\to D^{*+}D^{*-})}{\mathrm{d}z\mathrm{d}t} = \frac{9}{32\pi}e^{-\Gamma t}\{&[(1-R_\perp)G_+(z)+R_\perp G_-(z)]\\ &\overset{(-)}{+}[C_+(1-R_\perp)G_+(z)+C_\perp R_\perp G_-(z)]\cos\Delta m_d t\\ &\overset{(+)}{-}[S_+(1-R_\perp)G_+(z)-S_\perp R_\perp G_-(z)]\sin\Delta m_d t\}\ ,\end{aligned} \tag{6.1}$$

where

$$\begin{aligned}G_+(z) &= \frac{8\pi}{3}(1-z^2) = \frac{8\pi}{3}\sin^2\theta_{\mathrm{tr}}\\ G_-(z) &= \frac{16\pi}{3}z^2 = \frac{16\pi}{3}\cos^2\theta_{\mathrm{tr}}\,.\end{aligned} \tag{6.2}$$

The *CP* asymmetry parameters S_+ and C_+ are defined as

$$\begin{aligned}S_+ &= \frac{S_\parallel|A_\parallel^0|^2+S_0|A_0^0|^2}{|A_\parallel^0|^2+|A_0^0|^2}\\ C_+ &= \frac{C_\parallel|A_\parallel^0|^2+C_0|A_0^0|^2}{|A_\parallel^0|^2+|A_0^0|^2}\,.\end{aligned} \tag{6.3}$$

Because of the possible differences in the relative penguin and tree amplitudes, there are three distinct S and C parameters as discussed in Sec. 2.3. When taking into

account empirical tagging performance, Eq. 6.1 becomes

$$
\begin{aligned}
f_{\pm}(z,\Delta t) = \frac{9}{32\pi} e^{-|\Delta t|/\tau_{B^0}} \{ & (1 \mp \Delta w)\left[(1-R_{\perp})G_{+}(z) + R_{\perp}G_{-}(z)\right] \\
& \mp (1-2w)\left[C_{+}(1-R_{\perp})G_{+}(z) + C_{\perp}R_{\perp}G_{-}(z)\right]\cos\Delta m_d \Delta t \\
& \pm (1-2w)\left[S_{+}(1-R_{\perp})G_{+}(z) - S_{\perp}R_{\perp}G_{-}(z)\right]\sin\Delta m_d \Delta t \} \ , \qquad (6.4)
\end{aligned}
$$

with average mis-tag rate w and mis-tag differences Δw between B^0 and $\overline{B}^0$.

6.1 B tagging performance

B tagging was described in Sec. 4.6. The performance of the tagging routine is evaluated using a data sample of fully reconstructed B^0 decays to flavor eigenstates $B_{\rm flav}$ [41]. These are B^0 decays to $D^{(*)-}(\pi^+, \rho^+, a_1^+)$ states. Applying the tagging routine to these decays provides a method to understand the performance of the tagging routine and to measure the mis-tag rates and differences which dilute the *CP* parameters in Eq. 6.4. The mis-tag quantities are split based on the tagging category. Table 6.1 contains the tagging performance extracted from the $B_{\rm flav}$ sample. These quantities are fixed in the *CP* fit.

6.2 Δt resolution function

Finite detector resolution of the B vertices translates into a smearing of the distribution in Eq. 6.4. To unfold this from the measurement, we convolve Eq. 6.4 with a resolution model composed of the sum of three Gaussian functions, a core, a tail and an outlier. The bias and width of the core and tail Gaussian functions are

Category	ε	$\Delta\varepsilon$	w	Δw	Q
`Lepton`	8.96 ± 0.07	-0.1 ± 0.2	2.8 ± 0.3	0.3 ± 0.5	7.98 ± 0.11
`Kaon I`	10.82 ± 0.07	0.0 ± 0.2	5.3 ± 0.3	-0.1 ± 0.6	8.65 ± 0.14
`Kaon II`	17.19 ± 0.09	0.2 ± 0.3	14.5 ± 0.3	0.4 ± 0.6	8.68 ± 0.17
`Kaon-Pion`	13.67 ± 0.08	0.0 ± 0.2	23.3 ± 0.4	-0.7 ± 0.7	3.91 ± 0.12
`Pion`	14.18 ± 0.08	-0.7 ± 0.3	32.5 ± 0.4	5.1 ± 0.7	1.73 ± 0.09
`Other`	9.54 ± 0.07	0.3 ± 0.2	41.5 ± 0.5	3.8 ± 0.8	0.27 ± 0.04
Total	74.37 ± 0.10	-0.2 ± 0.6			31.2 ± 0.3

Table 6.1: Tagging efficiency parameters found from fitting the B_{flav} data sample. Tagging efficiency ε, efficiency difference between B^0 and $\overline{B}^0$ tagged events $\Delta\varepsilon$, mis-tag fraction w, mis-tag difference between B^0 and $\overline{B}^0$ tagged events Δw, and effective tagging power Q. All quantities are given in percent.

scaled by $\sigma_{\Delta t}$, the event by event uncertainty of Δt measurement from the vertex fit. The core and tail Gaussian shapes are of the form

$$G(\Delta t, \Delta t_{\text{true}}) \propto \exp\left\{-\frac{[(\Delta t - \Delta t_{\text{true}}) - b\sigma_{\Delta t}]^2}{2(S\sigma_{\Delta t})^2}\right\}, \tag{6.5}$$

where b is the bias and S is the scale factor. The outlier is a traditional Gaussian shape with a mean and a width. The parameters of the resolution function are determined from the B_{flav} sample and fixed in the *CP* fit. We split the parameters to accommodate differences by tagging category as follows:

- The core scale factor S_{core} is split between lepton and non-lepton tagged events.
- The core bias b_{core} is split between lepton and non-lepton tagged events.

The following parameters are fixed

- tail scale factor to 3
- outlier width to 8 ps
- outlier mean to 0 ps.

Table 6.2 contains the values of the tagging and resolution parameters for different data and MC samples.

6.3 *CP* fit description and validation

We extract the *CP* asymmetry parameters in an unbinned ML fit to the $m_{\rm ES}$, Δt and $\cos\theta_{\rm tr}$ distributions. Events, which are untagged or do not meet the requirements $|\Delta t| < 20\,{\rm ps}$ and $\sigma_{\Delta t} < 2.5\,{\rm ps}$, are used to constrain the $m_{\rm ES}$ and $\cos\theta_{\rm tr}$ shapes but do not contribute to the *CP* portion of the fit. The likelihood is then defined as $\mathcal{L} = \mathcal{L}_{CP} \times \mathcal{L}_{\rm untagged}$ with

$$\begin{aligned}
\mathcal{L}_{CP} = \prod_i [& f_{\rm sig} \times \mathcal{F}_{\rm sig}(m_{{\rm ES},i}) \times \mathcal{F}_{\pm,{\rm sig}}(\cos\theta_{{\rm tr},i}, \Delta t_i) + \\
& (1 - f_{\rm sig} - f_{\rm sig} f_{\rm peak}) \times \mathcal{F}_{\rm bg}(m_{{\rm ES},i}) \times \mathcal{F}_{\rm bg}(\cos\theta_{{\rm tr},i}) \times \mathcal{F}_{\pm,{\rm bg}}(\Delta t_i) + \\
& f_{\rm sig} f_{\rm peak} \times \mathcal{F}_{\rm sig}(m_{{\rm ES},i}) \times \mathcal{F}_{\rm bg}(\cos\theta_{{\rm tr},i}) \times \mathcal{F}_{\pm,CP,{\rm bg}}(\Delta t_i)] \\
\mathcal{L}_{\rm untagged} = \prod_i [& f_{\rm sig,untagged} \times \mathcal{F}_{\rm sig}(m_{{\rm ES},i}) \times \mathcal{F}_{\rm sig,untagged}(\cos\theta_{{\rm tr},i}) + \\
& (1 - f_{\rm sig,untagged} - f_{\rm sig,untagged} f_{\rm peak}) \times \mathcal{F}_{\rm bg}(m_{{\rm ES},i}) \times \mathcal{F}_{\rm bg}(\cos\theta_{{\rm tr},i}) + \\
& f_{\rm sig,untagged} f_{\rm peak} \times \mathcal{F}_{\rm sig}(m_{{\rm ES},i}) \times \mathcal{F}_{\rm bg}(\cos\theta_{{\rm tr},i})] \,, \qquad (6.6)
\end{aligned}$$

where $f_{\rm sig}$ is the fraction of signal events; $\mathcal{F}_{\rm sig}(m_{\rm ES})$ is a Gaussian PDF describing the signal; $\mathcal{F}_{\pm,{\rm sig}}(\cos\theta_{\rm tr}, \Delta t)$ is the PDF in Eq. 6.4; $\mathcal{F}_{\rm bg}(m_{\rm ES})$ is an ARGUS threshold PDF; and $F_{\rm bg}(\cos\theta_{\rm tr})$ is the same second order polynomial used in the fit for $R_\perp$. The description of the background PDF in Δt is given by a sum of zero and non-zero lifetime components

$$\mathcal{F}_{\pm,{\rm bg}}(\Delta t) = f_{\rm prompt}\delta(\Delta t) + (1 - f_{\rm prompt})\mathcal{F}_{\pm,CP,{\rm bg}}(\Delta t)\,, \qquad (6.7)$$

	$D^{*+}D^{*-}$ MC	B_{flav} MC	B_{flav} Data
b_{core}—`Lepton`	-0.044 ± 0.033	-0.0439 ± 0.0044	-0.0666 ± 0.0264
b_{core}—non-`Lepton`	-0.230 ± 0.015	-0.2438 ± 0.0020	-0.1916 ± 0.0124
b_{tail}	0.88 ± 0.13	-1.2512 ± 0.0217	-0.9674 ± 0.0987
S_{core}—`Lepton`	0.994 ± 0.058	1.0080 ± 0.0072	1.0142 ± 0.0418
S_{core}—non-`Lepton`	1.091 ± 0.025	1.1037 ± 0.0034	1.0973 ± 0.0206
f_{core}	0.863 ± 0.011	0.8893 ± 0.0014	0.8744 ± 0.0079
f_{outlier}	0.0051 ± 0.0007	0.0039 ± 0.0001	0.0026 ± 0.0005
w—`Lepton`	0.020 ± 0.013	0.0292 ± 0.0004	0.0300 ± 0.0027
w—`Kaon I`	0.045 ± 0.012	0.0611 ± 0.0005	0.0552 ± 0.0032
w—`Kaon II`	0.168 ± 0.011	0.1600 ± 0.0005	0.1489 ± 0.0032
w—`Kaon-Pion`	0.243 ± 0.012	0.2555 ± 0.0006	0.2345 ± 0.0040
w—`Pion`	0.328 ± 0.012	0.3488 ± 0.0006	0.3286 ± 0.0042
w—`Other`	0.434 ± 0.015	0.4216 ± 0.0008	0.4160 ± 0.0052
Δw—`Lepton`	0.016 ± 0.009	0.0009 ± 0.0008	0.0000 ± 0.0051
Δw—`Kaon I`	0.010 ± 0.008	0.0007 ± 0.0009	0.0002 ± 0.0059
Δw—`Kaon II`	-0.008 ± 0.007	-0.0020 ± 0.0009	0.0017 ± 0.0055
Δw—`Kaon-Pion`	-0.016 ± 0.008	-0.0163 ± 0.0010	-0.0019 ± 0.0065
Δw—`Pion`	0.072 ± 0.008	0.0637 ± 0.0010	0.0508 ± 0.0067
Δw—`Other`	0.032 ± 0.009	0.0463 ± 0.0012	0.0377 ± 0.0081

Table 6.2: Resolution and tagging parameters extracted in fits to the $B^0 \to D^{*+}D^{*-}$ signal MC, B_{flav} MC, and B_{flav} data samples.

with $f_{\rm prompt}$ being the fraction of zero lifetime background and

$$\mathcal{F}_{\pm,CP,\rm bg}(\Delta t) \propto e^{-|\Delta t|/\tau_{\rm bg}} \left[1 \pm C_{\rm bg,eff} \cos \Delta m_d \Delta t \pm S_{\rm bg,eff} \sin \Delta m_d \Delta t\right] . \qquad (6.8)$$

The component of the fit dealing with peaking background has only a lifetime component in the Δt background because the source was identified as a specific B decay. And $f_{\rm peak}$ is fixed to the value determined from generic MC in Sec. 4.7.2. All of the PDF components that depend on Δt are convolved with the resolution function from Sec. 6.2. The signal PDF's that depend on $\cos\theta_{\rm tr}$ are convolved with the angular resolution function described in Sec. 5.3. Table 6.3 lists the parameters which float in the ML fit.

For simplicity, we neglect the angular acceptance moments. Their effect on the values of the *CP* parameters is negligible. Instead of explicitly modeling the angular acceptance moments in the signal PDF, we absorb their effects into an effective $R_{\perp,\rm eff}$ which will differ from the value of $R_\perp$ we found in Chapter 5. This procedure is validated using MC in Sec. 6.3.1

6.3.1 Toy MC validation

In the time-dependent *CP* analysis, we neglect the acceptance moments of the angular distribution described in Sec. 5.2. This simplifies the signal PDF and speeds up the likelihood calculation. The effect of this simplification is that the $R_{\perp,\rm eff}$ value, which floats in the fit, absorbs the acceptance and leaves the *CP* parameters

Parameter	Description	Splitting
m_{B^0}	B^0 mass	
$\sigma_{m_{B^0}}$	width of $m_{\rm ES}$ signal	
κ	ARGUS shape parameter	
$f_{\rm sig}$	signal fraction	split by tagging category
$R_{\perp,\rm eff}$	effective *CP*-odd fraction	
b_2	$\cos\theta_{\rm tr}$ background shape	
$\tau_{\rm bg}$	effective lifetime of Δt background	
$f_{\rm prompt}$	fraction of zero-lifetime Δt background	
S	*CP* asymmetry	split by *CP*-even and odd
C	direct *CP* asymmetry	split by *CP*-even and odd
$S_{\rm bg,eff}$	background effective *CP*	split by tagging category
$C_{\rm bg,eff}$	background effective *CP*	split by tagging category

Table 6.3: Parameters which float in the time-dependent *CP* fit.

unbiased. Were we to include the acceptance moments $I_j(z)$, Eq. 6.1 would become

$$\begin{aligned}\frac{1}{\Gamma}\frac{\mathrm{d}^2\Gamma}{\mathrm{d}z\mathrm{d}t} \propto e^{-|\Delta t|^2/\tau_{B^0}} \{&[O_+(z)G_+(z) + O_-(z)G_-(z)] \\ &\mp [C_+(z)G_+(z) + C_-(z)G_-(z)]\cos\Delta m_d\Delta t \\ &\pm [S_+(z)G_+(z) - S_-(z)G_-(z)]\sin\Delta m_d\Delta t\} \ , \end{aligned} \tag{6.9}$$

with

$$\begin{aligned} O_+(z) &= |A^0_\parallel|^2 I_\parallel(z) + |A^0_0|^2 I_0(z) \\ O_-(z) &= |A^0_\perp|^2 I_\perp(z) \\ C_+(z) &= C_\parallel |A^0_\parallel|^2 I_\parallel(z) + C_0 |A^0_0|^2 I_0(z) \\ C_-(z) &= C_\perp |A^0_\perp|^2 I_\perp(z) \\ S_+(z) &= S_\parallel |A^0_\parallel|^2 I_\parallel(z) + S_0 |A^0_0|^2 I_0(z) \\ S_-(z) &= S_\perp |A^0_\perp|^2 I_\perp(z) \, . \end{aligned} \tag{6.10}$$

To validate that the *CP* parameters remain unbiased, we generate toy MC

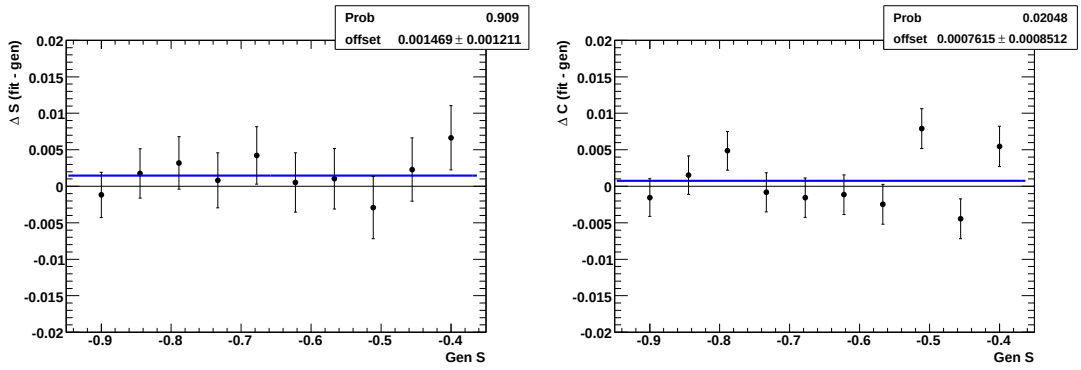

Figure 6.1: Difference between fitted and generated S and C as a function of the value of S. Here $R_\perp = 0.125$, $C = 0$, and $\alpha = 0$.

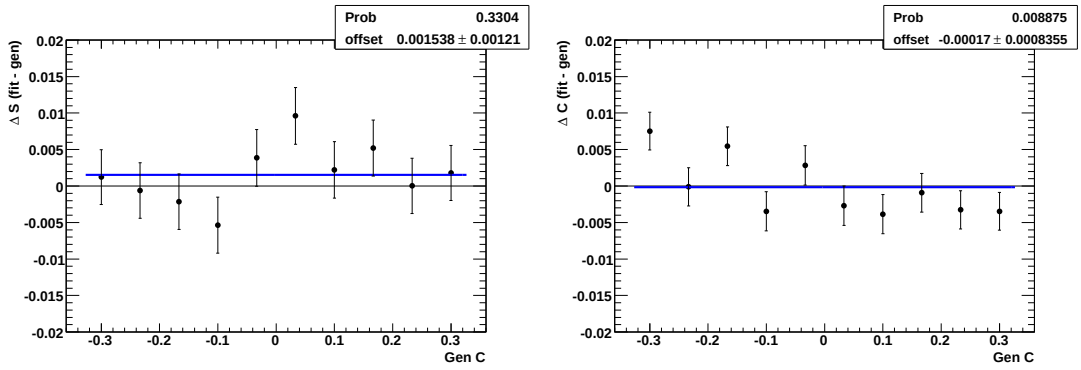

Figure 6.2: Difference between fitted and generated S and C as a function of the value of C. Here $R_\perp = 0.125$, $S = -0.7$, and $\alpha = 0$.

samples of 200k events according to Eq. 6.9 and fit these samples using Eq. 6.1. We assume that $C_\parallel = C_0 = C_\perp$ and that $S_\parallel = S_0 = S_\perp$. Plots of the deviation from generated S and C as a function of the generated S, C, $R_\perp$, and α are shown in Figs. 6.1–6.4. We observe no significant bias.

Confident that the acceptance can be safely neglected, we turn to validating the fitting procedure using toy MC generated from the PDF's which make up the likelihood. We perform 500 data-sized toy experiments with $S_+ = S_\perp = -0.703$, $C_+ = C_\perp = 0$, $R_\perp = 0.14$, and other parameters set to those expected from pre-

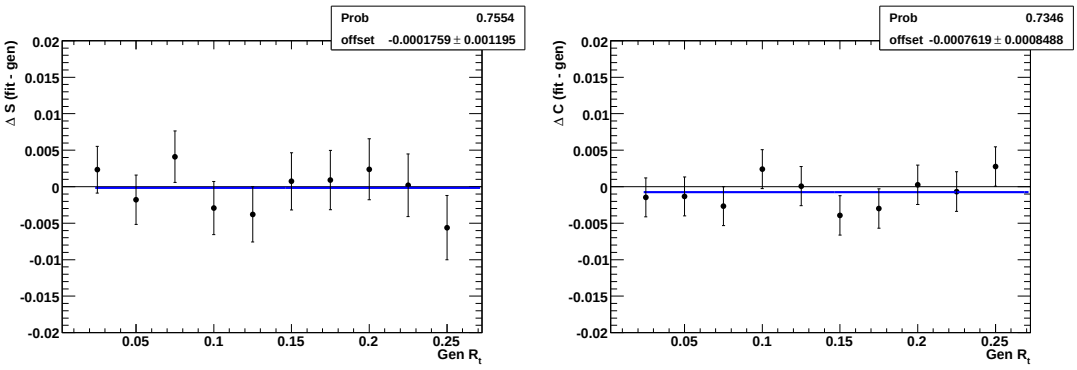

Figure 6.3: Difference between fitted and generated S and C as a function of the value of $R_\perp$. Here $C = 0.0$, $S = -0.7$, and $\alpha = 0$.

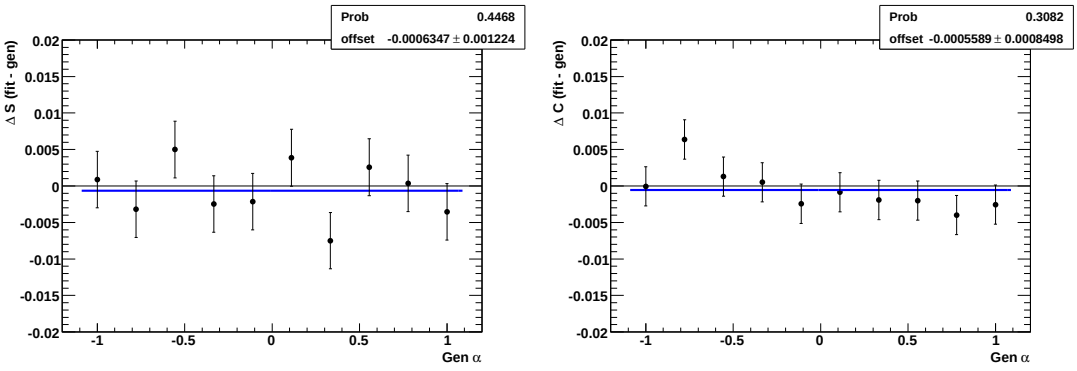

Figure 6.4: Difference between fitted and generated S and C as a function of the value of α. Here $R_\perp = 0.125$, $C = 0.0$, and $S = -0.7$.

liminary fits to just the $m_{\rm ES}$ spectrum in data. The distributions of the fitted *CP* parameters, their errors and pulls are shown in Fig. 6.5. From the pull distributions, we find no significant bias and that the errors from the fitter are reasonable.

6.3.2 Embedded toy MC validation

We divide our signal MC dataset generated with full detector simulation into 112 data-sized subsets and combine it with background events generated from the background PDF's. We fit these embedded toy MC experiments using the full fitting procedure. The results of this study are shown in Fig. 6.6. Again, we see no significant bias.

6.3.3 Full MC validation

Before applying our fitter to the data, we fit our MC samples which includes full detector simulation. The signal MC sample was generated with $S = -0.703$, $C = 0$, and $R_\perp = 0.0626$. The second sample of generic MC weighted to the integrated luminosity has the same *CP* parameters but $R_\perp = 0.222$. In these fits, we are able to obtain the generated *CP* parameters within statistical errors. In addition to fitting separate S_+, $S_\perp$, C_+ and $C_\perp$, we also fit constraining $S_+ = S_\perp = S$ and $C_+ = C_\perp = C$. The fit results are compiled in Table 6.4, and the projection plots are in Figs 6.7–6.10.

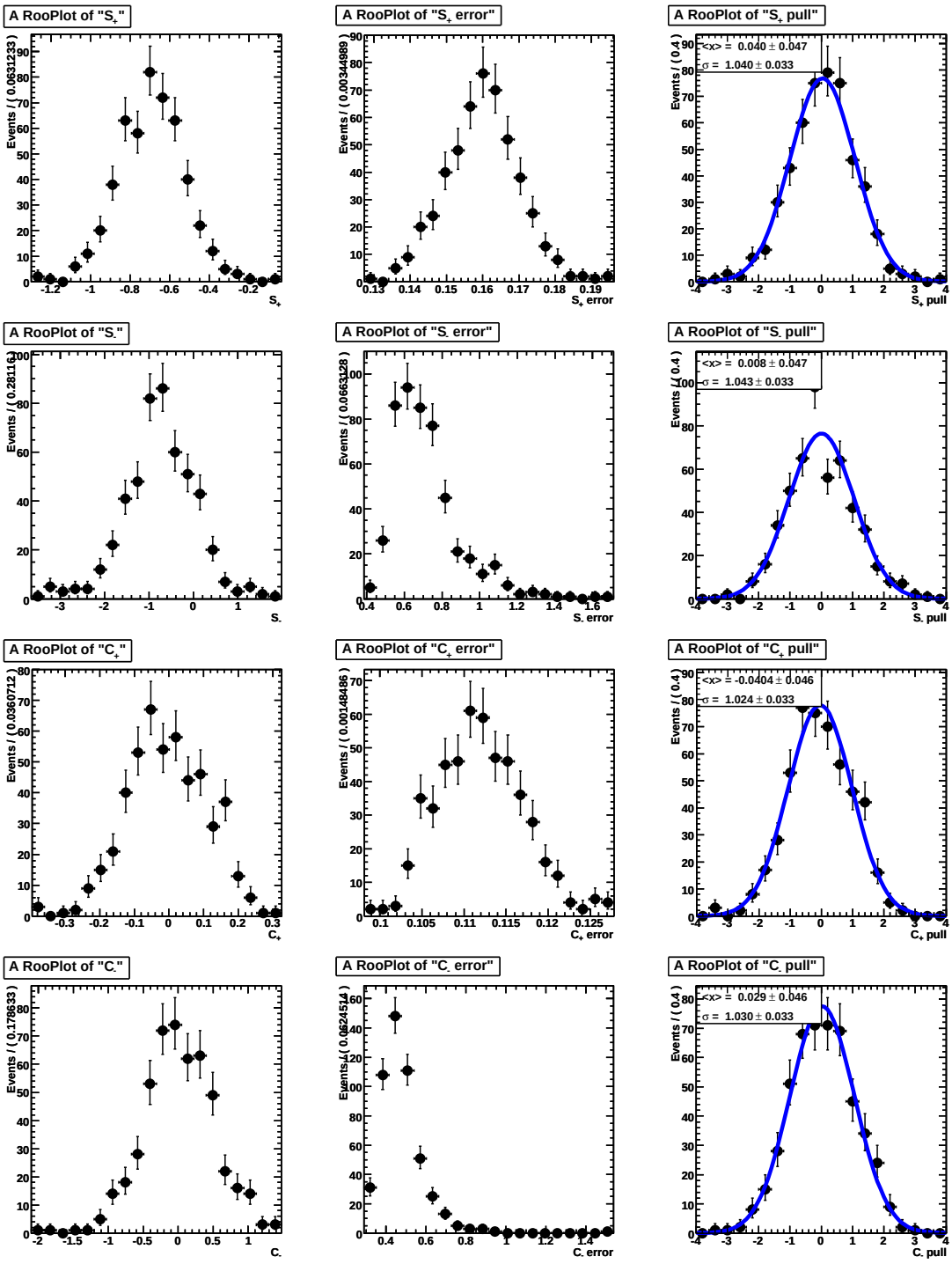

Figure 6.5: Toy MC distributions of the *CP* parameters S_+, $S_\perp$, C_+, and $C_\perp$ for 500 toy experiments. The left plot is the distribution of the parameter; the center is the distribution of the errors; and the right is the pull.

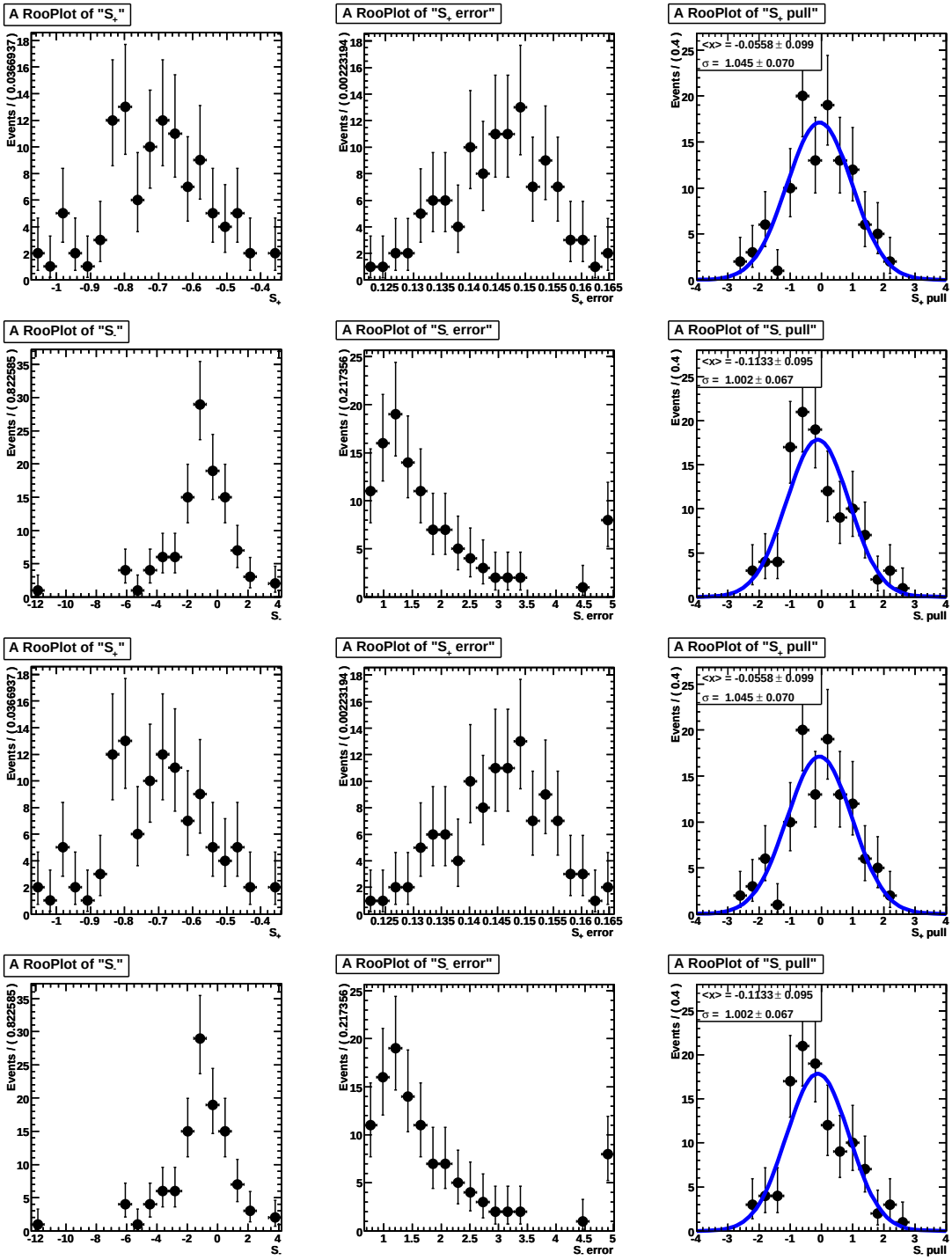

Figure 6.6: Embedded toy MC distributions of the *CP* parameters S_+, $S_\perp$, C_+, and $C_\perp$ for 112 experiments. The left plot is the distribution of the parameter; the center is the distribution of the errors; and the right is the pull.

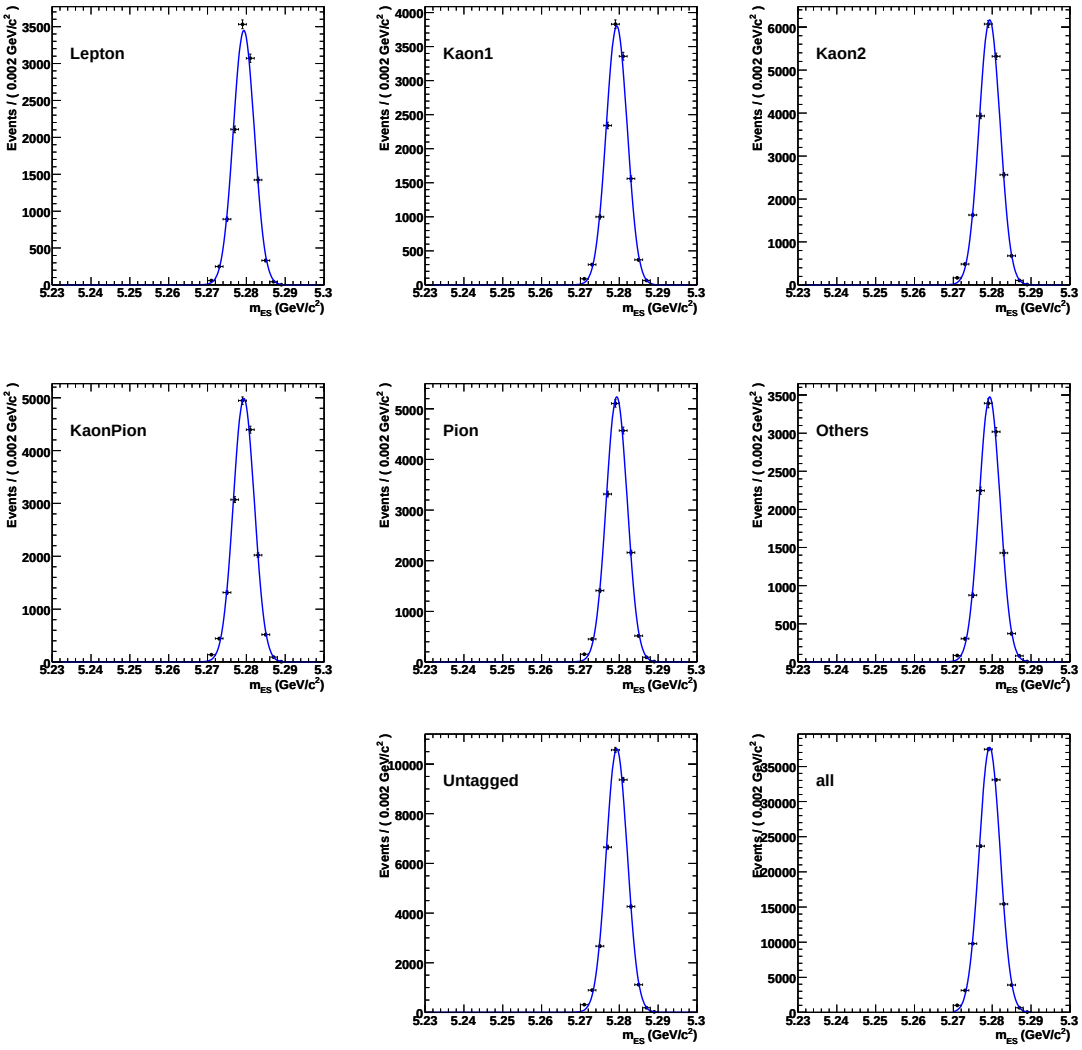

Figure 6.7: Projection of the fit to signal MC onto $m_{\rm ES}$ for each of the tagging categories and combined in the final plot.

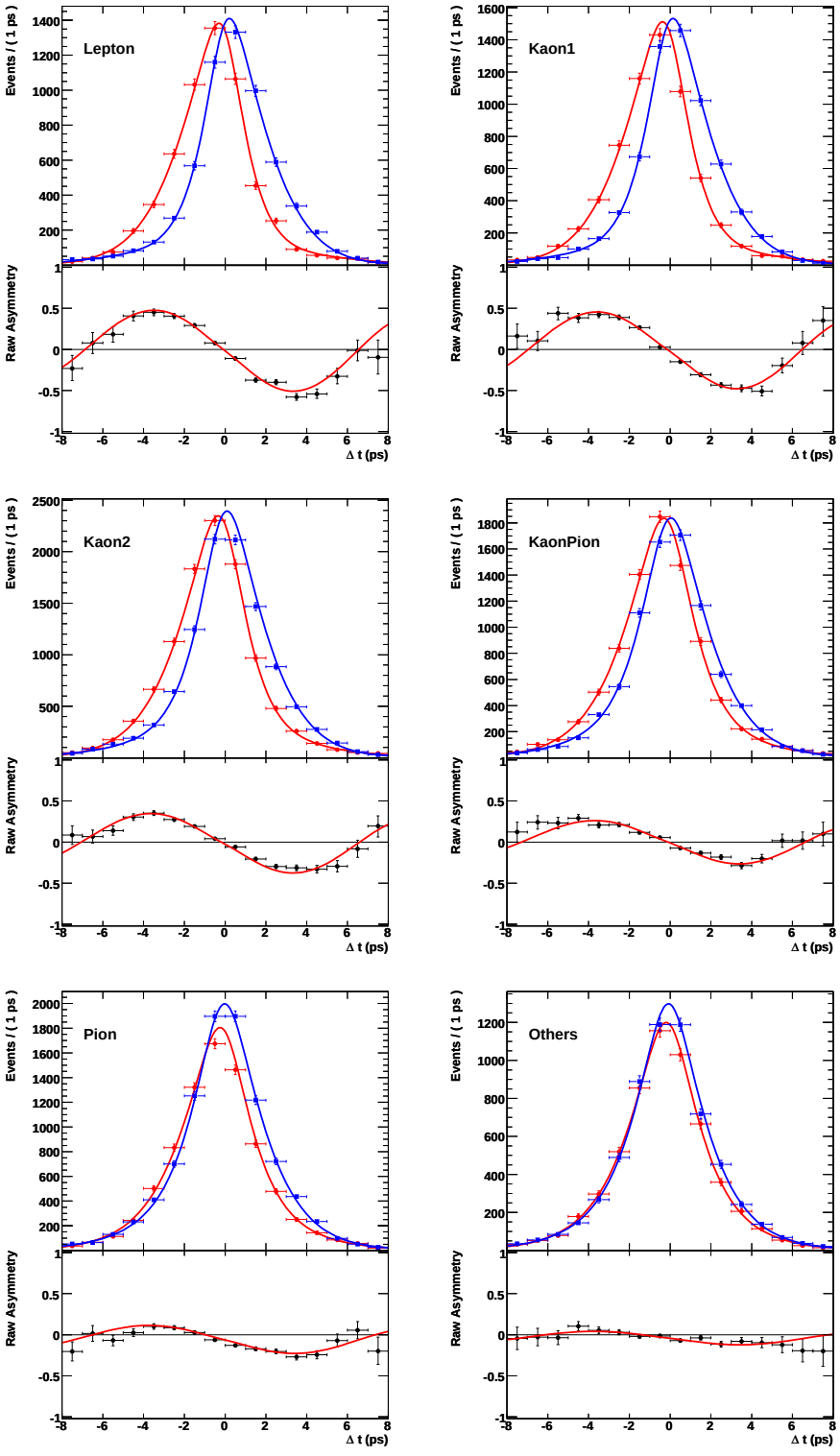

Figure 6.8: Projection of the fit to signal MC onto Δt and the raw flavor asymmetry for each of the tagging categories.

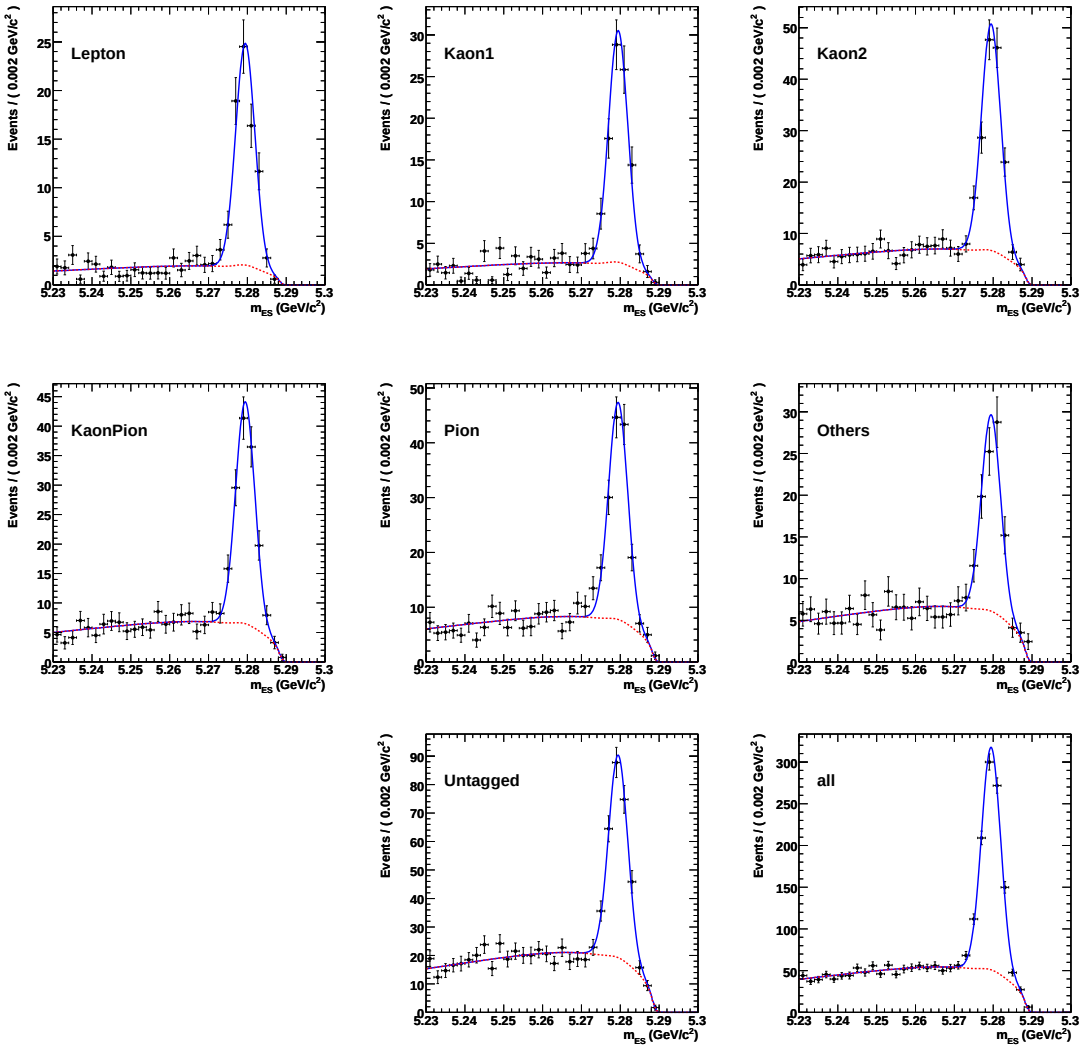

Figure 6.9: Projection of the fit to generic MC onto $m_{\rm ES}$ for each of the tagging categories and combined in the final plot.

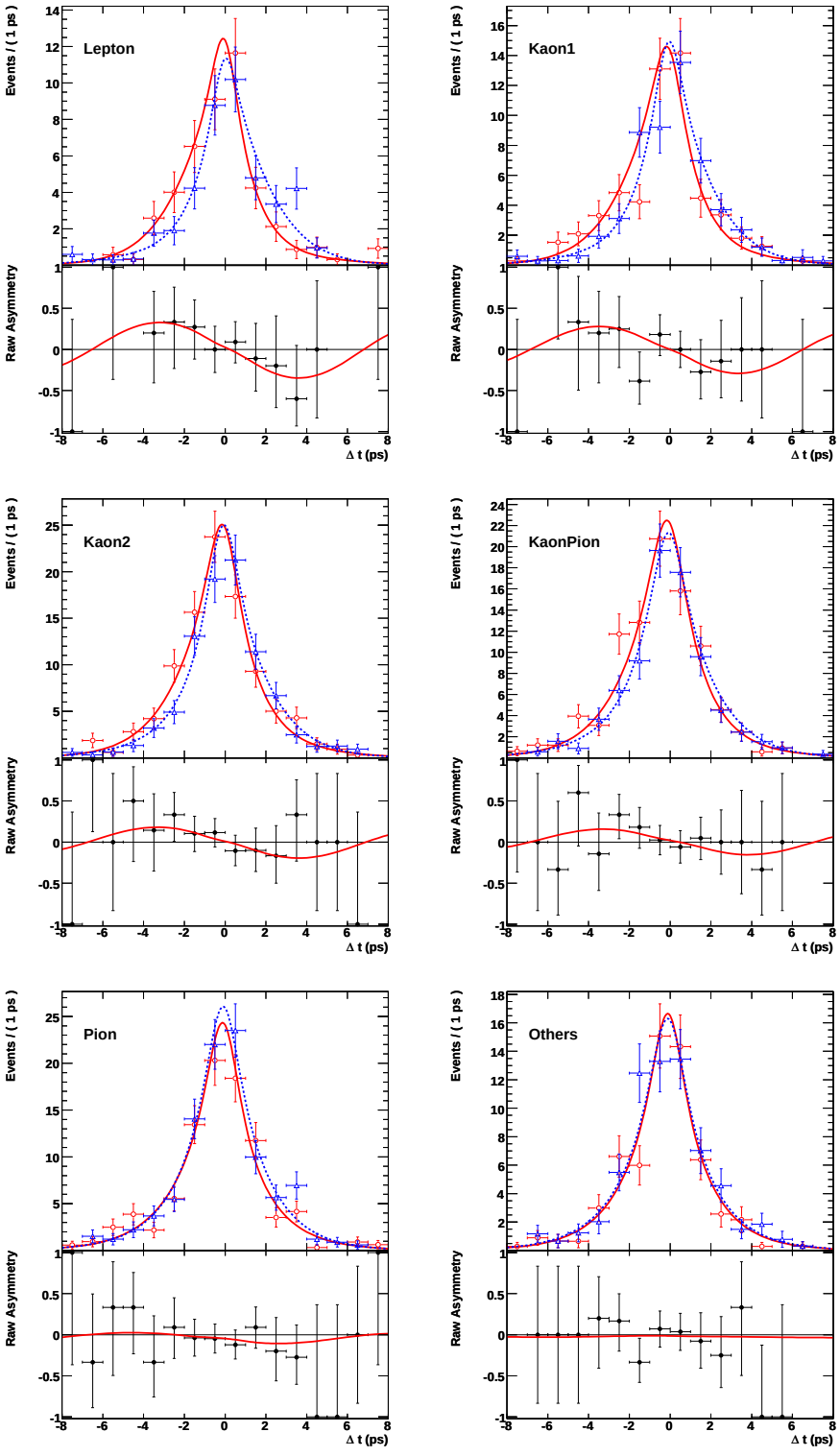

Figure 6.10: Projection of the fit to generic MC onto Δt and the raw flavor asymmetry for each of the tagging categories.

	Signal MC	Generic MC
S_+	-0.698 ± 0.011	-0.76 ± 0.17
$S_\perp$	-0.888 ± 0.098	-1.12 ± 0.49
C_+	0.008 ± 0.008	-0.06 ± 0.13
$C_\perp$	-0.033 ± 0.065	0.13 ± 0.35
$R_\perp$	0.0652 ± 0.0017	0.212 ± 0.031
S	-0.690 ± 0.011	-0.74 ± 0.17
C	0.005 ± 0.007	-0.026 ± 0.094
$R_\perp$	0.0662 ± 0.0017	0.218 ± 0.030

Table 6.4: Fitted *CP* parameters for MC simulation including full detector simulation.

6.4 Systematic uncertainties

After blinding the *CP* parameters, we evaluate the systematic uncertainties. These uncertainties are summarized in Table 6.5 and described in this section.

6.4.1 Tagging parameters

As was mentioned in Sec. 6.1 and Sec. 6.2, we fix the parameters related to tagging performance and Δt resolution to those obtained from a separate fit to the $B_{\rm flav}$ sample. To assign a corresponding systematic error we generate 100 random parameter sets using the error matrix from the $B_{\rm flav}$ fit and refit our data using these parameters. The distribution of the *CP* parameters in these fits are shown in Fig. 6.11. We fit these distributions with a Gaussian function and take its width plus the absolute value of its mean as the systematic uncertainty.

In addition, we use the alternative tagging parameters from Table 6.1 and fit our signal MC sample and assign the differences as the systematic uncertainty associated with alternative parameters.

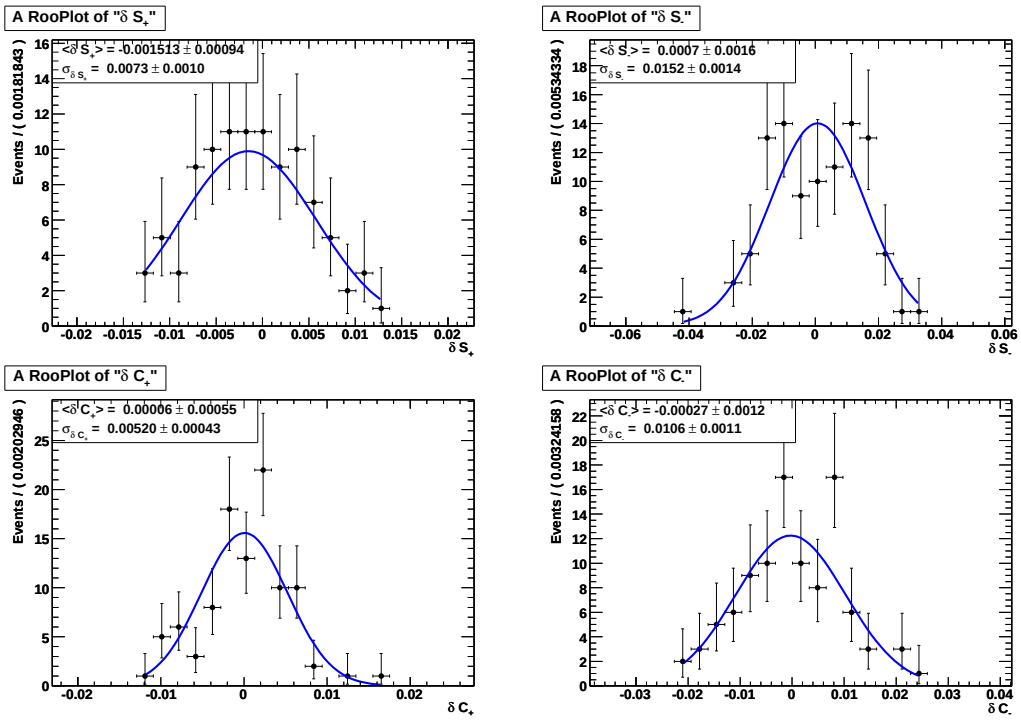

(a) Split *CP*-even and odd

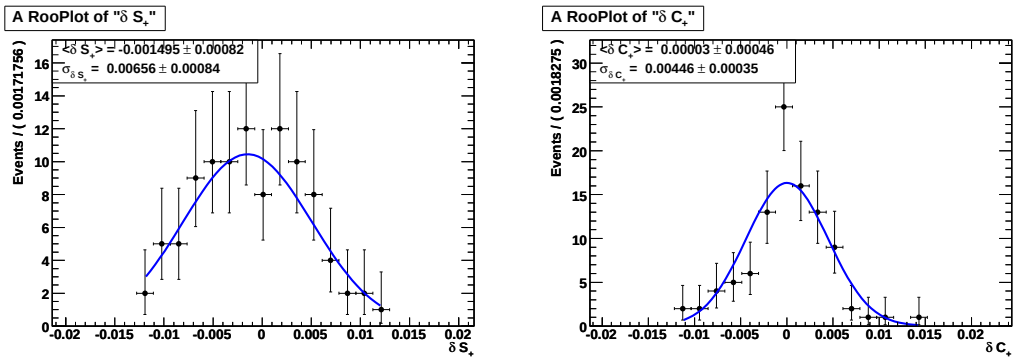

(b) Combined *CP*-even and odd

Figure 6.11: Distribution of CP parameters fit using randomized sets of tagging and Δt resolution parameters.

	C_+	$C_\perp$	S_+	$S_\perp$	C	S
Tagging variations	0.0053	0.0108	0.0088	0.0160	0.0045	0.0081
Tagging alternatives	0.0084	0.0125	0.0206	0.0263	0.0073	0.0198
Peaking background	0.0021	0.0186	0.0120	0.0787	0.0028	0.0116
Prompt fraction	0.0003	0.0152	0.0105	0.0243	0.0020	0.0106
Δm_d variation	0.0040	0.0210	0.0061	0.0005	0.0005	0.0061
τ_{B^0} variation	0.0007	0.0040	0.0024	0.0046	0.0001	0.0030
Angular resolution	0.0004	0.0017	0.0007	0.0050	0.0001	0.0005
slow π mis-reconstruction	0.0035	0.0147	0.0246	0.0908	0.0006	0.0115
Angular background	0.0002	0.0002	0.0006	0.0022	0.0000	0.0007
Potential fit bias	0.0079	0.0648	0.0112	0.0981	0.0066	0.0105
Boost uncertainty	0.0027	0.0115	0.0014	0.0036	0.0004	0.0012
SVT alignment	0.0013	0.0188	0.0058	0.0294	0.0018	0.0050
DCSD interference	0.0144	0.0144	0.0020	0.0020	0.0144	0.0020
Total Systematic error	0.0203	0.0801	0.0397	0.1629	0.0184	0.0320

Table 6.5: Systematic error contributions to $B^0 \to D^{*+}D^{*-}$ *CP* parameters.

6.4.2 Peaking background

In the nominal fit, we fix the peaking background yield to be 1.6% of the signal. To estimate the uncertainty associated with this we vary the fraction of peaking background +1.9% and −1.6%. We increase the width of the peaking background to ×1.5 the signal width, and change the $\cos\theta_{\rm tr}$ distribution to that of the signal rather than the background. We sum the difference in *CP* parameters for each variation in quadrature to obtain the full peaking background systematic error.

6.4.3 Prompt background fraction

We allow the fraction of zero lifetime background $f_{\rm prompt}$, common to all tagging categories, to float in the fit. `Lepton` tagged events should not have prompt

background, an assumption born out by our MC. To evaluate a systematic uncertainty associated with conflating our prompt background we split off the `Lepton` tagged events and assign them $f_{\text{prompt—}\texttt{Lepton}} = 0$. The difference in the *CP* parameters with respect to the nominal fit is taken as the corresponding systematic error.

6.4.4 Fixed Δm_d and τ_{B^0} parameters

The physics input parameters Δm_d and τ_{B^0} are fixed to their PDG 2006 [37] values. We vary these parameters by their quoted errors and take the sum of the deviations in quadrature as the systematic uncertainty.

6.4.5 Angular resolution

We study our dependence on the angular resolution parameters using the same method described in Sec. 5.5.1. Figures 6.12–6.17 show the distribution of the *CP* parameters. We take the root mean square width of the distribution plus the magnitude of the mean as the systematic uncertainty.

We additionally include as a systematic the change in the *CP* parameters when removing the uncorrelated term from the angular fit.

6.4.6 Angular background

We use the method from Sec. 5.5.5 to evaluate the systematic uncertainty associated with the shape of the $\cos\theta_{\text{tr}}$ background PDF.

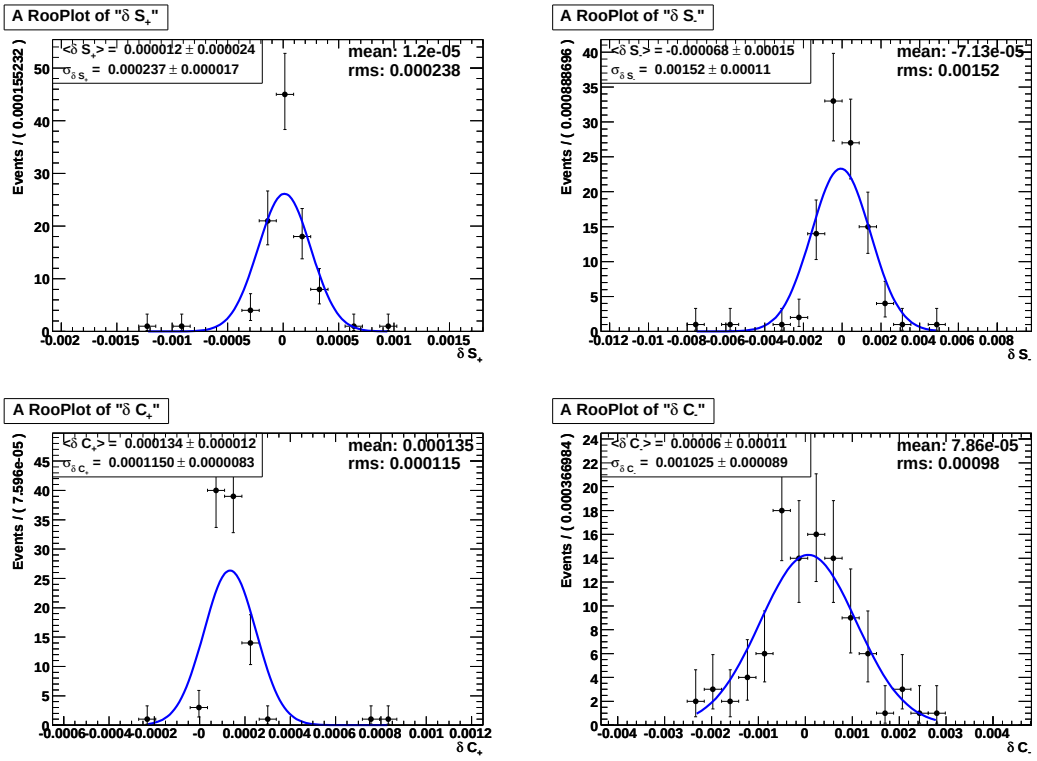

Figure 6.12: Distribution of *CP* parameters split by *CP*-even and odd using randomized angular resolution parameters for the $\pi^+\pi^0$ slow pion mode.

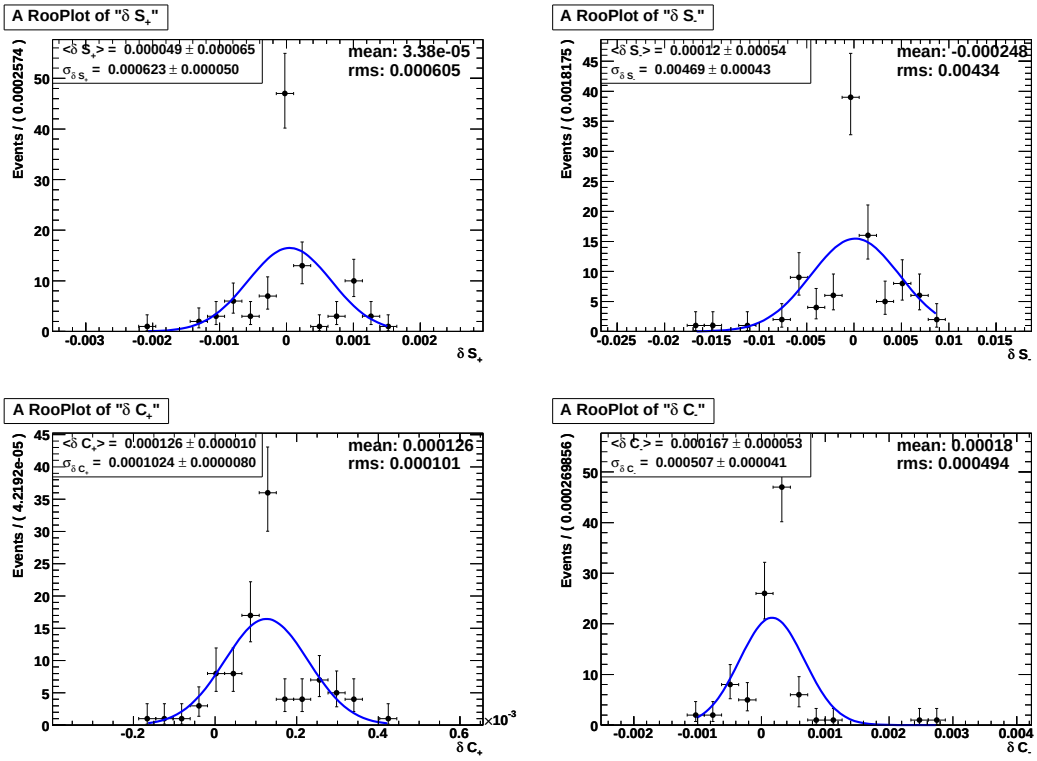

Figure 6.13: Distribution of *CP* parameters split by *CP*-even and odd using randomized angular resolution parameters for the $\pi^+\pi^-$ slow pion mode.

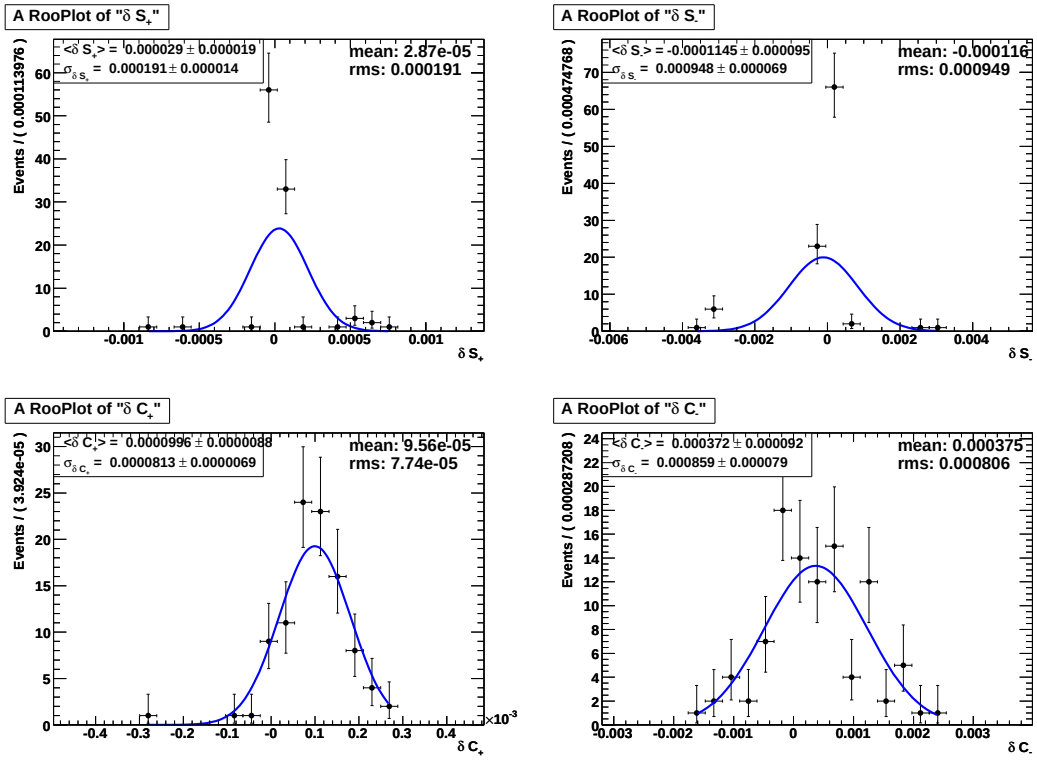

Figure 6.14: Distribution of *CP* parameters split by *CP*-even and odd using randomized angular resolution parameters for the $\pi^0\pi^-$ slow pion mode.

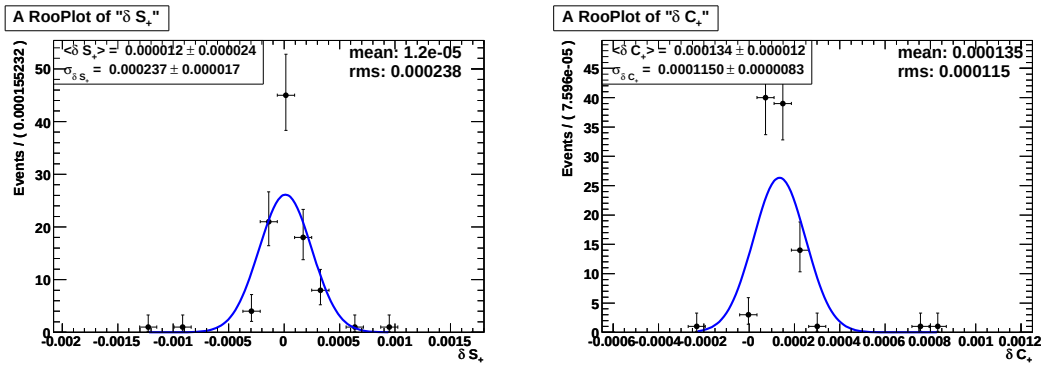

Figure 6.15: Distribution of combined *CP* parameters using randomized angular resolution parameters for the $\pi^+\pi^0$ slow pion mode.

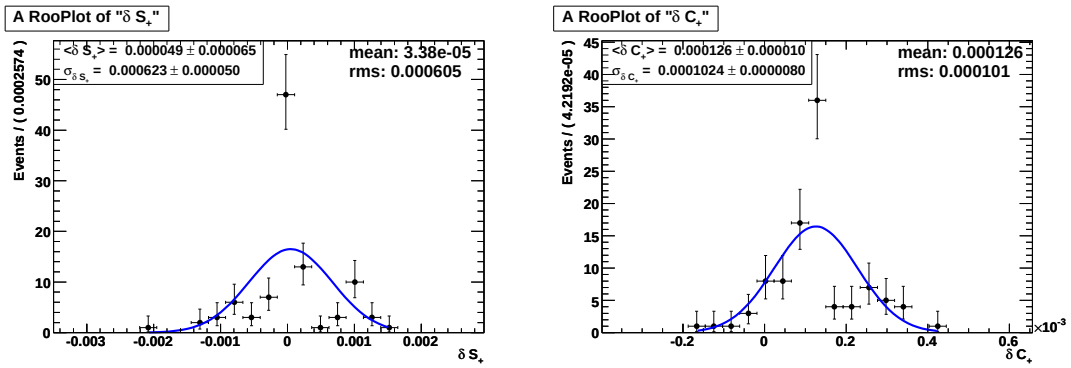

Figure 6.16: Distribution of combined *CP* parameters using randomized angular resolution parameters for the $\pi^+\pi^-$ slow pion mode.

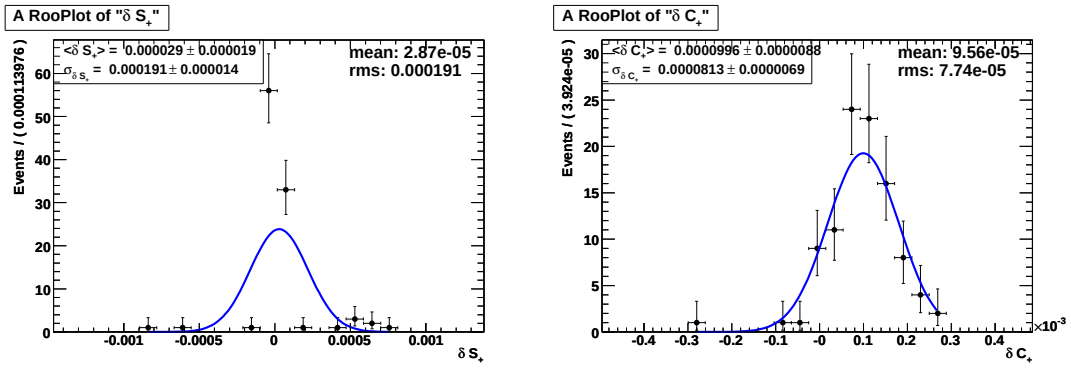

Figure 6.17: Distribution of combined *CP* parameters using randomized angular resolution parameters for the $\pi^0\pi^-$ slow pion mode.

6.4.7 Potential fit bias

In our MC validations we see no significant bias. We assign the statistical error from the fit to the signal MC as a systematic related to our ability to validate the fitting procedure for potential bias.

6.4.8 Boost uncertainty

The effect of the uncertainty of the boost and the z scale affects the measurement of Δt. To evaluate our dependence we scale Δt and its error $\sigma_{\Delta t}$ by $\pm 0.6\%$. The changes in the C and S parameters are taken as the systematic error.

6.4.9 SVT alignment

Because the SVT provides the precise determination of the B decay vertices and thus Δt, we evaluate our sensitivity to the alignment of the SVT. SVT alignment experts have provided four different misalignment configurations and one configuration with a shift in the z direction of entire layers. We refit the events from our signal MC sample using each of the five configurations. To avoid fluctuations in S and C due to events migrating in and out of the final sample we keep only the events which are common to all samples and fit these events to extract S and C. We take the largest difference with respect to the nominal alignment added in quadrature with the difference from the fifth configuration as the systematic uncertainty.

6.4.10 Tag interference from DCSD amplitudes

Tagging performance suffers from doubly-CKM-suppressed decays (DCSD) of the tag side B meson undergoing a $b \to u\bar{c}d$ transition [42]. These affect tags using kaons and pions, but not leptons. We evaluate the systematic uncertainty using

$$\begin{aligned} C_{\text{fit}} &= C_0 \left[1 + 2r' \cos\delta' \left\{\mathcal{G}\cos(2\beta+\gamma) - S_0 \sin(2\beta+\gamma)\right\}\right] \\ &\quad - 2r' \sin\delta' \left\{S_0 \cos(2\beta+\gamma) + \mathcal{G}\sin(2\beta+\gamma)\right\} \\ S_{\text{fit}} &= S_0 \left[1 + 2r' \cos\delta' \mathcal{G}\cos(2\beta+\gamma)\right] + 2r' \sin\delta' C_0 \cos(2\beta+\gamma)\,, \end{aligned} \tag{6.11}$$

where the shifts are randomly sampled using

- r' uniform on $[0.00, 0.04]$
- δ' uniform on $[0, 2\pi]$
- γ uniform on $[39^\circ, 80^\circ]$
- $C_0 = -0.02$
- $S_0 = -0.66$
- $\mathcal{G} = \cos 2\beta$
- $2\beta = \sin^{-1} 0.71 = 45.2^\circ$.

The resulting distribution of the shift in S and C are shown in Fig. 6.18.

The systematic uncertainty is the 68% coverage of the shifts corrected for the presence of leptonic tags which are not sensitive to DCSD interference. We apply a

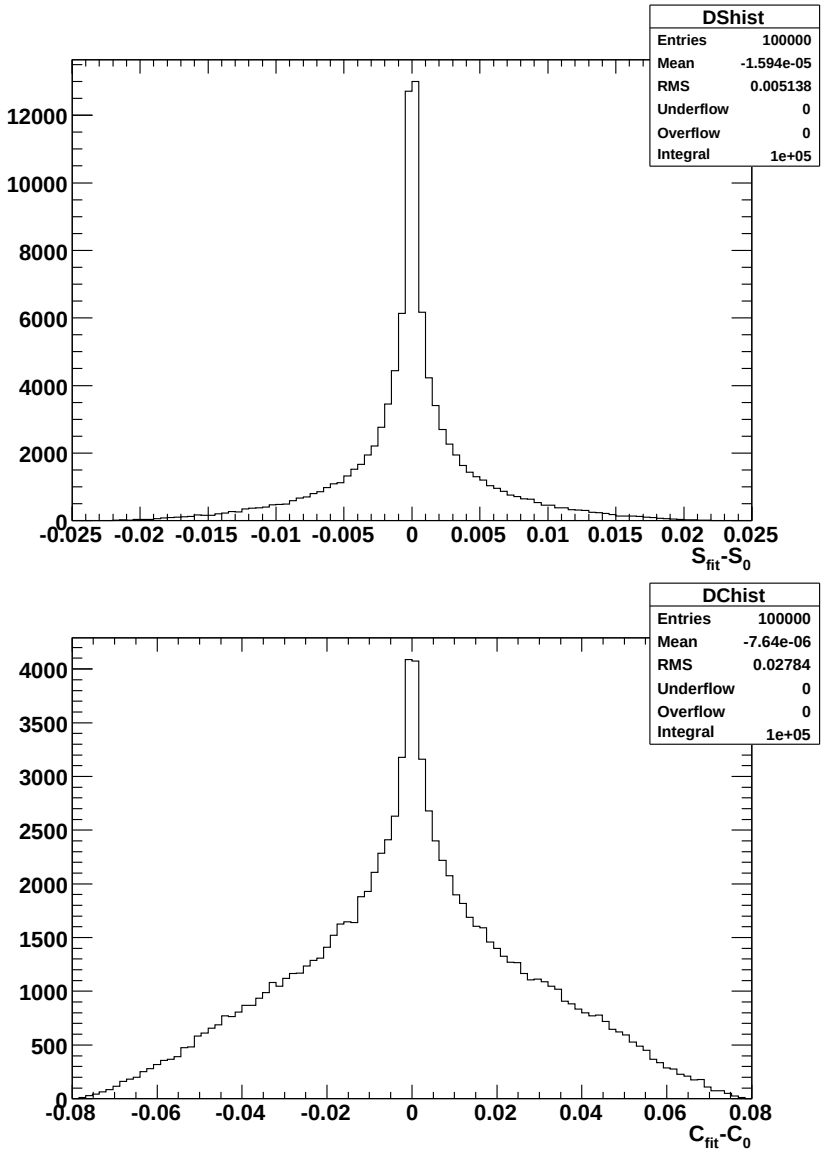

Figure 6.18: Distributions of the deviation of C and S due to doubly-CKM-suppressed decays.

correction factor of 0.5 to obtain

$$\Delta S = 0.004 \times 0.5 = 0.002$$

$$\Delta C = 0.0288 \times 0.5 = 0.0144\,. \tag{6.12}$$

6.5 Results

The fit to data yields $N_{\rm sig} = 934 \pm 40$ events and $N_{\rm bg} = 1637 \pm 57$ events in the region $m_{\rm ES} > 5.23$. The *CP* asymmetry is

$$\begin{aligned} C_+ &= \quad 0.02 \pm 0.12 \pm 0.02 \\ C_\perp &= \quad 0.41 \pm 0.50 \pm 0.08 \\ S_+ &= -0.76 \pm 0.16 \pm 0.04 \\ S_\perp &= -1.81 \pm 0.71 \pm 0.16 \\ R_{\perp,\rm eff} &= \quad 0.155 \pm 0.030\,. \end{aligned} \tag{6.13}$$

As expected, the value of $R_{\perp,\rm eff}$ is different from the $R_\perp$ of the time-integrated transversity analysis. Constraining $C_+ = C_\perp$ and $S_+ = S_\perp$ yields

$$\begin{aligned} C &= \quad 0.047 \pm 0.091 \pm 0.019 \\ S &= -0.71 \pm 0.16 \pm 0.03 \\ R_{\perp,\rm eff} &= \quad 0.171 \pm 0.028\,. \end{aligned} \tag{6.14}$$

In each preceding measurement the first (only) uncertainty is statistical in nature and the second is systematic. The correlations among the *CP* parameters are given in Tables 6.6 and 6.7. The break down of all the floating parameters from the fits

with split and combined *CP* parameters are shown in Table 6.8. Figures 6.19–6.21 show the projections of the fit onto data.

	S_+	S_-	C_+	C_-	$R_\perp$
S_+	1.000	0.376	0.008	−0.036	−0.083
S_-	0.376	1.000	0.045	−0.224	0.471
C_+	0.008	0.045	1.000	−0.465	0.003
C_-	−0.036	−0.224	−0.465	1.000	−0.151
$R_{\perp,\mathrm{eff}}$	−0.083	0.471	0.003	−0.151	1.000

Table 6.6: Correlations of *CP* parameters for the case where they are split based on *CP*-even or -odd.

	S	C	$R_\perp$
S	1.000	0.008	−0.083
C	0.008	1.000	0.003
$R_{\perp,\mathrm{eff}}$	−0.083	0.003	1.000

Table 6.7: Correlations of *CP* parameters for the case where they are not split.

Parameter	Separate *CP*-even and -odd	Combined *CP*-even and odd
$C_\perp$	0.41 ± 0.50	—
C_+	0.02 ± 0.12	0.05 ± 0.09
$S_\perp$	-1.81 ± 0.71	—
S_+	-0.76 ± 0.16	-0.71 ± 0.16
$R_{\perp,\text{eff}}$	0.155 ± 0.030	0.171 ± 0.028
m_{B^0}	5.2793 ± 0.0001	5.2793 ± 0.0001
$\sigma_{m_{B^0}}$	0.00267 ± 0.00012	0.00269 ± 0.00012
f_{sig}-Lepton	0.647 ± 0.051	0.650 ± 0.050
f_{sig}-Kaon I	0.575 ± 0.047	0.576 ± 0.047
f_{sig}-Kaon II	0.436 ± 0.034	0.438 ± 0.034
f_{sig}-Kaon-Pion	0.396 ± 0.035	0.398 ± 0.035
f_{sig}-Pion	0.294 ± 0.032	0.296 ± 0.032
f_{sig}-Other	0.318 ± 0.036	0.319 ± 0.037
f_{sig}-Untagged	0.289 ± 0.023	0.291 ± 0.023
κ	-61.1 ± 6.0	-60.6 ± 6.0
b_2	-0.276 ± 0.073	-0.286 ± 0.072
τ_{bg}	1.28 ± 0.11	1.28 ± 0.11
C_{bg}-Lepton	-0.15 ± 0.31	-0.15 ± 0.32
C_{bg}-Kaon I	0.02 ± 0.26	0.03 ± 0.27
C_{bg}-Kaon II	-0.08 ± 0.15	-0.07 ± 0.15
C_{bg}-Kaon-Pion	-0.07 ± 0.15	-0.07 ± 0.15
C_{bg}-Pion	0.29 ± 0.13	0.29 ± 0.13
C_{bg}-Other	-0.19 ± 0.15	-0.19 ± 0.15
S_{bg}-Lepton	0.04 ± 0.49	0.08 ± 0.49
S_{bg}-Kaon I	-0.12 ± 0.41	-0.08 ± 0.41
S_{bg}-Kaon II	-0.43 ± 0.21	-0.41 ± 0.22
S_{bg}-Kaon-Pion	0.10 ± 0.24	0.12 ± 0.24
S_{bg}-Pion	-0.07 ± 0.19	-0.06 ± 0.19
S_{bg}-Other	0.27 ± 0.24	0.28 ± 0.24
$f_{\text{bg,prompt}}$	0.334 ± 0.069	0.336 ± 0.069

Table 6.8: Fit results from the fit to data. The errors are purely statistical.

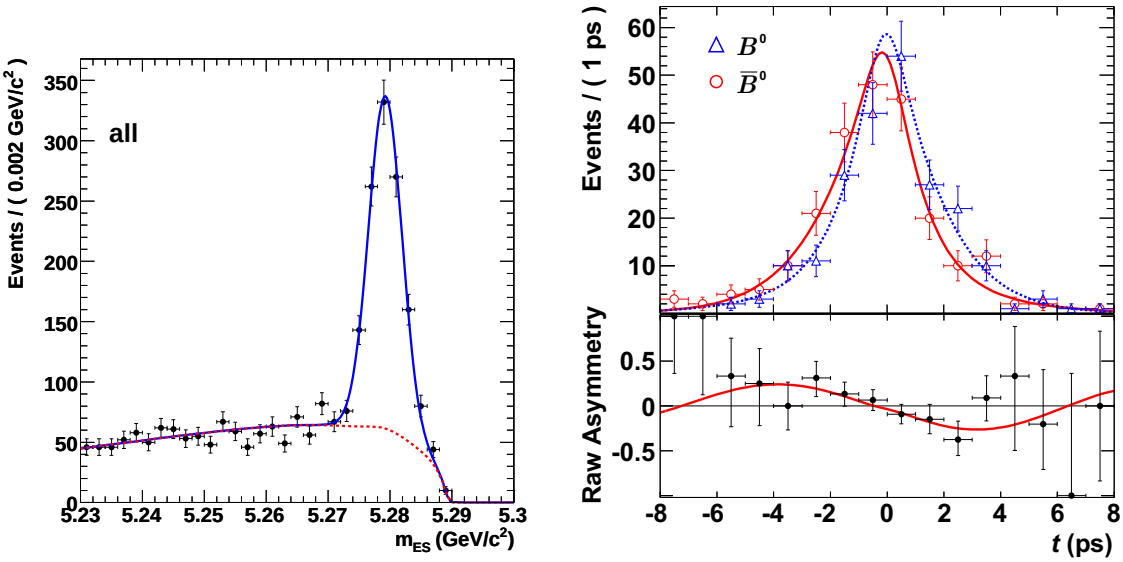

Figure 6.19: Projections of the fit result onto data. The left plot is the $m_{\rm ES}$ spectrum for all tagging categories. The right plot is the projection onto Δt and its raw flavor asymmetry for the `Lepton`, `Kaon I`, and `Kaon II` events.

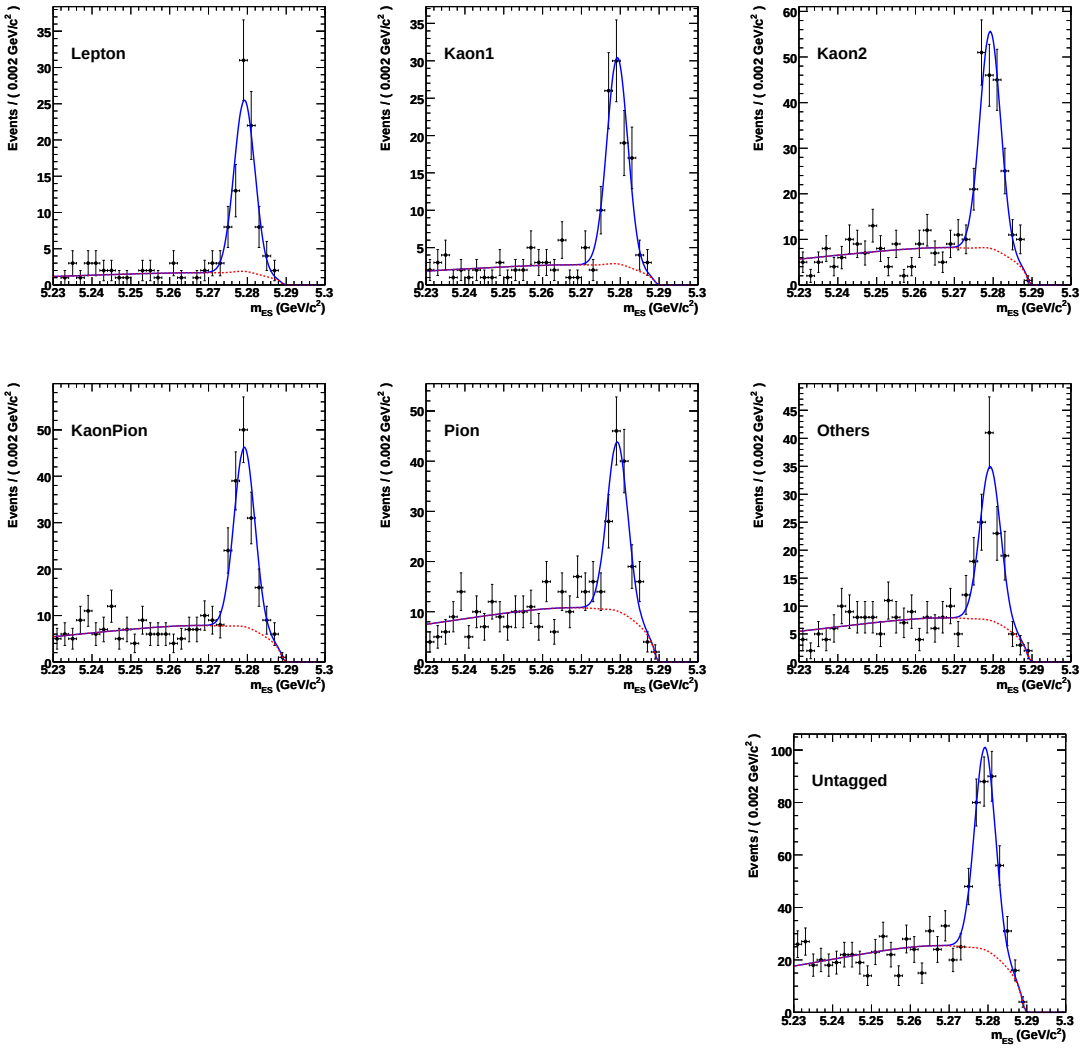

Figure 6.20: Projections of the m_{ES} component of the fit result onto data for each tagging category. The dashed red line represents the background contribution.

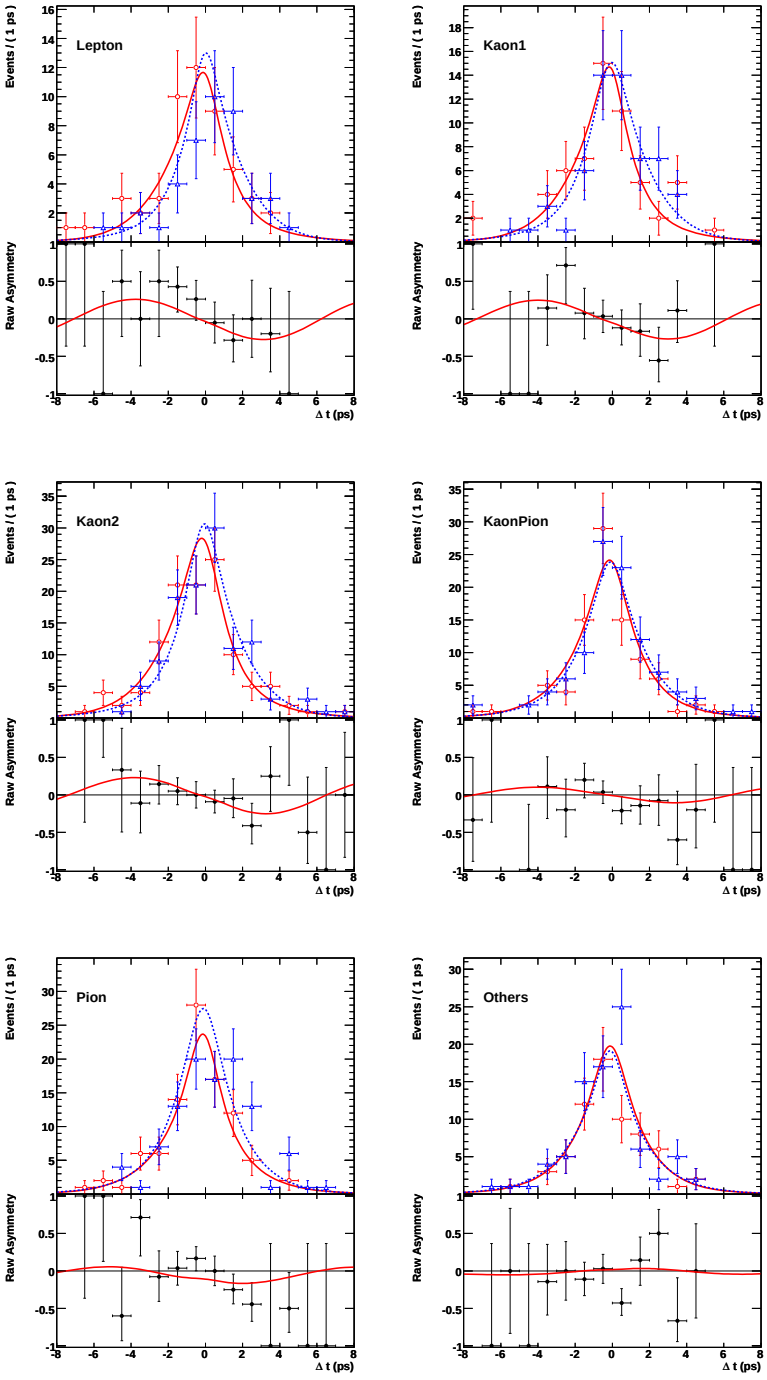

Figure 6.21: Projections of the Δt component of the fit result onto data for each tagging category. The triangular points and blue dashed line are for B^0 tagged events. The circular points and red line are for the $\overline{B}^0$ tagged events. The lower of each plot is the raw flavor asymmetry.

Chapter 7

Conclusions

7.1 Summary of results

We have measured the *CP*-odd fraction $R_\perp$ and time-dependent *CP* asymmetry of $B^0 \to D^{*+}D^{*-}$ decays shown in Table 7.1. These results are consistent with the SM and the most recent *BABAR* measurement in the $B^0 \to J/\psi K^0_S$ [44]. Figure 7.1 [45] shows excellent agreement of sin2β from this result, other related decays, and with the world average from $b \to (c\bar{c})s$ transitions.

7.2 Final words

The agreement of sin2β between $B^0 \to D^{*+}D^{*-}$ and $B^0 \to J/\psi K^0_S$ suggests that factorization and HQET are soundly rooted for calculations of this type. The contributions of the penguin amplitudes cannot be overly large. A full angular anal-

$R_\perp$	$0.158 \pm 0.028 \pm 0.006$
C_+	$0.02 \pm 0.12 \pm 0.02$
$C_\perp$	$0.41 \pm 0.50 \pm 0.08$
S_+	$-0.76 \pm 0.16 \pm 0.04$
$S_\perp$	$-1.81 \pm 0.71 \pm 0.16$
Constraining $C_+ = C_\perp$ and $S_+ = S_\perp$	
C	$0.05 \pm 0.09 \pm 0.02$
S	$-0.71 \pm 0.16 \pm 0.03$

Table 7.1: *CP* parameters extracted from the full dataset. The first uncertainty is statistical; the second is systematic.

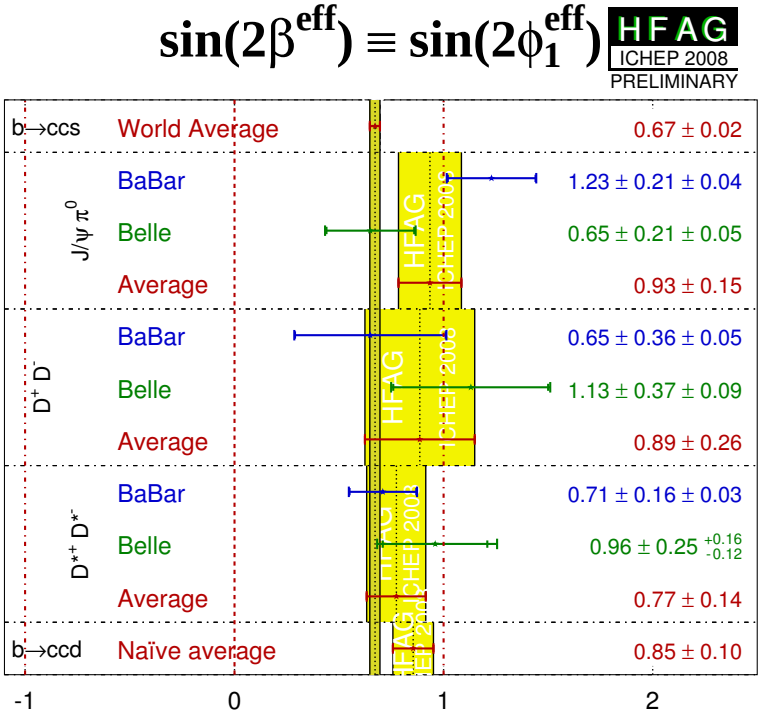

Figure 7.1: Averages showing sin2β from measurements of $b \to c\bar{c}d$ transitions in comparison with that from the "golden" $b \to c\bar{c}s$ transitions.

ysis of $B^0 \to D^{*+}D^{*-}$ decays would yield further understanding of the validity of the assumptions and could hold sensitivity to $\cos 2\beta$, however this analysis is technically very challenging. Because these measurements are still statistically limited, a super B factory could significantly improve the measurement of the asymmetries and better constrain the theoretical models.

The current constraints on the Unitarity Triangle are pictured in Fig. 7.2 [46]. So far significant deviations from what could be expected in the SM have not been observed.

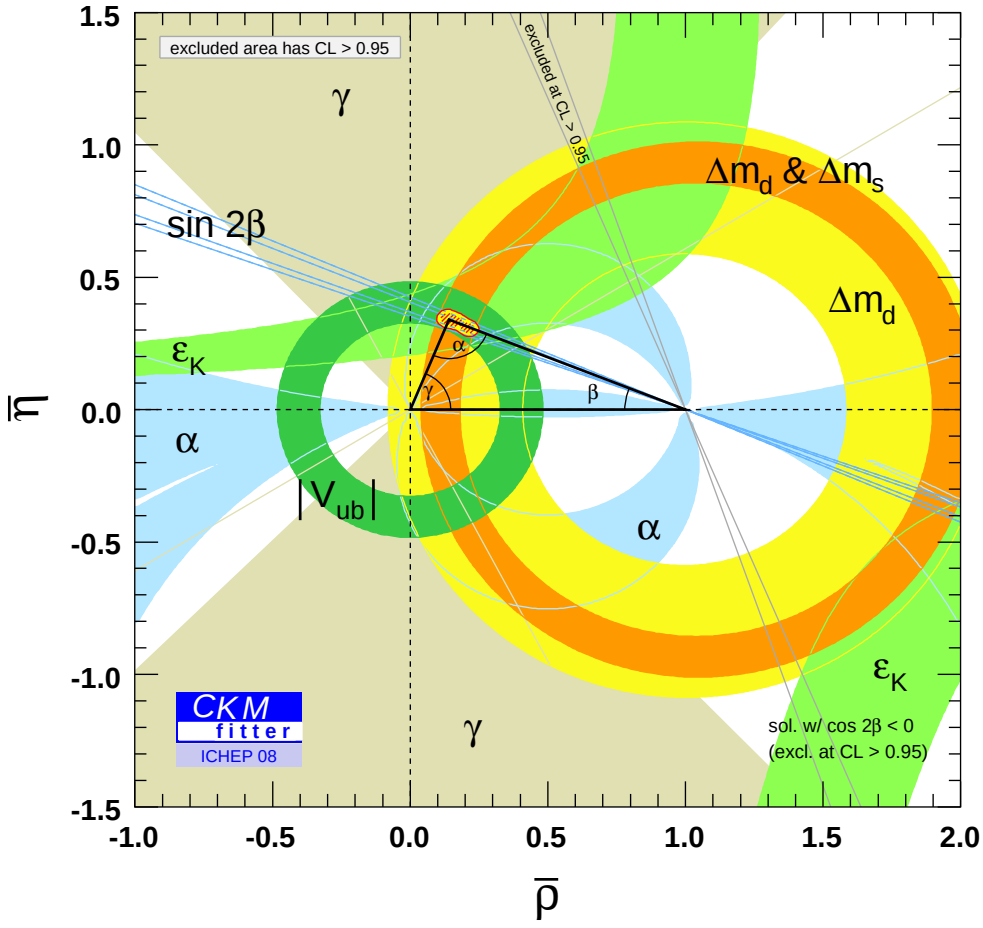

Figure 7.2: Constraints on the Unitarity Triangle in the $(\bar{\rho}, \bar{\eta})$ plane.

Bibliography

[1] A. D. Sakharov. Violation of *CP* Invariance, *C* Asymmetry, and Baryon Asymmetry of the Universe. *Pisma Zh. Eksp. Teor. Fiz.* **5**:32 (1967).

[2] I. Dunietz, H. R. Quinn, A. Snyder, W. Toki, and H. J. Lipkin. How to extract *CP* violating asymmetries from angular correlations. *Phys. Rev.* **D43**:2193 (1991).

[3] P. F. Harrison and H. R. Quinn (*BABAR* Collaboration). The *BABAR* physics book: Physics at an asymmetric *B* factory (1998). SLAC-R-0504, Papers from Workshop on Physics at an Asymmetric B Factory (*BABAR* Collaboration Meeting), Rome, Italy, 11-14 Nov 1996, Princeton, NJ, 17-20 Mar 1997, Orsay, France, 16-19 Jun 1997 and Pasadena, CA, 22-24 Sep 1997.

[4] J. Goldstone, A. Salam, and S. Weinberg. Broken Symmetries. *Phys. Rev.* **127**:965 (1962).

[5] S. Weinberg. A Model of Leptons. *Phys. Rev. Lett.* **19**:1264 (1967).

[6] M. E. Peskin and D. V. Schroeder. *An Introduction to quantum field theory*. Addison-Wesley (1995).

[7] F. Halzen and A. D. Martin. *Quarks and Leptons: An Introductory Course in Modern Particle Physics*. Wiley (1984).

[8] C. S. Wu, E. Ambler, R. W. Hayward, D. D. Hoppes, and R. P. Hudson. Experimental test of parity conservation in beta decay. *Phys. Rev.* **105**:1413 (1957).

[9] J. H. Christenson, J. W. Cronin, V. L. Fitch, and R. Turlay. Evidence for the 2π decay of the K_2^0 meson. *Phys. Rev. Lett.* **13**(4):138 (Jul 1964).

[10] B. Aubert *et al.* (*BABAR* Collaboration). Observation of *CP* Violation in the B^0 Meson System. *Phys. Rev. Lett.* **87**(9):091801 (Aug 2001). [hep-ex/0107013].

[11] K. Abe *et al.* (Belle Collaboration). Observation of Large *CP* Violation in the Neutral *B* Meson System. *Phys. Rev. Lett.* **87**(9):091802 (Aug 2001). [hep-ex/0107061].

[12] C. Amsler *et al.* (Particle Data Group). Review of particle physics. *Phys. Lett.* **B667**:1 (2008).

[13] B. Aubert *et al.* (*BABAR* Collaboration). Search for T, *CP* and CPT violation in $B^0\overline{B}^0$ mixing with inclusive dilepton events. *Phys. Rev. Lett.* **96**:251802 (2006). [hep-ex/0603053].

[14] N. Cabibbo. Unitary Symmetry and Leptonic Decays. *Phys. Rev. Lett.* **10**:531 (1963).

[15] M. Kobayashi and T. Maskawa. *CP* Violation in the Renormalizable Theory of Weak Interaction. *Prog. Theor. Phys.* **49**:652 (1973).

[16] L. Wolfenstein. Parametrization of the Kobayashi-Maskawa Matrix. *Phys. Rev. Lett.* **51**:1945 (1983).

[17] A. I. Sanda and Z. Z. Xing. Determination of ϕ_1 with $B \to D^{(*)}\overline{D}^{(*)}$. *Phys. Rev.* **D56**:341 (1997). [hep-ph/9702297].

[18] G. Michelon. A theoretical review of the $B \to D^{(*)}\overline{D}^{(*)}$ decay channel (1996). SLAC-BABAR-NOTE-34.

[19] X. Y. Pham and Z. Z. Xing. *CP* asymmetries in $B_d \to D^{*+}D^{*-}$ and $B_s \to D_s^{*+}D_s^{*-}$ decays: P-wave dilution, penguin and rescattering effects. *Phys. Lett.* **B458**:375 (1999). [hep-ph/9904360].

[20] Z. Z. Xing. Measuring *CP* violation and testing factorization in $B_d \to D^{*\pm}D^{\mp}$ and $B_s \to D_s^{*\pm}D_s^{\mp}$ decays. *Phys. Lett.* **B443**:365 (1998).

[21] Z. Z. Xing. *CP* violation in $B_d \to D^+D^-$, $D^{*+}D^-$, D^+D^{*-} and $D^{*+}D^{*-}$ decays. *Phys. Rev.* **D61**:014010 (2000).

[22] V. A. Lillard. *Measurements of the CP content and CP violating asymmetries in neutral B decays to two D* mesons with the BABAR detector*. Ph.D. thesis, University of Maryland (2004). SLAC-R-761.

[23] B. Aubert *et al.* (*BABAR* Collaboration). Measurement of time-dependent *CP* asymmetries and the *CP*-odd fraction in the decay $B^0 \to D^{*+}D^{*-}$. *Phys. Rev. Lett.* **95**:151804 (2005). [hep-ex/0506082].

[24] H. Miyake *et al.* (Belle Collaboration). Branching fraction, polarization and CP-violating asymmetries in $B^0 \to D^{*+}D^{*-}$ decays. *Phys. Lett.* **B618**:34 (2005).

[25] J. L. Rosner. Determination of pseudoscalar charmed meson decay constants from B meson decays. *Phys. Rev.* **D42**:3732 (1990).

[26] G. Kramer and W. F. Palmer. Branching ratios and *CP* asymmetries in the decay $B \to VV$. *Phys. Rev.* **D45**:193 (1992).

[27] Y. Grossman and M. P. Worah. *CP* asymmetries in B decays with new physics in decay amplitudes. *Phys. Lett.* **B395**:241 (1997).

[28] R. Zwicky. Unparticles at heavy flavour scales: *CP* violating phenomena. *Phys. Rev.* **D77**:036004 (2008). [arXiv:0707.0677 [hep-ph]].

[29] M. Gronau, J. L. Rosner, and D. Pirjol. Small amplitude effects in $B^0 \to D^+D^-$ and related decays. *Phys. Rev.* **D78**:033011 (2008). [arXiv:0805.4601 [hep-ph]].

[30] B. Aubert *et al.* (BABAR). The *BABAR* detector. *Nucl. Instrum. Meth.* **A479**:1 (2002). [hep-ex/0105044].

[31] U. Wienands, Y. Cai, S. D. Ecklund, J. T. Seeman, and M. K. Sullivan. PEP-II at $1.2 \times 10^{34}-/\mathrm{cm}^2/\mathrm{s}$ luminosity. In *Proceeding of Particle Accelerator Conference (PAC 07)*, page 37. Albuquerque, New Mexico (Jun 2007). Invited talk at Particle Accelerator Conference.

[32] I. Adam *et al.* (*BABAR* DIRC). The DIRC particle identification system for the *BABAR* experiment. *Nucl. Instrum. Meth.* **A538**:281 (2005).

[33] P. Coyle *et al.* The DIRC counter: A New type of particle identification device for B factories. *Nucl. Instrum. Meth.* **A343**:292 (1994).

[34] W. Menges. The *BABAR* muon system upgrade. *IEEE Nucl. Sci. Symp. Conf. Rec.* **5**:1470 (2006). [physics/0609039].

[35] D. J. Lange. The EvtGen particle decay simulation package. *Nucl. Instrum. Meth.* **A462**:152 (2001).

[36] S. Agostinelli *et al.* (GEANT4 Collaboration). GEANT4: A simulation toolkit. *Nucl. Instrum. Meth.* **A506**:250 (2003).

[37] W. M. Yao *et al.* (Particle Data Group). Review of particle physics. *J. Phys.* **G33**:1 (2006). with 2007 partial update for the 2008 edition.

[38] B. Aubert *et al.* (*BABAR* Collaboration). Measurement of branching fractions and *CP*-violating charge asymmetries for B-meson decays to $D^{(*)}\overline{D}^{(*)}$, and implications for the Cabibbo-Kobayashi-Maskawa angle gamma. *Phys. Rev.* **D73**(11):112004 (2006). [hep-ex/0604037].

[39] G. C. Fox and S. Wolfram. Observables for the Analysis of Event Shapes in e^+e^- Annihilation and Other Processes. *Phys. Rev. Lett.* **41**:1581 (1978).

[40] W. D. Hulsbergen. Decay chain fitting with a Kalman filter. *Nucl. Instrum. Meth.* **A552**:566 (2005). [physics/0503191].

[41] B. Aubert *et al.* (*BABAR* Collaboration). A study of time dependent *CP*-violating asymmetries and flavor oscillations in neutral B decays at the $\Upsilon(4S)$. *Phys. Rev.* **D66**:032003 (2002).

[42] O. Long, M. Baak, R. N. Cahn, and D. Kirkby. Impact of tag-side interference on time dependent CP asymmetry measurements using coherent B^0 anti-B^0 pairs. *Phys. Rev.* **D68**:034010 (2003). [hep-ex/0303030].

[43] H. Albrecht *et al.* (ARGUS Collaboration). Search for hadronic $b \to u$ decays. *Phys. Lett.* **B241**:278 (1990).

[44] B. Aubert *et al.* (*BABAR* Collaboration). Improved Measurement of *CP* Violation in Neutral B Decays to $c\bar{c}s$. *Phys. Rev. Lett.* **99**:171803 (2007). [hep-ex/0703021].

[45] Heavy Flavor Averaging Group. Results on Time-Dependent *CP* Violation, and Measurements Related to the Angles of the Unitarity Triangle: Summer 2008 (ICHEP2008, USA & CKM2008, Italy) (2008). http://www.slac.stanford.edu/xorg/hfag/triangle/summer2008/index.shtml.

[46] J. Charles *et al.* (CKMfitter Group). *CP* violation and the CKM matrix: Assessing the impact of the asymmetric B factories. *Eur. Phys. J.* **C41**:1 (2005). updated results and plots available at: http://ckmfitter.in2p3.fr , [hep-ph/0406184].